Dissertation

submitted to the

Combined Faculties of the Natural Sciences and Mathematics
of the Ruperto-Carola-University of Heidelberg. Germany

for the degree of

Doctor of Natural Sciences

Put forward by

Brenden Scott Nickerson

Born in: Halifax, Nova Scotia, Canada.

Oral examination: December 10, 2019

Towards coherent control of the ^{229}Th isomeric transition in VUV-transparent crystals

First referee: PD Dr. Adriana Pálffy-Buß
Second referee: Prof. Dr. Maurits W. Haverkort

Zusammenfassung

Der ^{229m}Th-Isomerenzustand bei 8.28 eV erregt groes Interesse als mglicher Kandidat fr die Entwicklung einer nuklearen Uhr mit bislang unerreichter Przision und Stabilitt. Ein Ansatz zum Bau einer solchen Uhr beruht auf der Anregung von Thoriumkernen, die in VUV-transparenten Kristallen dotiert sind. Die Anregung in der Kristallumgebung muss allerdings noch experimentell erreicht werden. In dieser Dissertation untersuchen wir von theoretischer Warte zwei Methoden zur Anregung des Th-isomerenzustands in der Kristallumgebung. Wir betrachten zunchst die Mglichkeit, Experimente mit nuklearer Vorwrtsstreuung durchzufhren, die eine eindeutige Signatur der nuklearen Anregung liefern und damit die Verstimmung der treibenden Lasersysteme in Bezug auf die fragliche bergangsenergie quantifizieren knnten. Diese Arbeit umfasst die Analyse der Phasendifferenz und der Zeitverzgerung zwischen Anregungsimpulsen sowie die Rolle von Magnetfeldern und der Orientierung der Dotierung auf die Energieniveaus zur Anregung. Als zweite Methode untersuchen wir Elektronenbrcke (EB) Prozesse in der Kristallumgebung, die bisher in der Literatur noch nicht erforscht wurden. Der EB Ansatz nutzt die in nuklearer Vorwrtsstreuung vernachlssigte Kopplung zwischen Kern und Elektronenhlle aus. Es werden neuartige EB-Schemata in der Kristallumgebung vorgestellt, die darauf abzielen, die Isomerenpopulation unter Verwendung von Breitbandanregungsquellen zu erhhen. Die Raten solcher EB-Prozesse werden berechnet und ihre Vorteile im Vergleich zu die direkte Laseranregung werden prsentiert. Diese Erkenntnisse untersttzen die zuknftige Entwicklung einer nuklearen Uhr.

Abstract

The ^{229m}Th isomeric state at approximately 8.28 eV has generated significant interest as a possible candidate for the development of a nuclear clock with cutting edge precision and stability. One of the approaches to build such a clock relies on the excitation of thorium nuclei doped into VUV-transparent crystals. Excitation in the crystal environment has yet to be achieved experimentally. In this dissertation we investigate from the theoretical side, two methods aimed at exciting thorium's isomeric state within the crystal environment. We study first the possibility to carry out nuclear forward scattering style experiments which could provide a unique signature of the nuclear excitation along with quantifying the detuning of the driving laser systems to the transition energy in question. This work includes analysis of the phase difference and time delay between excitation pulses along with the role of magnetic fields and dopant orientations on the level schemes available for driving. As a second method we investigate Electronic Bridge (EB) processes within the crystal environment which have never been addressed so far in the literature. EB exploits the coupling between the nucleus and the electronic shell which is neglected in the direct laser excitation approach. Novel EB schemes in the crystal environment are introduced which aim to increase the isomeric population with the use of broadband excitation sources. Rates of such EB processes are calculated and their advantages with respect to the direct laser excitation are discussed. These findings support the development of a solid-state nuclear clock.

Within the framework of this dissertation the following article was published in a refereed journal

Collective effects in ^{229}Th-doped crystals
Brenden S. Nickerson, Wen-Te Liao, and Adriana Pálffy
Phys. Rev. A 98, 062520 - Published 26 December 2018

And the following article is in preparation

Electronic Bridge processes in ^{229}Th-doped crystals
Brenden S. Nickerson, Martin Pimon, Pavlo V. Bilous, Peter Mohn, Thorsten Schumm and Adriana Pálffy

Contents

Introduction 1

I Nuclear Forward Scattering in Thorium-Doped Crystals 5

1 Theoretical background for Nuclear Forward Scatting (NFS) 7
1.1 Bloch equations . . . 8
1.1.1 Unitary transformations and the Rotating-Wave Approximation (RWA) . . . 10
1.1.2 Two-state system . . . 13
1.2 Maxwell's field equation . . . 14
1.2.1 Resonant cross section . . . 16
1.2.2 Initial conditions: Rabi Frequency . . . 18
1.2.3 Factoring of Clebsch-Gordan coefficients . . . 19
1.3 Nuclear forward scattering and the Maxwell-Bloch Equations . . . 20

2 NFS in ^{229}Th:CaF_2 21
2.1 Modified couple laser Ω_c . . . 26
2.1.1 Square pulse . . . 26
2.1.2 Gaussian pulse . . . 27
2.2 Train of probe pulses . . . 28
2.2.1 Two-level system with $\Delta = 0$ . . . 28
2.2.2 Two-level system with $\Delta \neq 0$ . . . 29
2.2.3 Three-level system . . . 31
2.3 Applied static magnetic field . . . 31

3 The role of crystal structure and quantization axis 35
3.1 Lowest energy configuration: $\eta \neq 0$ . . . 38

II Electronic Bridge process in Doped Crystals 43

4 Theoretical Background for Electronic Bridge 45
4.1 Operators . . . 49
4.1.1 Nuclear operators . . . 49
4.1.2 Electronic operators . . . 49
4.1.3 Order of computation . . . 53

5 EB in Thorium-doped crystals 55

6 Excitation of the nuclear isomer 61
6.1 Direct photoexcitation . . . 61
6.2 *A*: EB starting in the electronic ground state . . . 63
6.3 *B*: EB starting from the color-center with energy greater than the isomer . . . 64
6.3.1 Stimulated Electronic Bridge . . . 66
6.4 C: EB starting from the color-center with energy less than the isomer . . . 69
6.4.1 Internal conversion from excited states . . . 71

7 Discussion of errors and approximations **73**
7.1 Benchmark with quasi-relativistic wave functions . . . 73
7.2 DFT wave functions of undefined (j, m_j) . . . 75
7.2.1 Checks based on selection rules . . . 75
7.2.2 Brute force checks: grid choice . . . 75
7.2.3 Brute force checks: intermediate states . . . 77

Conclusion & Outlook **79**

Appendix: Details in development **80**
A.1 Dynamical beat: ^{57}Fe . . . 81
A.2 Clebsch-Gordan coefficients, Wigner-Eckhart theorem . . . 83
A.3 Decay rate, linewidth and lifetime . . . 84
A.4 Weisskopf units . . . 85
A.5 Early time decay rate in NFS spectrum . . . 85
A.6 Introducing pulse phase shift in initial conditions . . . 86
A.7 Multipulsed excitation: superposition . . . 86
A.8 Electric field gradient . . . 87
A.9 Multipole radiation selection rules . . . 88
A.10 Multi-quantization axis calculations . . . 88
A.11 The spherical basis . . . 89
A.12 Computation of magnetic-dipole coupling operator . . . 89

Bibliography **93**

Acknowledgements **99**

Introduction

Today's global primary and secondary time standards are based on coherent light driving atomic transitions. However, efforts are underway to extend the clock physical systems to atomic nuclei. This development is based on a unique nuclear transition in the vacuum ultraviolet (VUV) range in the actinide nucleus ^{229}Th [1]. The first excited state of ^{229}Th is an isomer, i.e., a long-lived excited state, and lies at only $E_m = 8.28 \pm 0.17$ eV [2], being in the range of VUV lasers. The current prediction for the radiative lifetime of the isomeric state is in the region of hours [3]. Advantageous features of this isomeric transition towards the development of a nuclear clock include the very small ratio of radiative width to transition energy $\Gamma_\gamma / E_m \approx 10^{-20}$ and the isolation from external perturbations promising amazing stability [1, 4]. There have been two methods proposed for implementation of the nuclear clock, the first being with the use of trapped thorium ions [1, 5], and the second with thorium doped VUV-transparent crystals [6–8]. A review that addresses both methods can be found in [9]. Both approaches have their advantages, for instance, in the case of trapped ions our investigation would be free of impurities. On the other hand the crystal environment, although subject to impurities and line broadening due to interaction with the host crystal, allows for interrogation of a far greater number of nuclei at one time. Dopant density upwards of 10^{16} cm^{-3} [7, 10] can be achieved versus the approx 10^9 cm^{-3} seen for laser cooled Coulomb crystals that could be formed using ^{229}Th^{3+} ions [5, 11, 12]. The quantum instability of a clock is $\sigma \propto \Gamma/(E_m\sqrt{N})$ where N is the total number of atoms addressed and Γ the transition width [9, 13]. Thus, increased density achieved in the crystal environment could potentially lead to a clock with orders of magnitude more stability than with trapped ions.

At present, efforts in the development of a nuclear frequency standard are centered around a more accurate determination of the isomer state energy. At the start of this doctoral work, three years ago, the accepted value of the isomeric state was 7.8 ± 0.5 eV. This value dates back to indirect gamma-spectroscopy measurements performed in 2007 [14, 15]. Over the course of the last few years there have been many achievements in the thorium community including the first direct measurement of the excitation (however without providing information on the corresponding energy) [16, 17], as well as a new determination of thorium's isomeric energy, 8.28 ± 0.17 eV, by looking at the emission of internal conversion (IC) electrons from neutral thorium atoms [2]. Further experimental investigation of the IC process has been proposed to gain an even more accurate determination of the isomeric energy [18]. These new experimental measurements finally eliminate the waning idea that the isomeric state may not even exist.

Direct excitation of the isomeric state has proven difficult due to the exact feature that makes it so promising, its narrow linewidth. The ability to address a large number of ^{229}Th nuclei should lead to fluorescence rates sufficient for the use of broadband synchrotron light to directly measure the transition energy [6]. Therefore, in the following dissertation we will focus on the theoretical development of experimental approaches which make use of ^{229}Th-doped VUV-transparent crystals, where the larger nuclear density can be taken advantage of.

Due to their large band gap, crystals like CaF_2 or $LiCaAlF_6$ should be transparent in the region of the isomer energy [8]. In practice, several attempts of direct photoexcitation of the isomeric state with broadband light sources have been unsuccessful [10, 19, 20]. The two major sources of background that might cover the nuclear spectroscopy signal, namely VUV photoluminescence, caused by the probe light, and radioluminescence, caused by the radioactive decay of ^{229}Th and its daughters, have been investigated in [21]. Furthermore, attempted laser excitation can lead to crystal damage and the formation of defects. Even without laser induced damage, the act of doping thorium into CaF_2 and other VUV-transparent crystals results in localized electronic thorium states within the band gap of the crystal. These electronic states can be viewed as a crystal defect, and are referred to as color-center states [8, 22]. Both laser induced and damage intrinsic to the doping process can potentially decrease the transmission coefficient as well as adding parasitic signals in the relevant UV/VUV region [23, 24].

Since inhomogeneous broadening in the crystal lattice environment compromises the traditional

clock interrogation schemes, fluorescence spectroscopy was presented as an alternative [7]. A significant suppression of the inhomogeneous broadening is expected as long as all nuclei experience the same crystal lattice environment and are confined to the Lamb-Dicke regime, i.e., the recoilless transitions regime [6, 25]. However, theoretical work has shown that these very conditions lead to coherent light propagation through the sample and enhanced transient fluorescence in the forward direction, with a speed up of the initial decay (homogeneous broadening) depending primarily on the sample optical thickness [26]. These collective effects are actually well known from resonant coherent light scattering in different parameter regimes such as nuclear forward scattering (NFS) of synchrotron radiation [27] driving Mössbauer nuclear transitions in the x-ray regime, or from the interaction of atomic systems with visible and infrared light [28–30]. The coherent enhancement of the resonant scattering in the forward direction can be exploited for a more efficient excitation, but also in combination with additional electromagnetic fields can provide a specific signature of the nuclear excitation. First proposals in this direction have been discussed in [26, 31, 32].

In this work we go beyond the state of the art for NFS in thorium-doped crystals and investigate for the first time both spontaneous and stimulated Electronic Bridge (EB) processes in the crystal environment. NFS relies on direct photoexcitation of the thorium nuclei neglecting the electronic shell, and EB capitalizes on the interaction between nuclei and surrounding electrons to aid in excitation of the isomeric state. In the first part of this work we extend the study of collective effects for the ^{229}Th nuclear clock transition in VUV-transparent crystals and investigate theoretically several NFS excitation schemes involving one or two VUV laser fields and a combination of VUV laser field and external magnetic field. We go beyond the previous results in [26, 31, 32] to show that each excitation scheme requires analysis of the crystal structure and dopant orientation, which give information not only on the hyperfine structure of the levels to be driven, but also on the orientation of the possible quantization axes. The hyperfine structure determines the required energies to drive transitions as well as the angular momentum selection rules in the frame of each individual Th nucleus. Knowledge of the quantization axis, which can be different between dopant sites, determines which transitions will be driven in the bulk sample by a defined laser-pulse polarization in the laboratory frame. We identify setups for the excitation of the nuclear clock transition in ^{229}Th:CaF_2 and the correct interpretation of the experimental fluorescence spectra. We also investigate the role of phase relations between VUV laser pulses for efficient nuclear excitation by a pulse train. Our results show that the time interval between pulses, detuning, and phase difference play a critical role for the scattered spectra. A setup comprising of two crystal samples, one of which under the action of a moderate external magnetic field, is shown to provide the desired nuclear excitation signature due to interference effects and a clear signal also when using VUV pulse trains.

It is shown in Part I that narrowband excitation via NFS in the crystal environment has many advantages but must be reserved for future experiments when the transition energy is defined more accurately. Until that time, tuneable broadband lasers are being used to scan the energy region of interest in hopes of exciting the nuclear transition directly. Provided excitation is seen, such an experiment can determine the transition energy within the linewidth of the exciting laser. Thus there are two important trade-offs to consider: (1) between the time the experiment takes and the accuracy, and (2) between the lasers linewidth and the number of excitation photons with correct energy to drive the transition. Clearly to get the most accurate measurement we must excite the transition with a laser of small linewidth, however because the energy is not defined precisely, the smaller the linewidth the longer the time it takes to scan the energy region of interest. Using tuneable lasers with wider linewidth then has the issue of having fewer resonant photons and the risk of blindly passing over the transition energy increases. Much effort has been put towards broadband excitation of the isomeric state in the crystal environment [7, 8, 10, 19, 21, 33, 34], even still, progress has been slow and nuclear excitation has yet to be achieved. These broadband studies could instead be employed to characterize the electronic color-center states as these will be of utmost importance in the excitation method covered in the latter part of this dissertation.

In the second part of this dissertation, as a prequel to experimental implementation of NFS we investigate theoretically EB as a possible means to excite the isomer in the solid-state. EB may be more easily realized currently with ^{229}Th:CaF_2 and has not been considered inside the crystal environment until now. EB describes a process whereby the nucleus decays via transfer of energy to the electronic shell with the emission of a photon. This process can allow the decay or excitation to happen at a faster rate than would be seen with strictly the radiative decay channel.

The EB process and other closely related schemes have garnered interest recently when considering excitation of thorium ions where the IC channel is blocked [35–37]. Our goal is to understand if EB processes which cause such a drastic effect for ions [36, 38] can also be harnessed in the crystal environment for excitation purposes. In the literature, excitation of ^{229}Th in the crystal has gone

hand in hand with the assumption that both IC and other processes such as EB that affect the lifetime of the isomeric state do not occur. In the case of IC, this assumption has been warranted as thorium is usually in a charged state that prevents it from occurring based on the conservation of energy. In the case of EB however, the enhancement if any has not been quantified and thus the dominant decay rate inside the crystal has been assumed to be radiative.

Here we show how electronic color-center states, previously viewed as a hindrance in NFS, may be used to our advantage for EB excitation. A variety of bridge schemes can be used for nuclear excitation depending on the energy of the color-center and the available laser sources. The most promising EB schemes will be covered, where initial photoexcitation of valence electrons to color-center states will be the starting point for the most successful ones. We will consider initial color-center excitation using a VUV lamp which is currently in use for experimental investigation of ^{229}Th:CaF_2 [10]. Both excitation and decay of the isomer via EB are studied with an emphasis on schemes used for excitation. Two closely related schemes, labeled B^{st} and C, show the most promise in this regard. They both make use of the VUV lamp for initial electronic excitation to the color-center, in addition to lasers in the range of 1 W/(m^{2}Hz) to stimulate and drive the EB process respectively. To our knowledge, stimulated EB processes in the crystal will also be covered here for the first time. We discuss quenching of the excited isomer from two points of view. Firstly as a negative, which leads to lower occupation probability of the isomeric state. Secondly as a positive, where under certain circumstances can be controlled and triggered intentionally. These schemes provide excitation channels that can be upwards of 10^3 faster than direct photoexcitation with only the VUV lamp (depending on the energy of the color-center states).

This dissertation is structured in two parts, the first is dedicated to NFS and the second covers EB. Starting with Chapter 1, we outline the theory of the Maxwell-Bloch Equations (MBE) that allow us to calculate the NFS intensity spectrum. This chapter includes, in Section 1.1, a treatment of the Bloch equations which describe the effect of a given field on a multilevel system. All transformations and approximations used for their computation are outlined here. This is then expanded upon in Section 1.2 with the introduction of Maxwell's equations to describe the impact the changing excitation in the multilevel system has on the exciting field. This is followed by a discussion of required initial conditions, resulting in the final set of equations used for the theoretical calculation of NFS spectrum, as presented in Section 1.3. In Chapter 2, the theoretical quantum optics model based on the MBE is put to work for the pulse propagation through the ^{229}Th:CaF_2 crystal. The most relevant features of coherent excitation of ^{229}Th in crystal environment along with the importance of the quantization axis are introduced. Our analysis allows for the simplification of the multilevel systems into two and three-level systems showing both the enhancement of the radiative decay as well as the quantum beat signature in the case of the three-level system. Numerical results for excitation schemes using one pulsed and one continuous-wave VUV laser in different configurations are presented followed by a discussion of pulse shape and repetition rate for the realization of an effective continuous-wave laser as it applies to NFS in Section 2.1. Nuclear excitation with a pulse train is investigated along with the interplay between phase relation, detuning and pulse spacing in Section 2.2. Section 2.3 considers a two-crystal setup with a static magnetic field. Chapter 3 outlines important details of crystal structure including dopant orientation, quantization axis, and state mixing. This then defines the energy requirements for which the results shown in Chapter 2 are valid.

Part II presents our work on EB in the crystal. Chapter 4 outlines the theory of EB along with all required operators in their non-relativistic form and our computational method. Chapter 5 discusses the application of EB, first defined for ions, to the doped crystal environment. Here too is a discussion of the electronic color-center states most important for the EB process in ^{229}Th:CaF_2, and the computation of their wave functions. Chapter 6 presents numerical results and estimations for the decay and excitation rate of the isomeric state via various EB schemes. This begins in Section 6.1 with a discussion of direct photoexcitation of both the isomer and electronic color-center independently. Sections 6.2-6.4 then outline three EB schemes for excitation including discussion of laser stimulation and comparison to direct photoexcitation of the isomer without EB. The final two EB schemes studied, labeled B_{st} and C, make use of a VUV lamp for initial excitation of the color-center as well as a second laser of energy equal to the difference between the color-center and the isomer. The main difference between B_{st} and C is that the color-center states are assumed above and below the isomer in energy, respectively. These are the most promising EB schemes presented and could provide an enhancement upwards of 10^3 in excitation when compared to direct photoexcitation of the isomer with the same VUV lamp. Chapter 7 outlines the benchmarking measures taken during calculation of EB rates and wave functions along with a discussion of errors due to the choice of a discrete three-dimensional grid and the summation over intermediate states required for EB rate calculation.

These two parts are brought to an end with the conclusions and outlook, followed by appendices which outline details of assumptions and equations used throughout the work.

Part I

Nuclear Forward Scattering in Thorium-Doped Crystals

Chapter 1

Theoretical background for Nuclear Forward Scatting (NFS)

The goal of this work is to investigate the excitation of thorium's isomeric state within the crystal environment. Our first approach is Nuclear Forward Scattering (NFS). Unlike fluorescence spectroscopy which relies on measuring spontaneous decay photons with spatial distribution of 4π, NFS signal is emitted in the forward direction defined by the optical axis of the exciting laser. The photons measured in NFS are the result of superradiant decay, post excitation, of a collection of identical particles which in our case are the thorium nuclei. In the field of NFS, collective effects refer to the formation of a delocalized excitation extended over a large part of the sample. This delocalized excitation, which typically does not contain more than one single excited nucleus, is also known as "nuclear exciton" and resembles a Dicke state [39]. The formation of the exciton requires the indiscernibility of the possible scattering paths, i.e., recoilless transitions, no spin flips or internal conversion. This is the case of coherent scattering when the nuclei return to their initial state, such that the scattering path and the number of occurred events are unknown.

The decay of the collective excitation happens via a complicated temporal structure known as the dynamical beat, which presents a speed-up decay at short times immediately after the excitation and additional damping and oscillations at later times. The dynamical beat can be very different from the natural decay of a single nucleus. Its origin is related to the process of coherent multiple scattering of a single resonant photon in the sample. At early times the NFS decay happens up to a factor $\xi = N\sigma L/4$ faster than the spontaneous decay rate, where N is the number density of active nuclei in the crystal, σ the resonant cross section and L the thickness of the sample. The possibility to generate crystals with thorium-dopant densities $N > 10^{16}$ cm^{-3} has been achieved [7, 10] suggesting that a significant enhancement factor could be expected. The dynamical beat along with the speed-up effect and emission in the forward direction were initial motivations for our investigation into NFS. Note that in our numerical results, the dynamical beat feature is not obvious when looking at the graphs because the decay due to the decoherence rates is the dominant component on the time scale of interest. As an example, the dynamical beat is compared to the quantum beat in Appendix A.1 for the standard ^{57}Fe sample.

In comparison with typical atomic physics superradiance, the collective effects in nuclear ensembles have to take into account two peculiarities. First, the condition that the wavelength is much larger than the internuclear distance often does not hold, since typically nuclear transitions are in the range of tens or hundreds of keV energy. ^{229}Th is an exception, with the wavelength at ~ 150 nm. Second, the induced nuclear excitation is very small, i.e., typically one or very few nuclei are excited. This is in contrast to typical atomic superradiance effects which become most pronounced when approximately half of the atoms are excited. A quite comprehensive review on the topic of nuclear excitons and collective effects in nuclear condensed-matter physics is given in [27].

The experimental setup for NFS is illistrated in Figure 1.1, where a detector placed along the optical axis records the intensity and time delay between decay photons from the sample and the exciting laser pulses. This can be done provided the exciting laser pulse has a width much less than the decay rate of the sample, $\delta \ll 1/\Gamma$. The final NFS spectrum is a plot of intensity of the decay photons emitted in the forward direction versus the time delay between arrival of the excitation pulse and the decay photon respectively on the detector. The spectrum is thus built up from the result of many trials, whereby an excitation pulse is sent through the sample and one looks for decay photons. The number of trials required to build up the final intensity spectrum

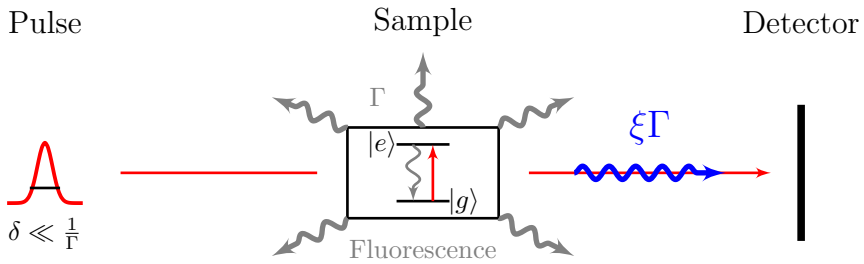

Figure 1.1: Depiction of typical NFS setup. A pulsed laser with temporal width $\delta \ll 1/\Gamma$ excites a collective excitation in the sample. The collective excitation decays in the forward direction. The enhanced rate at early time after excitation is $\xi\Gamma$.

will depend on the strength of the excitation generated in the sample. For low excitation rates each trial may yield only a single point in the final NFS time spectrum. The level structure driven in NFS can be far more complicated than the simple two-level system depicted in Figure 1.1. Furthermore, several lasers can be used on multilevel systems to generate different signatures in the NFS spectrum beyond the dynamical beat.

As discussed above, the measured quantity in an NFS experiment is the intensity of the emitted photons after excitation with a laser pulse. Our calculation must then consider not only the effect of the applied field on the system but also the effect of the system on the field [40, p164]. For this we must introduce equations for the evolution of the field to be solved self-consistently with those of the collection of particles (thorium nuclei) in the sample. The set of equations are called Maxwell-Bloch Equations (MBE). As the name suggests, the MBE combine Maxwell's equations which describe the applied field and the Bloch equations which describe the changing level populations in the sample. The combination describe the evolution of the field during its interaction with the sample.

Starting in Section 1.1 the Bloch equations for the two-level system will be covered which provides a base from which we can expand the notation to cover all other more complicated systems. Section 1.2 then introduces equations for the exciting laser field and its interaction with the sample described by the previously outline Bloch equations. By solving the MBE, one can then plot the NFS time spectrum, where the intensity is proportional to the square of the exciting field amplitude, $I \propto |\mathscr{A}|^2$. Furthermore it is shown that the exciting field amplitude is proportional to the Rabi frequency $\mathscr{A} \propto \Omega$ and thus $I \propto |\Omega|^2$.

We note here that solving the MBE is an equivalent approach to the iterative field equation method commonly used in NFS to describe the coherent scattering and so-called collective effects in coherent light propagation [41–43].

1.1 Bloch equations

The simplest case is to consider the interaction of a single quantum-optical two-level system[1] with a single-mode field [40, ch.5] [44, ch.15] [45, 46]. We seek a solution to the Hamiltonian of our system $\hat{H}$, as a linear combination of states of the unperturbed Hamiltonian $\hat{H}_0$,

$$|\psi(t)\rangle = c_1(t)|1\rangle + c_2(t)|2\rangle \tag{1.1}$$

where $\hat{H}_0|n\rangle = \hbar\omega_n|n\rangle$, $\hbar$ the reduced Planck constant, and $n \in \{1, 2\}$. The density matrix is written as

$$\begin{aligned} \hat{\rho} &= |\psi\rangle\langle\psi|, & (1.2)\\ &= \begin{pmatrix} \rho_{11} & \rho_{12} \\ \rho_{21} & \rho_{22} \end{pmatrix}, & (1.3)\\ &= \begin{pmatrix} c_1^2 & c_1 c_2^* \\ c_2 c_1^* & c_2^2 \end{pmatrix}. & (1.4) \end{aligned}$$

[1] Our particular application will be concerned with two-level nuclei, however, the Bloch equations can be used to describe any two-level particle or group of particles where the applied field is not significantly affected by whatever excitation is induced. In other words, the number of resonant photons is far greater than the number of particles taking part in the excitation process. If the field becomes significantly affected one must move on to solving the MBE for the system.

Expressing the unperturbed Hamiltonian in matrix form we make use of the identity operator for the two-level system

$$\hat{H}_0 = (|1\rangle\langle 1| + |2\rangle\langle 2|)\hat{H}_0(|1\rangle\langle 1| + |2\rangle\langle 2|) \tag{1.5}$$

$$= \begin{pmatrix} \hbar\omega_1 & 0 \\ 0 & \hbar\omega_2 \end{pmatrix}. \tag{1.6}$$

The perturbing Hamiltonian is the result of the interaction of the impinging laser field with the two-level system. The form of this potential depends on the transition in question. The interaction Hamiltonian can be written in the most general form as

$$\hat{H}_{int} = -\frac{1}{c}\int \boldsymbol{j}(\boldsymbol{r},t)\cdot\boldsymbol{A}(\boldsymbol{r},t)\ \mathrm{d}^3r, \tag{1.7}$$

where $\boldsymbol{j}(\boldsymbol{r},t)$ is the nuclear charge current and $\boldsymbol{A}(\boldsymbol{r},t)$ the vector potential of the laser field. Typically the interaction Hamiltonian can be expanded into nuclear multipole moments and particular terms selected according to the driven transition. For simplicity we consider an electric dipole (E1) transition[2], the potential of which can be written as[3]

$$\hat{H}_{int} \to \hat{V} = -\boldsymbol{d}_i\cdot\boldsymbol{E}(\boldsymbol{r}_i,t), \tag{1.8}$$

where $\boldsymbol{d}_i$ is the electric dipole moment operator of our two-level atom i, and $\boldsymbol{E}(\boldsymbol{r}_i,t)$ the electric field evaluated at the position of that atom $\boldsymbol{r}_i$.

Given a dipole moment $\boldsymbol{d}_i = ex\,\hat{\boldsymbol{x}}$, where $\hat{\boldsymbol{x}} = \boldsymbol{x}/|\boldsymbol{x}|$ is the unit polarization vector, we can define a monochromatic electric field $\boldsymbol{E}(\boldsymbol{r}_i,t) = \mathscr{E}\cos(\nu t)\,\hat{\boldsymbol{x}}$ polarized along $\hat{\boldsymbol{d}}_i$. With this impinging monochromatic electric field polarized linearly along the same direction as the electric dipole moment operator, the interaction Hamiltonian becomes,

$$\hat{V} = -exE(t) \tag{1.9}$$

$$= -e(|1\rangle\langle 1| + |2\rangle\langle 2|)x(|1\rangle\langle 1| + |2\rangle\langle 2|)E(t) \tag{1.10}$$

$$= \begin{pmatrix} 0 & -e\langle 1|x|2\rangle E(t) \\ -e\langle 2|x|1\rangle E(t) & 0 \end{pmatrix}. \tag{1.11}$$

where the spatial parameter is dropped in the notation, $E(\boldsymbol{r}_i,t) = E(t) = \mathscr{E}\cos(\nu t)$. The total Hamiltonian of the system is thus a sum of the unperturbed and interaction Hamiltonians, $\hat{H} = \hat{H}_0 + \hat{V}$.

The master equation[4] that determines the dynamics of the level densities is given by

$$\partial_t\hat{\rho} = \frac{1}{i\hbar}[\hat{H},\hat{\rho}]. \tag{1.12}$$

In addition to this one must introduce a relaxation term

$$\hat{\rho}_r = -\sum_{n,m}\langle m|\hat{\Gamma}^{in}|n\rangle\left(\frac{1}{2}|n\rangle\langle n|\hat{\rho} + \frac{1}{2}\hat{\rho}|n\rangle\langle n| - |m\rangle\langle n|\hat{\rho}|n\rangle\langle m|\right) - \frac{1}{2}\{\hat{\Gamma}^{ex},\hat{\rho}\}, \tag{1.13}$$

which allows for internal decay between levels within the system and external decay to and from the system [40, p161] [49, p281] [50, p32] [51] not covered in the Hamiltonian $\hat{H}$. The internal relaxation is controlled by $\hat{\Gamma}^{in}$, i.e., between levels in the considered system, and $\hat{\Gamma}^{ex}$ controls external relaxation, i.e., from a level in the considered system to some level outside the system or vice versa, where $\{\hat{A},\hat{B}\} = \hat{A}\hat{B} + \hat{B}\hat{A}$ is the anticommutator. The relaxation matrices take the form $\langle m|\hat{\Gamma}^{ex}|n\rangle = \gamma_n\delta_{mn}$, $\langle m|\hat{\Gamma}^{in}|n\rangle = \gamma_{mn}(1-\delta_{mn})$, where γ_n is the relaxation rate of level $|n\rangle$ to any level outside the considered system, and γ_{mn} is the internal relaxation rate from level $|n\rangle \to |m\rangle$. Other notation can be used for computation[5].

[2] See [45, p202] for potential for other types of transitions.

[3] Diagonal elements are zero [46, p35] [47] due to parity selection rules [48, p98].

[4] Also referred to as the Liouville or von Neumann equation of motion.

[5] For computation we can rewrite (1.13) using the matrix

$$\sigma(n,m) = \begin{array}{c} \\ \\ \\ \\ \\ \\ \end{array}\begin{array}{c} \begin{array}{ccc} & & m \\ & & \downarrow \end{array} \\ \begin{pmatrix} \ddots & \cdots & & & & & \\ \vdots & & & & & & \\ & & 0 & 0 & 0 & & \\ & & 0 & 1 & 0 & & \\ & & 0 & 0 & 0 & & \\ & & & & & \ddots & \end{pmatrix} \end{array} \begin{array}{l} \\ \\ \\ \\ \leftarrow n \\ \\ \end{array}$$

The master equation is then,

$$\partial_t\hat{\rho} = \frac{1}{i\hbar}[\hat{H},\hat{\rho}] - \sum_{n,m}^{2}\gamma_{mn}\left(\frac{1}{2}|n\rangle\langle n|\hat{\rho} + \frac{1}{2}\hat{\rho}|n\rangle\langle n| - |m\rangle\langle n|\hat{\rho}|n\rangle\langle m|\right) - \frac{1}{2}\{\hat{\Gamma}^{ex},\hat{\rho}\}. \tag{1.14}$$

This set of equations are called the Bloch equations, written out here for our two-level system

$$\dot{\rho}_{11} = \frac{i}{\hbar}(V_{21}\rho_{12} - V_{12}\rho_{21}) - \gamma_{21}\rho_{11} + \gamma_{12}\rho_{22} - \gamma_1\rho_{11}, \tag{1.15}$$

$$\dot{\rho}_{21} = -\frac{i}{\hbar}V_{21}(\rho_{11} - \rho_{22}) - \left(i(\omega_2 - \omega_1) + \frac{1}{2}\gamma_{12} + \frac{1}{2}\gamma_{21} + \frac{1}{2}(\gamma_1 + \gamma_2)\right)\rho_{21}, \tag{1.16}$$

$$\dot{\rho}_{22} = -\frac{i}{\hbar}(V_{21}\rho_{12} - V_{12}\rho_{21}) + \gamma_{21}\rho_{11} - \gamma_{12}\rho_{22} - \gamma_2\rho_{22}, \tag{1.17}$$

where $\rho_{12} = \rho_{21}^*$ and it is understood that the potential energy, the density matrix elements and their rate of change are functions of position and time. Ignoring the effect of the applied potential, if we only allow for the decay of level population then terms relating to excitation, $\{\gamma_{mn}|m > n\}$, are set to zero. Furthermore, we can impose a closed system by setting all external relaxation rates γ_n to zero.

1.1.1 Unitary transformations and the Rotating-Wave Approximation (RWA)

Interaction picture

Before implementation of the Bloch equations, we make use of the Rotating-Wave Approximation (RWA) which is more easily demonstrated in the interaction picture [40, p155]. Given the Schrödinger equation,

$$i\hbar\partial_t|\psi(t)\rangle = \hat{H}|\psi(t)\rangle \tag{1.18}$$

we define a new state vector

$$|\tilde{\psi}(t)\rangle = \hat{U}^\dagger(t)|\psi(t)\rangle \tag{1.19}$$

where $\hat{U}^\dagger(t) = e^{i\hat{A}t/\hbar}$ is a unitary transformation. To have $|\tilde{\psi}(t)\rangle$ satisfy the Schrödinger equation we solve the time evolution to find the form of the new Hamiltonian[6]

$$\begin{aligned} i\hbar\partial_t|\tilde{\psi}\rangle &= i\hbar\partial_t\hat{U}^\dagger|\psi\rangle + i\hbar\hat{U}^\dagger\partial_t|\psi\rangle \\ &= i\hbar\partial_t\hat{U}^\dagger\hat{U}|\tilde{\psi}\rangle + \hat{U}^\dagger\hat{H}|\psi\rangle \\ &= \left(i\hbar\partial_t\hat{U}^\dagger\hat{U} + \hat{U}^\dagger\hat{H}\hat{U}\right)|\tilde{\psi}\rangle. \end{aligned} \tag{1.20}$$

Hence, the Hamiltonian in this new picture[7] is given by $\hat{\tilde{H}} = i\hbar\partial_t\hat{U}^\dagger\hat{U} + \hat{U}^\dagger\hat{H}\hat{U}$. All other operators are then given by the typical transformation $\hat{\tilde{O}} = \hat{U}^\dagger\hat{O}\hat{U}$.

The interaction picture is found by choosing $\hat{U} = \hat{U}_0 = e^{-i\hat{H}_0t/\hbar}$, i.e., the unitary time-evolution operator. For the two-state system $\hat{U}_0 = e^{-i\omega_1t}|1\rangle\langle 1| + e^{-i\omega_2t}|2\rangle\langle 2|$ and thus, the density matrix transforms to

$$\hat{\rho}_I = \begin{pmatrix}\tilde{\rho}_{11} & \tilde{\rho}_{12}\\ \tilde{\rho}_{21} & \tilde{\rho}_{22}\end{pmatrix} = \begin{pmatrix}\rho_{11} & e^{-i\omega t}\rho_{12}\\ e^{i\omega t}\rho_{21} & \rho_{22}\end{pmatrix}, \tag{1.21}$$

$$\langle i|\sigma(n,m)|j\rangle = \delta_{in}\delta_{jm},$$

which serves the purpose of a raising and lowering operator on the state, $\sigma(n,m)|m\rangle = |n\rangle$, giving

$$\hat{\rho}_r = -\sum_{n,m}\langle m|\hat{\Gamma}^{in}|n\rangle\left(\frac{1}{2}\sigma(n,n)\hat{\rho} + \frac{1}{2}\hat{\rho}\sigma(n,n) - \sigma(m,n)\hat{\rho}\sigma(n,m)\right) - \frac{1}{2}\{\hat{\Gamma}^{ex},\hat{\rho}\}.$$

[6] Dropping the explicit time dependence for notational simplicity.

[7] Converting back to the Schrödinger picture is done simply by inverse operation

$$\begin{aligned}\hat{H} &= \hat{U}\hat{\tilde{H}}\hat{U}^\dagger - i\hbar\hat{U}\partial_t\hat{U}^\dagger,\\ \hat{O} &= \hat{U}\hat{\tilde{O}}\hat{U}^\dagger.\end{aligned}$$

where $\omega = \omega_2 - \omega_1$ and $\tilde{\rho}_{ij}$ denote the density matrix elements in the transformed picture[8].

Simplifying the Hamiltonian we find

$$\begin{aligned} \hat{H}_I &= i\hbar\partial_t \hat{U}_0^\dagger \hat{U}_0 + \hat{U}_0^\dagger \hat{H} \hat{U}_0 \\ &= \hat{U}_0^\dagger \hat{V} \hat{U}_0 \end{aligned} \tag{1.22}$$

hence, it is clear that the interaction picture is the one in which the unperturbed Hamiltonian is zero. As a result,

$$\hat{H}_I = \begin{pmatrix} 0 & e^{-i(\omega_2-\omega_1)t} V_{12} \\ e^{i(\omega_2-\omega_1)t} V_{21} & 0 \end{pmatrix}. \tag{1.23}$$

At this point we must consider the form of the applied field. Here we assume a monochromatic applied field polarized in the direction of $\boldsymbol{d}$, as done in the last section, $\boldsymbol{E}(\boldsymbol{r}_i, t) = \mathscr{E} \cos(\nu t)\, \hat{\boldsymbol{x}}$ and $\hat{\boldsymbol{d}}_i = ex\, \hat{\boldsymbol{x}}$. We can then expand the form of the perturbing Hamiltonian

$$\hat{V} = -(d_{21}|2\rangle\langle 1| + d_{21}^*|1\rangle\langle 2|)\mathscr{E}\cos(\nu t) \tag{1.24}$$

$$= -\frac{\hbar}{2}\left(\Omega|2\rangle\langle 1| + \Omega^*|1\rangle\langle 2|\right)\left(e^{i\nu t} + e^{-i\nu t}\right), \tag{1.25}$$

where the Rabi frequency for the $j \to i$ transition is defined in general by

$$|\hbar\Omega_{ij}|^2 = \left\{|\langle i|\hat{V}|j\rangle|^2\right\} = \frac{1}{T}\int_0^T |\langle i|\hat{V}|j\rangle|^2 \,\mathrm{d}t. \tag{1.26}$$

Here $\hat{V}$ is the interaction Hamiltonian[9] and the curly braces denote a time average over optical period T [45, p.175]. For this specific case of electric dipole interaction

$$\begin{aligned} \frac{1}{T}\int_{-T}^{T} |\langle i|\hat{V}|j\rangle|^2 \,\mathrm{d}t &= \frac{1}{T}\int_{-T}^{T} |\langle i|\boldsymbol{d}|j\rangle \cdot \boldsymbol{E}|^2 \,\mathrm{d}t \\ &= |d_{21}\mathscr{E}|^2 \frac{1}{T}\int_{-T}^{T} \cos^2(\nu t)\,\mathrm{d}t \\ &= |d_{21}\mathscr{E}|^2. \end{aligned} \tag{1.27}$$

resulting in,

$$\Omega_{21} = \frac{d_{21}\mathscr{E}}{\hbar}. \tag{1.28}$$

Substituting into (1.23),

$$\hat{H}_I = -\frac{\hbar}{2}\begin{pmatrix} 0 & \Omega^*(e^{-i(\omega+\nu)t} + e^{-i\Delta t}) \\ \Omega(e^{i(\omega+\nu)t} + e^{i\Delta t}) & 0 \end{pmatrix} \tag{1.29}$$

where $\Delta = \omega - \nu$. In the Rotating-Wave Approximation the $e^{\pm i(\omega+\nu)t}$ terms are dropped because we assume driving the transition close to its resonance frequency $\nu \approx \omega$. This is strictly a mathematical argument as these terms are highly oscillatory and centred on zero. Thus, upon integration to find the occupation probability[10], their contribution tends to zero compared to that of the slowly oscillating $e^{\pm i\Delta t}$ terms. Hence we have,

$$\hat{H}_I \overset{RWA}{\approx} -\frac{\hbar}{2}\begin{pmatrix} 0 & \Omega^* e^{-i\Delta t} \\ \Omega e^{i\Delta t} & 0 \end{pmatrix}. \tag{1.30}$$

[8] To prevent cluttered notation, only a distinction between the Schrodinger picture density matrix elements ρ_{ij} and the transformed density matrix elements $\tilde{\rho}_{ij}$ will be made. Refer to the text for details on the exact transformation used. In this case for example, $\tilde{\rho}_{ii} = \rho_{ii}$.

[9] Not to be confused with the full Hamiltonian transformed into the interaction picture $\hat{H}_I$.

[10] Given by the density matrix, ρ.

The resulting Bloch equations in the RWA are then[11],

$$\dot{\rho}_{11} = -\frac{i}{2}(\Omega e^{i\Delta t}\tilde{\rho}_{12} - \Omega^* e^{-i\Delta t}\tilde{\rho}_{21}) - \gamma_{21}\rho_{11} + \gamma_{12}\rho_{22} - \gamma_1\rho_{11}, \tag{1.31}$$

$$\dot{\tilde{\rho}}_{21} = \frac{i}{2}\Omega e^{i\Delta t}(\rho_{11} - \rho_{22}) - \left(\frac{1}{2}\gamma_{12} + \frac{1}{2}\gamma_{21} + \frac{1}{2}(\gamma_1 + \gamma_2)\right)\tilde{\rho}_{21}, \tag{1.32}$$

$$\dot{\rho}_{22} = \frac{i}{2}(\Omega e^{i\Delta t}\tilde{\rho}_{12} - \Omega^* e^{-i\Delta t}\tilde{\rho}_{21}) + \gamma_{21}\rho_{11} - \gamma_{12}\rho_{22} - \gamma_2\rho_{22}. \tag{1.33}$$

Alternate picture

The interaction picture is particularly useful to understand the RWA and which terms to drop to make this approximation. However, other unitary transformations can be used to achieve a more appealing form. Even still, the resulting sets of equations are equivalent when solved, provided the same approximations are made. The form of the terms that have to be dropped when making the RWA will change depending on the form of the unitary transformation. In all cases however, it is the fast oscillating terms that are neglected.

As an example of an alternate picture, we first define the lowest state energy in the system as zero and reference all other energies to it, hence

$$\hat{H} = \begin{pmatrix} 0 & V_{12} \\ V_{21} & \hbar\omega \end{pmatrix}. \tag{1.34}$$

Then we define the unitary transformation using[12]

$$\hat{U} = \begin{pmatrix} 1 & 0 \\ 0 & e^{-i\nu t} \end{pmatrix} \tag{1.36}$$

where ν is the resonant driving frequency for, in this case, the $1 \leftrightarrow 2$ transition. Which gives the transformed density matrix as

$$\hat{\tilde{\rho}} = \begin{pmatrix} \tilde{\rho}_{11} & \tilde{\rho}_{12} \\ \tilde{\rho}_{21} & \tilde{\rho}_{22} \end{pmatrix} = \begin{pmatrix} \rho_{11} & e^{-i\nu t}\rho_{12} \\ e^{i\nu t}\rho_{21} & \rho_{22} \end{pmatrix}, \tag{1.37}$$

and Hamiltonian

$$\hat{\tilde{H}} = \begin{pmatrix} 0 & e^{-i\nu t}V_{12} \\ e^{i\nu t}V_{21} & \hbar\Delta \end{pmatrix}, \tag{1.38}$$

where $\Delta = \omega - \nu$. As before we assume linearly polarized light, hence, to make the RWA in this picture we expand V and drop the $e^{\pm 2i\nu t}$ terms giving,

$$\hat{\tilde{H}} \overset{RWA}{\approx} -\frac{\hbar}{2}\begin{pmatrix} 0 & \Omega^* \\ \Omega & -2\Delta \end{pmatrix}. \tag{1.39}$$

[11] Before notational substitution

$$\partial_t \dot{\rho}_I = \begin{pmatrix} \dot{\tilde{\rho}}_{11} & \dot{\tilde{\rho}}_{12} \\ \dot{\tilde{\rho}}_{21} & \dot{\tilde{\rho}}_{22} \end{pmatrix} = \begin{pmatrix} \dot{\rho}_{11} & -i\omega e^{-i\omega t}\rho_{12} + e^{-i\omega t}\dot{\rho}_{12} \\ i\omega e^{i\omega t}\rho_{21} + e^{i\omega t}\dot{\rho}_{21} & \rho_{22} \end{pmatrix},$$

$$\begin{aligned} \dot{\rho}_{11} &= \frac{i}{\hbar}(V_{21}\rho_{12} - V_{12}\rho_{21}) - \gamma_{21}\rho_{11} + \gamma_{12}\rho_{22} - \gamma_1\rho_{11}, \\ \dot{\tilde{\rho}}_{21} &= e^{i\omega t}\left(-\frac{i}{\hbar}V_{21}(\rho_{11} - \rho_{22}) - \left(\frac{1}{2}\gamma_{12} + \frac{1}{2}\gamma_{21} + \frac{1}{2}(\gamma_1 + \gamma_2)\right)\rho_{21}\right), \\ \dot{\rho}_{22} &= -\frac{i}{\hbar}(V_{21}\rho_{12} - V_{12}\rho_{21}) + \gamma_{21}\rho_{11} - \gamma_{12}\rho_{22} - \gamma_2\rho_{22}. \end{aligned}$$

[12] For a larger system this unitary transformation is given by [52]

$$\hat{U} = \begin{pmatrix} 1 & 0 & \cdots & \\ 0 & e^{-i\nu_2 t} & & \\ \vdots & & \ddots & \\ & & & e^{-i\nu_n t} \end{pmatrix} \tag{1.35}$$

where ν_n are the resonant driving frequency for that level, i.e., at resonance $\omega_n = \nu_n$. This will be referred to as the resonant driving unitary transformation.

The resulting Bloch equations in the RWA are then

$$\dot{\rho}_{11} = -\frac{i}{2}(\Omega\tilde{\rho}_{12} - \Omega^*\tilde{\rho}_{21}) - \gamma_{21}\rho_{11} + \gamma_{12}\rho_{22} - \gamma_1\rho_{11}, \tag{1.40}$$

$$\dot{\tilde{\rho}}_{21} = \frac{i}{2}\Omega(\rho_{11} - \rho_{22}) - \left(i\Delta + \frac{1}{2}\gamma_{12} + \frac{1}{2}\gamma_{21} + \frac{1}{2}(\gamma_1 + \gamma_2)\right)\tilde{\rho}_{21}, \tag{1.41}$$

$$\dot{\rho}_{22} = \frac{i}{2}(\Omega\tilde{\rho}_{12} - \Omega^*\tilde{\rho}_{21}) + \gamma_{21}\rho_{11} - \gamma_{12}\rho_{22} - \gamma_2\rho_{22}, \tag{1.42}$$

which are equivalent the set we found in the last section. The unitary transformation used is somewhat arbitrary, with the goal being to simplify the form of the Bloch equations. As such, the form of the unitary transformation used can change depending on the system in question, and on how we wish to simplify the Bloch equations.

1.1.2 Two-state system

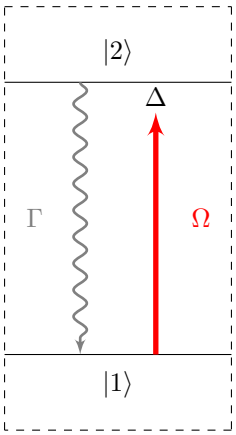

Figure 1.2: Schematic of the two-state system. We use the notation, ground state $|1\rangle$, excited state $|2\rangle$, decay rate Γ, Rabi frequency Ω due to laser with detuning Δ.

Simplifying the two-state electric-dipole system driven by a single linear polarized field and allowing for only internal decay channels is depicted in Figure 1.2 and represented by the set of equations,

$$\begin{aligned}
\partial_t\hat{\rho} &= \frac{1}{i\hbar}[\hat{H}, \hat{\rho}] + \hat{\rho}_r, \\
\hat{\rho} &= \begin{pmatrix} \rho_{11} & \tilde{\rho}_{12} \\ \tilde{\rho}_{21} & \rho_{22} \end{pmatrix}, \\
\hat{H} &= -\frac{\hbar}{2}\begin{pmatrix} 0 & \Omega^* \\ \Omega & -2\Delta \end{pmatrix}, \\
\Omega &= \frac{2}{\hbar}|\langle 2|\hat{H}|1\rangle|, \\
\hat{\rho}_r &= -\frac{\Gamma}{2}\begin{pmatrix} -2\rho_{22} & \tilde{\rho}_{12} \\ \tilde{\rho}_{21} & 2\rho_{22} \end{pmatrix}.
\end{aligned}$$

The resulting Bloch equations are

$$\begin{aligned}
\dot{\rho}_{11} &= -\frac{i}{2}(\Omega\tilde{\rho}_{12} - \Omega^*\tilde{\rho}_{21}) + \Gamma\rho_{22}, \\
\dot{\tilde{\rho}}_{21} &= \frac{i}{2}\Omega(\rho_{11} - \rho_{22}) - \left(i\Delta + \frac{1}{2}\Gamma\right)\tilde{\rho}_{21}, \\
\dot{\rho}_{22} &= \frac{i}{2}(\Omega\tilde{\rho}_{12} - \Omega^*\tilde{\rho}_{21}) - \Gamma\rho_{22}.
\end{aligned}$$

The effect of the decay rate, Γ, and detuning of the laser field, Δ, can then be seen by plotting the excited state occupation probabilty as a function of time, as shown in Figures 1.3 and 1.4.

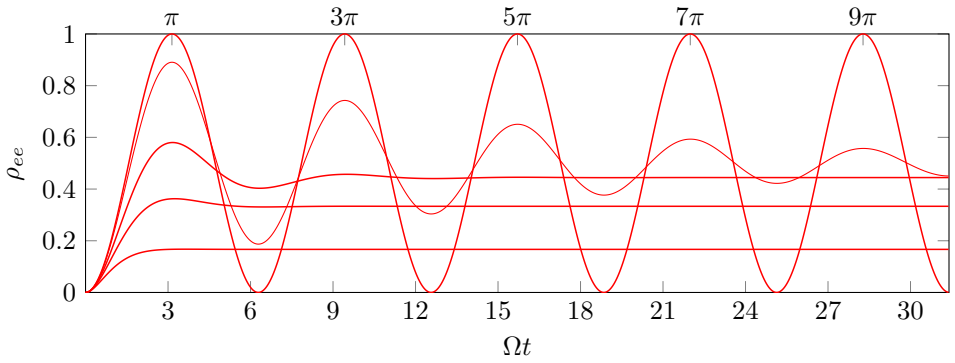

Figure 1.3: Occupation probability of the excited state, ρ_{22}, for various decay rates $\Gamma = \Omega \cdot \{0, 0.1, 0.5, 1, 2\}$. We consider the Rabi frequency $\Omega = 1$ and detuning $\Delta = 0$.

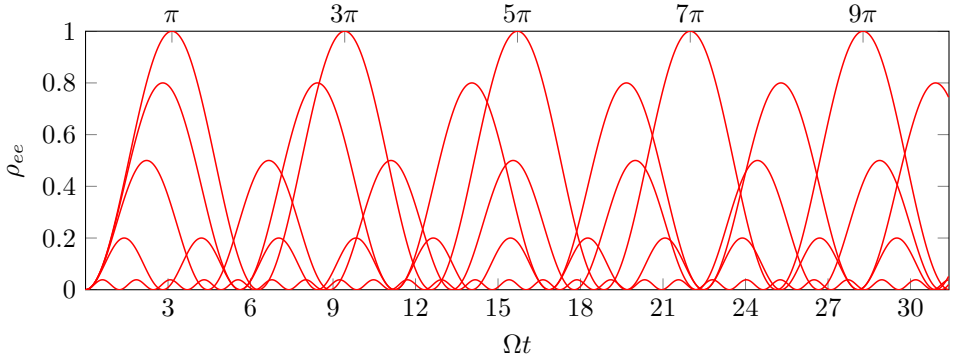

Figure 1.4: Occupation probability of the excited state, ρ_{22}, for various detunings $\Delta = \Omega \cdot \{0, 0.5, 1, 2, 5\}$. We consider the Rabi frequency $\Omega = 1$, and decay rate $\Gamma = 0$.

1.2 Maxwell's field equation

Bloch equations can be used to understand the changing population[13] of levels in the system. Now we would like to know how this changing excitation impacts the output field. Namely, how does the changing population affect the Hamiltonian $\hat{H}$.

The starting point is Maxwell's macroscopic equations [40, 53], given here in SI units,

$$\boldsymbol{\nabla} \cdot \boldsymbol{D} = \rho_f, \tag{1.43}$$
$$\boldsymbol{\nabla} \cdot \boldsymbol{B} = 0, \tag{1.44}$$
$$\boldsymbol{\nabla} \times \boldsymbol{E} = -\frac{\partial \boldsymbol{B}}{\partial t}, \tag{1.45}$$
$$\boldsymbol{\nabla} \times \boldsymbol{H} = \boldsymbol{J}_f + \frac{\partial \boldsymbol{D}}{\partial t}, \tag{1.46}$$

where

$$\boldsymbol{D} = \epsilon_0 \boldsymbol{E} + \boldsymbol{P}, \tag{1.47}$$
$$\boldsymbol{H} = \frac{1}{\mu_0} \boldsymbol{B} - \boldsymbol{M}, \tag{1.48}$$
$$\boldsymbol{J}_f = \sigma \boldsymbol{E}. \tag{1.49}$$

In the equations above, $\boldsymbol{E}$ is the electric field, $\boldsymbol{B}$ is the magnetic field, with $\boldsymbol{D}$ and $\boldsymbol{H}$ their auxiliary fields, respectively[14], $\boldsymbol{P}$ and $\boldsymbol{M}$ are the macroscopic polarization[15] and magnetization respectively, ρ_f and $\boldsymbol{J}_f$ the free-charge and free-current density respectively, σ the conductivity, ϵ_0 and μ_0 are the vacuum and vacuum permeability, respectively.

[13] Here the terms population and occupation probability are used interchangeably to refer to diagonal values of the density matrix, i.e probability to be in a specific state. The total number of nuclei in a given state is obtained by integrating the diagonal elements of the density matrix over the sample.

[14] Naming conversions vary among textbooks, $\boldsymbol{D}$ may be referred to at the electric displacement field and $\boldsymbol{H}$ the magnetic field strength.

[15] Not to be confused with the polarization of the field.

Here we are interested in nuclear excitation. As such the total current density is $\boldsymbol{J} = \boldsymbol{J}_f + \partial\boldsymbol{P}/\partial t + \nabla \times \boldsymbol{M}$, resulting from a sum of the free currents $\boldsymbol{J}_f$ and bound currents $\boldsymbol{J}_P = \partial\boldsymbol{P}/\partial t$ and $\boldsymbol{J}_M = \nabla \times \boldsymbol{M}$ resulting from the macroscopic polarization and magnetization of the sample, respectively. The total charge density[16] $\rho = \rho_f + \rho_b$ is thus related to the nuclei not the electrons of the system. In such a nuclear system there is no analog to the free charge or free current density (i.e., $\rho_f = \boldsymbol{J}_f = 0$). Here, the impinging field affects local nuclei causing excitation which in the case of electric dipole transitions (E1) can be considered as a macroscopic polarization. In the case of E1 transitions we let $\boldsymbol{M} = 0$ and develop the wave equation as follows,

$$\begin{aligned} \boldsymbol{\nabla} \times (\boldsymbol{\nabla} \times \boldsymbol{E}) &= -\frac{\partial}{\partial t}\boldsymbol{\nabla} \times \boldsymbol{B} && (1.50)\\ &= -\mu_0 \frac{\partial}{\partial t}\left(\frac{\partial \boldsymbol{D}}{\partial t}\right) && (1.51)\\ &= -\mu_0\epsilon_0 \frac{\partial^2 \boldsymbol{E}}{\partial t^2} - \mu_0 \frac{\partial^2 \boldsymbol{P}}{\partial t^2}. && (1.52)\\ & && (1.53) \end{aligned}$$

With $\mu_0\epsilon_0 = 1/c^2$ and using the identity $\boldsymbol{\nabla}(\boldsymbol{\nabla} \cdot \boldsymbol{A}) - \nabla^2 \boldsymbol{A} = \boldsymbol{\nabla} \times (\boldsymbol{\nabla} \times \boldsymbol{A})$ we obtain the wave equation,

$$\nabla^2 \boldsymbol{E} - \boldsymbol{\nabla}(\boldsymbol{\nabla} \cdot \boldsymbol{E}) - \frac{1}{c^2}\frac{\partial^2 \boldsymbol{E}}{\partial t^2} = \mu_0 \frac{\partial^2 \boldsymbol{P}}{\partial t^2}. \quad (1.54)$$

Assuming a plane wave traveling along the z-direction with unit polarization vector $\hat{\boldsymbol{e}} = \boldsymbol{e}/|\boldsymbol{e}|$ we have an electric field[17] in complex form

$$\boldsymbol{E}(z,t) = \mathscr{E}(z,t)e^{i(kz-\omega t)}\hat{\boldsymbol{e}}, \quad (1.55)$$

and then must have a macroscopic polarization of the form

$$\boldsymbol{P}(z,t) = \mathscr{P}(z,t)e^{i(kz-\omega t)}\hat{\boldsymbol{e}}. \quad (1.56)$$

The electric field oscillates perpendicular to the direction of travel, therefore $\boldsymbol{\nabla} \cdot \boldsymbol{E} = 0$ holds regardless of the electric field polarization vector $\hat{\boldsymbol{e}}$. As a result,

$$\begin{aligned} \nabla^2 \boldsymbol{E} - \frac{1}{c^2}\frac{\partial^2 \boldsymbol{E}}{\partial t^2} &= \mu_0 \frac{\partial^2 \boldsymbol{P}}{\partial t^2}, && (1.57)\\ \left(\frac{\partial}{\partial z} + \frac{1}{c}\frac{\partial}{\partial t}\right)\left(\frac{\partial}{\partial z} - \frac{1}{c}\frac{\partial}{\partial t}\right)\boldsymbol{E} &= \mu_0 \frac{\partial^2 \boldsymbol{P}}{\partial t^2}. && (1.58) \end{aligned}$$

Now making the Slowly Varying Envelope Approximation (SVEA) we enforce [40, 47]

$$\begin{aligned} \partial_t^2 U \ll \omega \partial_t U \ll \omega^2 U && (1.59)\\ \partial_z^2 U \ll k \partial_z U \ll k^2 U && (1.60) \end{aligned}$$

where $U = \mathscr{E}, \mathscr{P}$. We find that

$$\begin{aligned} \left(\frac{\partial}{\partial z} - \frac{1}{c}\frac{\partial}{\partial t}\right)E \approx 2ikE, && (1.61)\\ \frac{\partial^2 P}{\partial t^2} \approx -\omega^2 P, && (1.62) \end{aligned}$$

where we have dropped the polarization vectors as they are the same[18]. This results in,

$$\left(\frac{\partial}{\partial z} + \frac{1}{c}\frac{\partial}{\partial t}\right)E \approx \frac{i\mu_0\omega^2}{2k}P = \frac{i\pi}{\epsilon_0\lambda}P \quad (1.63)$$

where $k = 2\pi/\lambda = \omega/c$ is the wave vector and λ the wavelength of the transition.

Here we will now consider the form of the macroscopic polarization. The expectation value of an operator O is $\langle O \rangle = Tr[O\rho]$ where Tr is the trace and ρ is the density operator [40, p74] [44, p909]. Therefore, considering electric dipole transitions the macroscopic polarization can be

[16] Not to be confused with the occupation probability.
[17] Physical field is found by taking the real part.
[18] $\boldsymbol{E} = E\hat{\boldsymbol{e}}$, $\boldsymbol{P} = P\hat{\boldsymbol{e}}$.

written as $\boldsymbol{P} = N\langle \boldsymbol{d} \rangle$ or $P = N\,\mathrm{Tr}[(\boldsymbol{d}\cdot\hat{\boldsymbol{e}})\rho]$ which for a two-state system is[19] $P = 2N\,(\boldsymbol{d}_{12}\cdot\hat{\boldsymbol{e}})\rho_{21}$, where $\boldsymbol{d}$ is the electric dipole moment, and N the number density of active nuclei in the sample.

The electric dipole interaction potential is given by [45, p202]

$$\hat{V}^{E1} = -\boldsymbol{d}\cdot\boldsymbol{E}(0,t), \tag{1.64}$$

making the Rabi frequency[20] $\Omega^{E1} = (\boldsymbol{d}\cdot\boldsymbol{E})/\hbar$. Substitution results in the final form of the field equation for E1 transitions,

$$\left(\frac{\partial}{\partial z} + \frac{1}{c}\frac{\partial}{\partial t}\right)\Omega_{21} \approx i\frac{2\pi N(\boldsymbol{d}_{21}\cdot\hat{\boldsymbol{e}})^2}{\epsilon_0\lambda\hbar}\rho_{21}. \tag{1.65}$$

Similarly, in the case of magnetic dipole transitions (M1), the interaction potential is [45, p202]

$$\hat{V}^{M1} = -\boldsymbol{m}\cdot\boldsymbol{B}(0,t) \tag{1.66}$$

where the magnetization $\boldsymbol{M} = N\langle\boldsymbol{m}\rangle$ [45, p705]. In such a transition it is the interaction of the magnetic field $\boldsymbol{B}$ with the magnetic moment $\boldsymbol{m}$ that is important. Developing the wave equation for the magnetic field where $\boldsymbol{J}_f = \boldsymbol{P} = 0$, $\boldsymbol{B}(z,t) = \mathscr{B}(z,t)e^{i(kz-\omega t)}\hat{\boldsymbol{b}}$, and $\boldsymbol{M}(z,t) = \mathscr{M}(z,t)e^{i(kz-\omega t)}\hat{\boldsymbol{b}}$, where $\hat{\boldsymbol{b}} = \boldsymbol{b}/|\boldsymbol{b}|$ is the unit polarization vector of the magnetic field, results in

$$\nabla^2\boldsymbol{B} - \frac{1}{c^2}\frac{\partial^2\boldsymbol{B}}{\partial t^2} = -\mu_0\nabla\times\boldsymbol{J} \tag{1.67}$$

which after making the SVEA results in

$$\left(\frac{\partial}{\partial z} + \frac{1}{c}\frac{\partial}{\partial t}\right)\boldsymbol{B} \approx \frac{i\mu_0 k}{2}\boldsymbol{M}. \tag{1.68}$$

Making the substitution for Rabi frequency $\Omega^{M1} = (\boldsymbol{m}\cdot\boldsymbol{B})/\hbar$ results in the final form of the field equation for M1 transitions,

$$\left(\frac{\partial}{\partial z} + \frac{1}{c}\frac{\partial}{\partial t}\right)\Omega_{21} \approx \frac{i\mu_0 k N(\boldsymbol{m}_{21}\cdot\hat{\boldsymbol{b}})^2}{\hbar}\rho_{21}. \tag{1.69}$$

In both cases we can define the resonant cross section, as shown in Section 1.2.1 to be,

$$\sigma^{E1} = \frac{4\pi(\boldsymbol{d}\cdot\hat{\boldsymbol{e}})^2}{\epsilon_0\lambda\hbar\Gamma}, \tag{1.70}$$

$$\sigma^{M1} = \frac{2\mu_0 k(\boldsymbol{m}\cdot\hat{\boldsymbol{b}})^2}{\hbar\Gamma}, \tag{1.71}$$

which allows us to write field equation for both E1 and M1 in the same final form,

$$\left(\frac{\partial}{\partial z} + \frac{1}{c}\frac{\partial}{\partial t}\right)\Omega_{21} = i\frac{N\sigma\Gamma}{2}\rho_{21} = i\eta\rho_{21} \tag{1.72}$$

where $\eta = N\sigma\Gamma/2$. In the literature, for example in [54, 55], it is common to reference to the effective resonant thickness as $\xi = N\sigma L/4$, where L is the thickness of the sample along the optical axis, hence we may also write $\eta = 2\xi\Gamma/L$.

In the following sections we will generalize the field equation to allow us to study systems with an arbitrary number of levels.

1.2.1 Resonant cross section

In order to write the final field equation (1.72) we had to make the connection between (1.65) and (1.69). To do so we defined the transition's resonant cross section. Both E1 and M1 transitions have different cross sections, however they both refer to the same quantity, namely the ratio of scattered power to incident energy flux resulting in units of area. The proof of the resonant cross section is as follows.

[19] $\Re\{z\} = (z+z^*)/2$, hence $d_{12}\rho_{21} + d_{21}\rho_{12} = 2d_{12}\rho_{21}$.

[20] See (1.26). Here the time averaging is left out to avoid cluttered notation.

Starting from the Bloch equations for a two-state system where $\rho_{11} + \rho_{22} = 1$,

$$\begin{aligned}
\dot{\rho}_{11} &= -\frac{i}{2}(\Omega\tilde{\rho}_{12} - \Omega^*\tilde{\rho}_{21}) + \Gamma\rho_{22}, \\
\dot{\tilde{\rho}}_{21} &= \frac{i}{2}\Omega(\rho_{11} - \rho_{22}) - \left(i\Delta + \frac{1}{2}\Gamma\right)\tilde{\rho}_{21}, \\
\dot{\rho}_{22} &= \frac{i}{2}(\Omega\tilde{\rho}_{12} - \Omega^*\tilde{\rho}_{21}) - \Gamma\rho_{22},
\end{aligned}$$

we find the steady state solution. This is found in the limit as time goes to infinity or equivalently as the rate of change of population goes to zero [56, p.194][57, p.72 & 345][44, p.779, p.892]

$$\begin{aligned}
\rho_{22} &= \frac{i}{2\Gamma}(\Omega\tilde{\rho}_{12} - \Omega^*\tilde{\rho}_{21}) \\
\tilde{\rho}_{21} &= \frac{i\Omega(1 - 2\rho_{22})}{2i\Delta + \Gamma}.
\end{aligned}$$

Solving for ρ_{22} we find,

$$\rho_{22} = \frac{(\Omega/\Gamma)^2}{1 + 4(\Delta/\Gamma)^2 + 2(\Omega/\Gamma)^2}. \tag{1.73}$$

The rate of production of scattered photons by a single two-level atom is then [56, 58]

$$R = \Gamma\rho_{22} \tag{1.74}$$

$$= \frac{\Gamma}{2}\frac{I/I_0}{1 + 4(\Delta/\Gamma)^2 + I/I_0}, \tag{1.75}$$

where we have introduced the intensity, I, and saturation intensity, I_0. Using $I = c\varepsilon_0\mathscr{E}^2/2$ and $\Omega^{E1} = (\boldsymbol{d}\cdot\hat{\boldsymbol{e}})\mathscr{E}/\hbar$,

$$\frac{I}{I_0} = 2\left(\frac{\Omega}{\Gamma}\right)^2, \tag{1.76}$$

$$I_0 = \frac{c\varepsilon_0\Gamma^2\hbar^2}{4(\boldsymbol{d}\cdot\hat{\boldsymbol{e}})^2}. \tag{1.77}$$

Finally we can define the scattering cross section as the power radiated divided by the incident energy flux, $\sigma = R\hbar\omega/I$ [45, p.286 & 462] we have

$$\sigma = \frac{\sigma_0}{1 + 4(\Delta/\Gamma)^2 + I/I_0}, \tag{1.78}$$

where the resonant cross section is,

$$\begin{aligned}
\sigma_0 &= \frac{\hbar\omega\Gamma}{2I_0}, \\
\sigma_0^{E1} &= \frac{4\pi(\boldsymbol{d}\cdot\hat{\boldsymbol{e}})^2}{\epsilon_0\lambda\hbar\Gamma}.
\end{aligned} \tag{1.79}$$

In the case of magnetic dipole transitions we first solve for the laser intensity in terms of the magnetic field amplitude. Electric and magnetic components of the electromagnetic field are always perpendicular to each other and the direction of travel[21],

$$\begin{gathered}
\boldsymbol{E} = \mathscr{E}e^{i(kz-\omega t)}\hat{\boldsymbol{e}}, \\
\boldsymbol{B} = \mathscr{B}e^{i(kz-\omega t)}\hat{\boldsymbol{b}}, \\
\boldsymbol{\nabla}\times\boldsymbol{E} = -\frac{\partial\boldsymbol{B}}{\partial t}, \\
\partial_z E = -\partial_t B, \\
ikE = -i\omega B, \\
\mathscr{E}/c = \mathscr{B}.
\end{gathered}$$

Finally we have, $I = c^3\varepsilon_0\mathscr{B}^2/2$. Using then $\Omega^{M1} = (\boldsymbol{m}\cdot\hat{\boldsymbol{b}})\mathscr{B}/\hbar$ and following the same steps as above, we find

$$\sigma_0^{M1} = \frac{2\mu_0 k(\boldsymbol{m}\cdot\hat{\boldsymbol{b}})^2}{\hbar\Gamma}. \tag{1.80}$$

[21] For example $\hat{\boldsymbol{e}} = \hat{\boldsymbol{x}}$ and $\hat{\boldsymbol{b}} = \hat{\boldsymbol{y}}$ for linear polarization.

1.2.2 Initial conditions: Rabi Frequency

In order to understand any physical system we must know the equations governing it as well as the initial conditions. The sections up until now have discussed formulation of the MBE. Here we will discuss the initial conditions required to solve your system of choice.

We must first define the initial state of our system. This refers to the initial occupation probabilities of the levels in the system. Here it is assumed that before laser interaction all systems exist in their respective ground states, i.e., all level populations are zero except ground which is unity, $\rho_{ij}(z,0) = \delta_{ig}\delta_{jg}$. This approximation is made assuming our system is cooled such that the thermal energy is less than the spacing between low lying levels. This will be further discussed in later sections.

Secondly, we must define the initial state of the laser pulse. This is done by defining the initial form of the Rabi frequency Ω. Recall from (1.76) that the Rabi frequency is proportional to the exciting laser field amplitude. As such we define the shape of the laser pulse by defining an initial form of the Rabi frequency. For $\Omega(z,t) = const.$ we have continuous wave excitation. For pulsed excitation we have to define a pulse shape such as Gaussian, $\Omega(0,t) = \Omega_0 e^{-((t-t_p)/T)^2}$, where Ω_0 is the peak frequency, t_p the pulse delay time and T controls the pulse width.

To calculate the peak frequency we start from equation (1.76) which describes the Rabi frequency for the continuous driving of a two-level system,

$$\Omega \quad = \quad \sqrt{\frac{\Gamma I}{\hbar\omega}\sigma_0}.$$

Here we are concerned with transitions between two nuclear levels with angular momentum $I_g = 5/2$ and $I_e = 3/2$ for the ground and excited states respectively. These states can be split into $(2I+1)$ sub levels denoted by their angular momentum projection $m_I = \{I, I-1, \ldots, -I\}$. We will be concerned with specific transitions between the ground and excited state sub-levels. Hence we can make a change in notation to $\Gamma \rightarrow \gamma_{m_g,m_e}$, where γ_{m_g,m_e} is a partial decay rate from $|I_e, m_e\rangle \rightarrow |I_g, m_g\rangle$.

The resonant cross section[22]is given by [61, p.593] [48, p.507] [49, p.169] [45, p.180] [59, p.57]

$$\sigma_0 = \frac{\lambda^2}{\pi}(2K+1). \tag{1.82}$$

The partial decay rate being a transition rate can be written via Fermi's golden rule as

$$\gamma_{m_g,m_e} = \frac{2\pi}{\hbar}|\langle I_g m_g|H_{\lambda K,q}|I_e m_e\rangle|^2, \tag{1.83}$$

where $H_{\lambda K,q}$ is the interaction Hamiltonian expressed in the spherical basis and $\lambda = (E,M)$ refers to the interaction type[23] electric or magnetic, K is the transition multipolarity and q the spherical component which can take values $\{K, K-1, \ldots, -K\}$. The total decay rate from state $|I_e\rangle \rightarrow |I_g\rangle$ is [62, p.589],

$$\Gamma = \frac{1}{2I_e+1}\sum_{m_g,m_e,q}\gamma_{m_g,m_e} = \frac{2(K+1)}{\hbar\varepsilon_0 K((2K+1)!!)^2}\left(\frac{E}{\hbar c}\right)^{2K+1}\mathbb{B}_{\downarrow}. \tag{1.84}$$

where $\mathbb{B}_{\downarrow}$ reduced transition probability for the decay $e \rightarrow g$ and E nuclear transition energy. Via the Wigner-Eckhart theorem [63], see Appendix A.2, we can write the matrix element in terms of reduced matrix elements,

$$|\langle I_g m_g|H_{\lambda K,q}|I_e m_e\rangle|^2 = \frac{1}{2K+1}\left(C^{I_g\ \ I_e\ \ K}_{m_g\ -m_e\ q}\right)^2|\langle I_g||H_{\lambda K}||I_e\rangle|^2, \tag{1.85}$$

[22]As discussed in [59, p.57], [60, p.435] and [48, p.613] the Breit-Wigner formula for and unpolarized beam is,

$$\sigma = \frac{\lambda^2(2J+1)}{\pi(2s_a+1)(2s_b+1)}\frac{\Gamma/4}{(E-E_R)^2+\Gamma/4}. \tag{1.81}$$

In our case we consider a polarized excitation of a specific, fixed m sub-level transition, as such the statistical averaging factor $\frac{(2J+1)}{(2s_a+1)(2s_b+1)}$ is not necessary and thus reduces to $(2K+1)$.

[23]Not to be confused with the wavelength.

where $C^{I_g\ I_e\ K}_{m_g-m_e\ q}$ are Clebsch-Gordan coefficients[24]. Summing over sub-levels and spherical basis components allows us to write the total rate Γ for a given multipolarity K in terms of the reduced matrix element

$$\frac{1}{2I_e+1}\sum_{m_e,m_g,q}|\langle I_g m_g|H_{\lambda K,q}|I_e m_e\rangle|^2 = \frac{1}{2K+1}\frac{|\langle I_g||H_{\lambda K}||I_e\rangle|^2}{2I_e+1}\sum_{m_e,m_g,q}\left(C^{I_g\ I_e\ K}_{m_g-m_e\ q}\right)^2, \quad (1.87)$$

$$= \frac{|\langle I_g||H_{\lambda K}||I_e\rangle|^2}{2I_e+1} = \frac{\Gamma}{2\pi/\hbar}. \quad (1.88)$$

This then allows us to write the partial decay rate in terms of reduced transition probabilities $\mathbb{B}$ which we know from literature [3],

$$\gamma_{m_g,m_e} = \frac{2I_e+1}{2K+1}\left(C^{I_g\ I_e\ K}_{m_g-m_e\ q}\right)^2\Gamma. \quad (1.89)$$

Finally, for the Rabi frequency[25]

$$\Omega = \sqrt{\frac{I}{\hbar\omega}\frac{\lambda^2}{\pi}(2I_e+1)\left(C^{I_g\ I_e\ K}_{m_g-m_e\ q}\right)^2\frac{2(K+1)}{\hbar\varepsilon_0 K((2K+1)!!)^2}\left(\frac{E}{\hbar c}\right)^{2K+1}\mathbb{B}_\downarrow} \quad (1.90)$$

$$= \sqrt{\frac{8\pi I}{\hbar^2\varepsilon_0 c}\frac{K+1}{K((2K+1)!!)^2}\left(\frac{E}{\hbar c}\right)^{2K-2}\left(C^{I_g\ I_e\ K}_{m_g-m_e\ q}\right)^2(2I_g+1)\mathbb{B}_\uparrow} \quad (1.91)$$

where the wavenumber $2\pi/\lambda = E/(\hbar c)$, and $\mathbb{B}_\uparrow = \frac{2I_e+1}{2I_g+1}\mathbb{B}_\downarrow$.

Finally the initial condition of the field is the shape of the pulse with peak amplitude given by Ω_0 shown in (1.91), where we know the nuclear reduced transition probabilities from literature and we choose the desired laser intensity I.

1.2.3 Factoring of Clebsch-Gordan coefficients

As seen in equation (1.91), the Rabi frequency for the excitation between specific sub-levels is proportional to the corresponding Clebsch-Gordan coefficient for the decay process, $C^{I_g\ I_e\ K}_{m_g-m_e\ q}$. Often we will consider an applied field that drives more than one transition. In this case we must factor the Clebsch-Gordan coefficients out of the Rabi frequency. Considering the M1 transition we start with the field equation (1.68),

$$\left(\frac{\partial}{\partial z}+\frac{1}{c}\frac{\partial}{\partial t}\right)\boldsymbol{B} \approx \frac{i\mu_0 k}{2}\boldsymbol{M},$$

which is equivalent to,

$$\left(\frac{\partial}{\partial z}+\frac{1}{c}\frac{\partial}{\partial t}\right)\frac{\Omega}{\boldsymbol{m}\cdot\hat{\boldsymbol{b}}} = \frac{i\mu_0 k}{2\hbar}N\,\mathrm{Tr}[(\boldsymbol{m}\cdot\hat{\boldsymbol{b}})\rho], \quad (1.92)$$

where $\Omega = (\boldsymbol{m}\cdot\hat{\boldsymbol{b}})\mathscr{B}/\hbar$, and $M = N\,\mathrm{Tr}[(\boldsymbol{m}\cdot\hat{\boldsymbol{b}})\rho]$. Looking closer at the trace we can define $\boldsymbol{m}_{ij} = |C_{ji}|\,\boldsymbol{m}$ resulting in,

$$\mathrm{Tr}[(\boldsymbol{m}\cdot\hat{\boldsymbol{b}})\rho] = \mathrm{Tr}\left[\begin{pmatrix}\boldsymbol{m}_{11}\cdot\hat{\boldsymbol{b}} & \boldsymbol{m}_{12}\cdot\hat{\boldsymbol{b}} & \dots\\ \boldsymbol{m}_{21}\cdot\hat{\boldsymbol{b}} & \boldsymbol{m}_{22}\cdot\hat{\boldsymbol{b}} & \dots\\ \vdots & \vdots & \ddots\end{pmatrix}\begin{pmatrix}\rho_{11} & \rho_{12} & \dots\\ \rho_{21} & \rho_{22} & \dots\\ \vdots & \vdots & \ddots\end{pmatrix}\right] \quad (1.93)$$

$$= (\boldsymbol{m}\cdot\hat{\boldsymbol{b}})\sum_{ij}|C_{ij}|\rho_{ij} = 2(\boldsymbol{m}\cdot\hat{\boldsymbol{b}})\sum_{\substack{i,j,\\ j<i}}|C_{ij}|\rho_{ij} \quad (1.94)$$

[24]Several notations are used here, such as,

$$C_{fi} = C_{I_g m_g, I_e m_e} = C^{I_g\ I_e\ K}_{m_g-m_e\ q}. \quad (1.86)$$

This is done to avoid cluttered notation, however the first two are somewhat ambiguous and thus the last one is used when the notation is not as easily understood.

[25]For consistency with published values note that $|C_{ij}| = |C_{ji}|$ or with complete notation,

$$\left(C^{I_e\ I_g\ K}_{m_e-m_g-q}\right)^2 = \frac{1}{2K+1}\begin{pmatrix}I_e & I_g & K\\ m_e & -m_g & q\end{pmatrix}^2 = \frac{1}{2K+1}\begin{pmatrix}I_g & I_e & K\\ m_g & -m_e & -q\end{pmatrix}^2 = \left(C^{I_g\ I_e\ K}_{m_g-m_e\ q}\right)^2$$

where C_{ij} are Clebsch-Gordan coefficients. The only elements of $(\boldsymbol{m}\cdot\hat{\boldsymbol{b}})$ that survive are the transitions that can be driven with polarization $\hat{\boldsymbol{b}}$. Here, we set all diagonal terms $\boldsymbol{m}_{ii}$ to zero. Strictly speaking the diagonal terms are non-zero. They represent the static magnetic moments which are not of interest here as they do not correspond to a nuclear transition[26]. As a result we have,

$$\left(\frac{\partial}{\partial z}+\frac{1}{c}\frac{\partial}{\partial t}\right)\Omega=\frac{i\mu_0 kN(\boldsymbol{m}\cdot\hat{\boldsymbol{b}})^2}{\hbar}\sum_{\substack{i,j,\\ j<i}}|C_{ij}|\rho_{ij}=i\eta\sum_{\substack{i,j,\\ j<i}}|C_{ij}|\rho_{ij},$$

where $\Omega_{ij}=|C_{ji}|\Omega$.

1.3 Nuclear forward scattering and the Maxwell-Bloch Equations

The complete set of MBE and initial conditions for single pulsed excitation can then be written as,

$$\partial_t\hat{\rho}=\frac{1}{i\hbar}[\hat{H},\hat{\rho}]+\hat{\rho}_r, \tag{1.95}$$

$$\left(\frac{\partial}{\partial z}+\frac{1}{c}\frac{\partial}{\partial t}\right)\Omega=i\eta\sum_{\substack{i,f,\\ f<i}}|C_{fi}|\rho_{fi}, \tag{1.96}$$

$$\rho_{ij}(z,0)=\delta_{ig}\delta_{jg}, \tag{1.97}$$

$$\Omega(z,0)=\Omega_0 e^{-((t_p)/T)^2}, \tag{1.98}$$

$$\Omega(0,t)=\Omega_0 e^{-((t-t_p)/T)^2}, \tag{1.99}$$

$$\Omega_0=\sqrt{\frac{8\pi I_0}{\hbar^2\varepsilon_0 c}\frac{K+1}{K((2K+1)!!)^2}\left(\frac{E}{\hbar c}\right)^{2K-2}\left(C^{\,I_g\ \ I_e\ \ K}_{m_g\,-m_e\,q}\right)^2(2I_e+1)\mathbb{B}_{\downarrow}} \tag{1.100}$$

where the field Ω drives all transitions $i\rightarrow f$ with individual Rabi frequency $\Omega_{fi}=|C_{if}|\Omega=|C_{fi}|\Omega$. At this point it should be clear that the Rabi frequency is not only the oscillation frequency of the population at zero detuning and decay, but from its definition is proportional to $\sqrt{I}$ and thus the amplitude of the exciting field for electric and magnetic dipole transitions. We can therefore loosely refer to it as an amplitude. As such, by solving the MBE self consistently we can plot the relative intensity of the scattering signal $I/I_0\propto|\Omega/\Omega_0|^2$, where I_0 is the peak intensity of the exciting field. This approach can also be generalized by allowing for multiple lasers to excite our sample. This involves then multiple field equations each with their own initial conditions.

[26] When considering direct nuclear excitation with photons there cannot be a transition between a state and itself due to energy conservation. Disregarding energy conservation, the terms $(\boldsymbol{m}\cdot\hat{\boldsymbol{b}})C_{ii}\rho_{ii}$ satisfy the selection rules for a $\Delta m=0$ type M1 transition but would require zero energy photons and are thus neglected. In the case of EB, presented in Part II, this is different as energy must be conserved as a whole between nucleus and electron shell, as such there can be contributions from transitions where the initial, intermediate and final states can be the same.

Chapter 2

NFS in ^{229}Th:CaF$_2$

The complete outline of the MBE in the previous chapter now allows us to consider our specific system of thorium-doped calcium fluoride ^{229}Th:CaF$_2$. The host crystal CaF$_2$ has an experimentally measured band gap of $11-12$ eV [64–66], rendering it transparent in the energy range of the ^{229m}Th nuclear transition. This property allow us to use CaF$_2$ as an inert host for the thorium nuclei which can be doped at high densities upwards of 10^{16} cm^{-3} [7, 10].

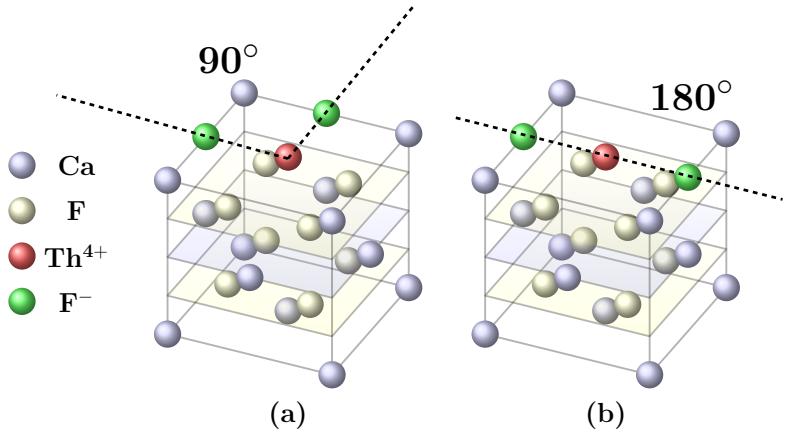

Figure 2.1: Th:CaF$_2$ structure, dopant orientation with (a) 90° and (b) 180° fluoride interstitials.

The CaF$_2$ crystal displays a cubic lattice structure. Thorium-doped in the CaF$_2$ crystal has charge state 4+ and replaces one of the calcium ions introducing two more interstitial fluorine ions for charge compensation. A density-functional study [8] shows that there exists preferred doping configurations, among which the two with lowest energy are the cases when the two fluorine interstitial ions are in a 90° and a 180° configuration relative to the thorium nucleus, as illustrated in Figure 2.1.

As a result of the CaF$_2$ crystal environment, the doped ^{229}Th nuclei experience quadrupole level splitting [7, 8, 67] according to the Hamiltonian

$$\hat{H}_{E2} = \frac{eQV_{zz}}{4I(2I-1)}\left[3\hat{I}_z^2 - \hat{I} + \frac{\eta}{2}\left(\hat{I}_+^2 + \hat{I}_-^2\right)\right], \tag{2.1}$$

where e is the electric charge, $Q_g = 3.11\,\mathrm{b}$ [5, 68] and $Q_e = 1.8\,\mathrm{b}$ [67, 69] are the quadrupole moments of the ground and isomer state, respectively, where $\mathrm{b} = 10^{-24}$ cm^2, V_{zz} is the dominant component of the electric field gradient at the thorium nuclei, $I_g = 5/2$ and $I_e = 3/2$ are the nuclear spin angular momenta of the ground or isomer state, respectively, and $I_z = m$ its projection on the quantization axis (q-axis). Furthermore, $\hat{I}$ and $\hat{I}_z$ are the angular momentum and projection operators with raising and lowering operators $\hat{I}_+$ and $\hat{I}_-$, respectively. Finally, $\eta = (V_{xx} - V_{yy})/V_{zz}$ is the asymmetry parameter of the electric-field gradient[27].

In the case of the two dopant orientations shown in Figure 2.1, we can diagonalize the Hamiltonian (2.1) to find the energy eigenvalues and eigenvectors. These energy levels are shown in Figure 2.2 (not to scale) resulting from the values of $V_{zz} = (223, -296.7)$ VÅ^{-2} and $\eta = (0.48, 0)$ for the 90° and 180° orientations, respectively [8].

[27] Not to be confused with η of the Maxwell-Bloch field equation introduced earlier.

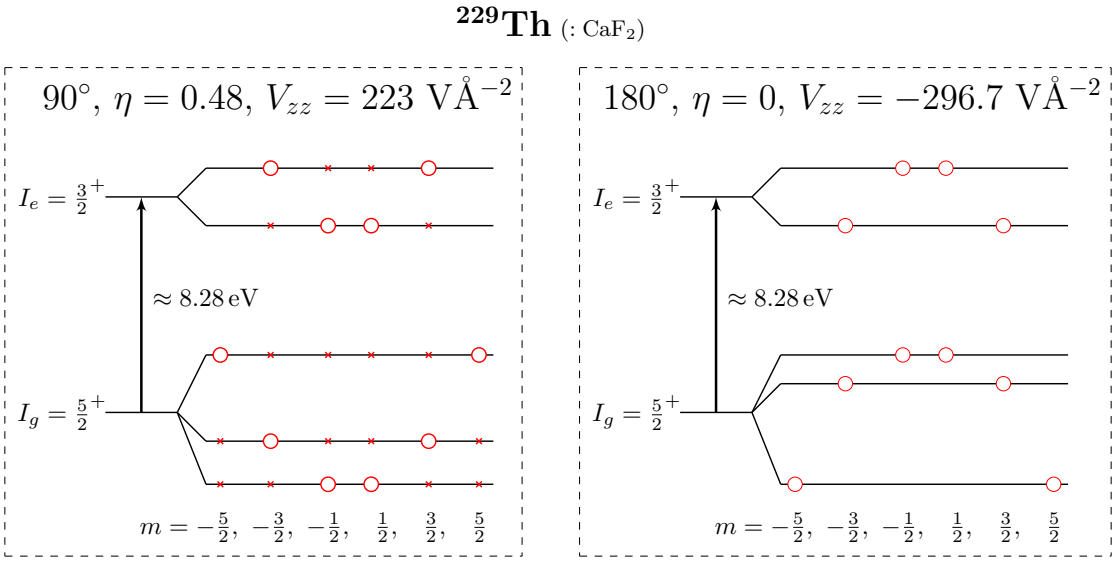

Figure 2.2: ^{229}Th:CaF_2 nuclear quadrupole splitting level scheme (not to scale) for the 90° and 180° fluoride interstitials doping configurations respectively. Open circles define the eigenstates of I_z. In the case of nonzero asymmetry parameter η, the angular momentum projection m is no longer a good quantum number. In this case, open circles define the largest contribution to the eigenstate, where a mixture from states with crosses can be present.

Certain simplifications can be made when considering driving by a narrowband VUV laser. Detailed explanation of these assumptions will be saved for Chapter 3 in order to provide an overview of how the system works before considering its intricacies. To this end, we present in the following a number of assumptions concerning the sample and field in order to demonstrate their consequences on the scattering spectra.

1. To simplify the initial discussion we consider the second most likely case of 180° fluoride interstitials where $\eta = 0$ (no state mixing) and $V_{zz} = -296.7$ VÅ^{-2}. As discussed in Chapter 3, the state mixing can safely be neglected also for the lowest energy case with 90° fluoride interstitials and $\eta = 0.48$, as such all methods outlined here will still apply.

2. We consider the case of coherent driving with a narrowband laser. When driving transitions near resonance, our calculations in Chapter 3 show that one can reduce the ^{229}Th:CaF_2 10-level scheme to a simpler effective system with uniform quantization axis. This is justified because the detuning in energy to the transition of interest $E_{\Delta i} = \hbar\Delta_i$ is less than the energy width of the excitation pulse $E_p = \hbar/T$, where E_p is less than the quadrupole level splitting E_Q and does not overlap with multiple hyperfine levels, $E_{\Delta i} < E_p < E_Q$. In such a case many levels can be neglected in systems with mismatched q-axes, because even though selection rules are satisfied, they are far out of resonance in comparison to the transitions of interest. In this limit, plots of relative intensity will show correct functional behaviour but will have to be scaled by factors relating the fraction of population taking part in the transitions.

3. We assume that crystal cooling will reduce the ground-state population to only the lowest hyperfine sub-levels. This is not a necessary condition, as its only purpose is to prevent relaxation between ground states. Even if this condition is not met the results will be similar in function but with lower intensity due to less population taking part.

For the 180° fluoride interstitials doping orientation, the hyperfine-split nuclear level scheme is illustrated in Figure 2.3. Considering the positive parity of both the ground and isomeric states, $(I_g, I_e) = \left(\frac{5}{2}^+, \frac{3}{2}^+\right)$, selection rules require that the nuclear transition is of magnetic dipole (M1) character. Weak multipole mixing of an electric quadrupole (E2) channel is possible which can be safely disregarded when considering the radiative excitation or decay of the nucleus [36]. The hyperfine splitting that occurs allows for several excitation schemes to be investigated such as a two-level system driven by one VUV laser field and a three-level system driven by two VUV laser fields illustrated in Figure 2.3, addressed previously in [26]. Each scheme has its own benefits. Our goal is to identify an NFS spectrum that has a defined signature of the nuclear excitation, from which we can gain information about the isomeric state. The signature that we aim to create

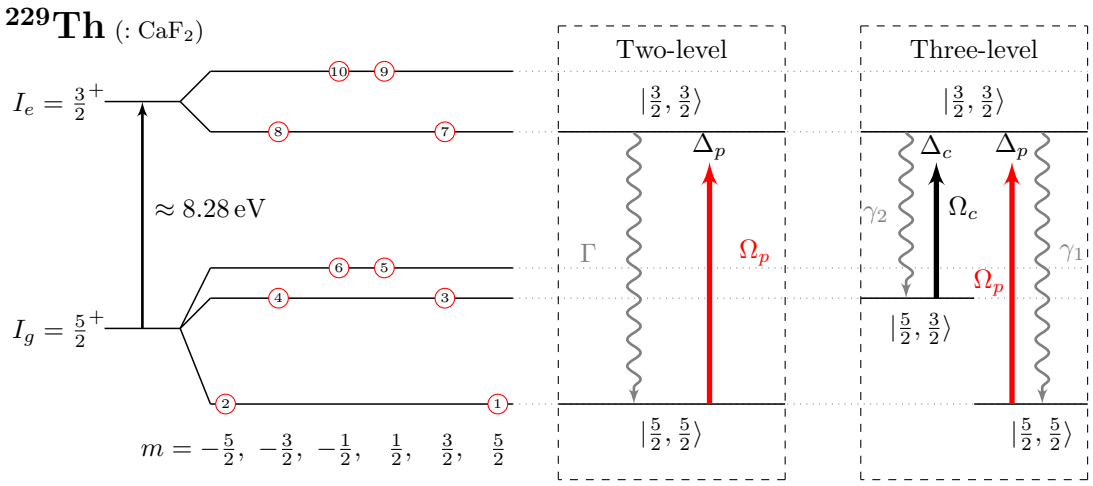

Figure 2.3: ^{229}Th:CaF_2 nuclear quadrupole splitting level scheme (not to scale) for the 180° fluoride interstitials doping configuration. Both ground state and isomeric state have positive parity. The possible projections of the nuclear spin angular momentum on the quantization axis are denoted by m. All states are labeled numerically from $1 \to 10$. Assuming that only the two lower ground state hyperfine levels are populated, probe (Ω_p) and couple (Ω_c) VUV laser pulses can couple to a two- and three-level schemes depicted in the panels on the right-hand side. $\Delta_{p/c}$ stands for the corresponding detunings of the probe and couple laser pulses.

is that of quantum beats induced by interference. This is typically induced by considering an effective V-type system. Here we consider two ways of constructing an effective V-type system: first, using two lasers to create Autler-Townes splitting of the excited state and second, by exciting two crystals successively using the same laser pulse where one of the two crystals is in a static magnetic field. Beyond this, we study for the first time in ^{229}Th:CaF_2 the effect of pulse shape as well as excitation with a pulse train of varying pulse spacing and detunings on the generated NFS signatures. All of these options will be discussed in the following pages.

Concentrating on the $|\frac{5}{2}, \frac{5}{2}\rangle$ level as the initial state we construct the two- and three-level systems by choosing the appropriate driving lasers' orientation and polarization. Being an M1 transition we will refer to the polarization vector of the magnetic component of the exciting laser. First, a left-handed circularly polarized probe pulse Ω_p moving parallel to the quantization axis can be used to excite the isomeric $\Delta m = -1$ transition, $|\frac{5}{2}, \frac{5}{2}\rangle \leftrightarrow |\frac{3}{2}, \frac{3}{2}\rangle$. Secondly, for the three-level system, a linearly polarized continuous-wave (cw) couple laser Ω_c polarized parallel to the quantization axis and moving perpendicular to it drives the $\Delta m = 0$ transition, $|\frac{5}{2}, \frac{3}{2}\rangle \leftrightarrow |\frac{3}{2}, \frac{3}{2}\rangle$. Following the development of the MBE presented in the last chapter, we can write out the set of equations that will be used to solve the above outlined two- and three-level schemes.

The nuclear wave function of the three-level system in question can be written as $|\psi\rangle = A_1(t)|\frac{5}{2}, \frac{5}{2}\rangle + A_2(t)|\frac{5}{2}, \frac{3}{2}\rangle + A_3(t)|\frac{3}{2}, \frac{3}{2}\rangle$ where we can change notation to the following $|\frac{5}{2}, \frac{5}{2}\rangle = |1\rangle$, $|\frac{5}{2}, \frac{3}{2}\rangle = |2\rangle$, and $|\frac{3}{2}, \frac{3}{2}\rangle = |3\rangle$. The Hamiltonian of the three-level system with two fields driving the $1 \to 3$ and $2 \to 3$ transitions is easily written as,

$$\hat{H} = \begin{pmatrix} 0 & 0 & V_{13} \\ 0 & \hbar\omega_2 & V_{23} \\ V_{31} & V_{32} & \hbar\omega_3 \end{pmatrix} \tag{2.2}$$

where ω_n is the frequency of level n and V_{ij} is the field component acting on the $j \to i$ transition. If we set $V_{32} = 0$ this is identical to the two-level system.

The quantization axis is assumed fixed in a known orientation, $\hat{\boldsymbol{q}} = \hat{\boldsymbol{y}}$. We know from earlier that for M1 transitions the perturbing Hamiltonian is,

$$\hat{V} = -\hat{\boldsymbol{m}} \cdot \boldsymbol{B}(0, t), \tag{2.3}$$

where $\hat{\boldsymbol{m}}$ is the transition magnetic dipole moment and $\boldsymbol{B}$ is the magnetic component of the impinging laser field. Selection rules for the probe-field driving the $1 \to 3$ transition, require a left circular polarization of the the impinging magnetic component of the field, moving in a direction parallel to the quantization axis which can be written as,

$$\boldsymbol{B}_{31}(\boldsymbol{r}, t) = \mathscr{B}_{31} e^{i(ky - \nu_p t)} \hat{\boldsymbol{b}}, \tag{2.4}$$

where $\hat{\boldsymbol{b}} = \frac{1}{\sqrt{2}}(\hat{\boldsymbol{z}} - i\hat{\boldsymbol{x}})$ is the polarization vector, ν_p the probe frequency and $\mathscr{B}_{31}$ amplitude. Selection rules for the couple-field driving the $2 \to 3$ transition require a linearly polarized magnetic component parallel to the quantization axis and moving perpendicular to it giving,

$$\boldsymbol{B}_{32}(\boldsymbol{r}, t) = \mathscr{B}_{32} \cos(kz - \nu_c t)\hat{\boldsymbol{y}}. \tag{2.5}$$

The probe-field which carries the relevant information is typically of lower intensity than the couple-field and thus can be difficult to discern from the large background if recorded simultaneously on the same detector. For this reason one needs to find a way to suppress the couple-field at the detector by any means, such as with shutters and polarizers. The selection rules for M1 transition help us not only in simplifying the level scheme as described in earlier sections, but they also help during the measurement as the probe and couple-fields are separated in space. The probe-field is recorded by a detector placed along the y axis, and the couple-field by a detector along z. Because of this, there is no chance for the couple-field to blind the sensitive detector used to measure the probe-field.

With the magnetic fields determined, the potentials take the form

$$V_{31} = -\hbar\Omega_{31} e^{-i\nu_p t}, \tag{2.6}$$

$$V_{32} = -\frac{\hbar}{2}\Omega_{32}\left(e^{i\nu_c t} + e^{-i\nu_c t}\right), \tag{2.7}$$

where $\Omega_{eg} = \langle e|\hat{\boldsymbol{m}}|g\rangle \cdot \boldsymbol{\mathscr{B}}/\hbar$ is the Rabi frequency, $\boldsymbol{\mathscr{B}} = \mathscr{B}\hat{\boldsymbol{b}}$ is the magnetic field amplitude of the impinging laser field including its polarization vector, and where ν_p and ν_c are the frequency of the probe and couple-fields respectively.

Making the unitary transformation,

$$\hat{U} = \begin{pmatrix} 0 & 0 & 0 \\ 0 & e^{-it(\nu_p - \nu_c)} & 0 \\ 0 & 0 & e^{-it\nu_p} \end{pmatrix}, \tag{2.8}$$

gives the transformed density matrix $\hat{\tilde{\rho}} = \hat{U}^\dagger \hat{\rho} \hat{U}$,

$$\hat{\tilde{\rho}} = (\tilde{\rho}_{ij}) = \begin{pmatrix} \rho_{11} & e^{-i(\nu_p - \nu_c)t}\rho_{12} & e^{-i\nu_p t}\rho_{13} \\ e^{i(\nu_p - \nu_c)t}\rho_{21} & \rho_{22} & e^{-i\nu_c t}\rho_{23} \\ e^{i\nu_p t}\rho_{31} & e^{i\nu_c t}\rho_{32} & \rho_{33} \end{pmatrix} \tag{2.9}$$

and the transformed Hamiltonian $\hat{\tilde{H}} = i\hbar\partial_t \hat{U}^\dagger \hat{U} + \hat{U}^\dagger \hat{H} \hat{U}$

$$\hat{H} = \begin{pmatrix} 0 & 0 & e^{-i\nu_p t}V_{13} \\ 0 & \hbar(\omega_2 + \nu_c - \nu_p) & e^{c\nu_p t}V_{23} \\ e^{i\nu_p t}V_{31} & e^{i\nu_c t}V_{32} & \hbar(\omega_3 - \nu_p) \end{pmatrix}. \tag{2.10}$$

Making the Rotating-Wave Approximation (RWA) [40][28], where $\Delta_{p/c}$ are the detunings of the fields to their respective transitions, $\omega_3 = \nu_p + \Delta_p$, $\omega_3 - \omega_2 = \nu_c + \Delta_c$, and factoring out the Clebsch-Gordan from the matrix element $\Omega_{ij} = |C_{ji}|\Omega$ [70], gives the final Hamiltonian of the system

$$\hat{\tilde{H}} \overset{RWA}{\approx} -\hbar \begin{pmatrix} 0 & 0 & |C_{13}|\Omega_p^* \\ 0 & -(\Delta_p - \Delta_c) & |C_{23}|\Omega_c^*/2 \\ |C_{13}|\Omega_p & |C_{23}|\Omega_c/2 & -\Delta_p \end{pmatrix}. \tag{2.11}$$

The relaxation contribution is given by (1.13), where only internal decay from the excited state to ground state, i.e not between the split levels, is allowed. After the unitary transformation we have

$$\hat{\tilde{\rho}}_r = \begin{pmatrix} \gamma_{13}\rho_{33} & 0 & -\frac{\Gamma}{2}\tilde{\rho}_{13} \\ 0 & \gamma_{23}\rho_{33} & -\frac{\Gamma}{2}\tilde{\rho}_{23} \\ -\frac{\Gamma}{2}\tilde{\rho}_{31} & -\frac{\Gamma}{2}\tilde{\rho}_{32} & -\Gamma\rho_{33} \end{pmatrix}. \tag{2.12}$$

Here to correctly describe the relaxation process we introduce terms that only affect the coherences not the populations. Such terms are of the form [40, p163][45, p354] $\rho^c_{nm} = (1 - \delta_{nm})\gamma^c_{nm}\rho_{nm}$, where $\gamma^c_{nm} = \gamma^c_{mn}$ hence,

$$\hat{\tilde{\rho}}_r = \begin{pmatrix} \gamma_{13}\rho_{33} & -\gamma^c_{12}\tilde{\rho}_{12} & -\frac{1}{2}(\Gamma + 2\gamma^c_{13})\tilde{\rho}_{13} \\ -\gamma^c_{12}\tilde{\rho}_{21} & \gamma_{23}\rho_{33} & -\frac{1}{2}(\Gamma + 2\gamma^c_{23})\tilde{\rho}_{23} \\ -\frac{1}{2}(\Gamma + 2\gamma^c_{13})\tilde{\rho}_{31} & -\frac{1}{2}(\Gamma + 2\gamma^c_{23})\tilde{\rho}_{32} & -\Gamma\rho_{33} \end{pmatrix} \tag{2.13}$$

[28] See discussion in [40, p158] where there are no counter rotating terms for left circularly polarized light.

where γ^c are decoherence rates due to spin relaxation in case of 180° doping configuration, $(\gamma^c_{13}, \gamma^c_{23}, \gamma^c_{12}) = 2\pi \times (251, 108, 30)\,\mathrm{Hz}$ [7]. The radiative partial rates γ_{ij} are given by (1.89). Finally, the MBE describing the coherent pulse propagation of the probe, Ω_p, and couple, Ω_c, fields are given by,

$$\partial_t \hat{\tilde{\rho}} = \frac{1}{i\hbar}[\hat{\tilde{H}}, \hat{\tilde{\rho}}] + \hat{\tilde{\rho}}_r, \tag{2.14}$$

$$\frac{1}{c}\partial_t \Omega_p + \partial_z \Omega_p = i\eta\,|C_{13}|\,\rho_{31}, \tag{2.15}$$

$$\frac{1}{c}\partial_t \Omega_c + \partial_z \Omega_c = i\eta\,|C_{23}|\,\rho_{32}. \tag{2.16}$$

Here the field equation for the coupling laser (2.16), is neglected as the high intensity of the coupling field is negligibly affected by the sample. We also assume that no other decay channels are allowed in the crystal environment other than radiative decay; therefore, the radiative decay rate is equal to the total decay rate of the isomeric state $\Gamma_\gamma = \Gamma$.

Equations (2.14) and (2.15) are solved with initial conditions corresponding to a Gaussian input probe pulse and a cw couple laser,

$$\rho_{ij}(z, 0) = \delta_{i1}\delta_{j1}, \tag{2.17}$$

$$\Omega_p(z, 0) = \Omega_{p0} e^{-(t_p/T)^2}, \tag{2.18}$$

$$\Omega_p(0, t) = \Omega_{p0} e^{-((t-t_p)/T)^2}, \tag{2.19}$$

$$\Omega_c(z, t) = \Omega_{c0}, \tag{2.20}$$

where $T = 10\ \mu$s is the pulse half-width and $t_p = 50\ \mu$s the pulse delay time. The peak amplitude is given by (1.91) written here as,

$$\Omega_{p/c0} = \sqrt{\frac{16\pi I}{\hbar^2 \varepsilon_0 c} \frac{(2I_e + 1)}{((3)!!)^2} \mathbb{B}_\downarrow} \tag{2.21}$$

where $\mathbb{B}_\downarrow$ is the reduced transition probability for the nuclear M1 transition which has been evaluated theoretically to $B_W(M1; 3/2^+(7.8\,\mathrm{eV}) \to 5/2^+(0.0\,\mathrm{eV})) \approx 0.7\times10^{-2}$ Weisskopf units, converts via $\mathbb{B}_\downarrow(M1; i \to f) = B_W \times 1.790 \times \mu_N^2$ where $\mu_N = \frac{e\hbar}{2m_p c}$ [3, 71] and m_p is the proton mass. I_0 is the intensity of the exciting lasers, which for the couple was chosen to be 2 kW/cm^2. The normalized NFS intensity, $I = |\Omega_p/\Omega_{p0}|^2$, is independent of the chosen probe intensity I_{p0} provided no Rabi oscillations occur while the pulse is active, hence provided $\Omega_{p0} < \pi/T$. This can be seen clearly in Figure 1.3 and Figure 1.4 where the first maximum population of the excited state is reached at $t = 2\pi/\Omega'$ where $\Omega' = \sqrt{\Omega^2 + \Delta^2}$. Hence, for a pulse half-width of T we require $T < \pi/\sqrt{\Omega_{p0}^2 + \Delta^2}$, or for small detuning $\Delta \ll \Omega_{p0}$, $\Omega_{p0} < \pi/T$ to prevent Rabi oscillations.

The detuning is taken here as $\Delta = \Delta_c = \Delta_p$ [26], and the crystal thickness is taken as $L = 1$ cm. There is a wide range of possible dopant densities in the range of $10^{16} - 10^{18}\,\mathrm{cm}^{-3}$ [7, 10]. Here we choose $N = 10^{16}\,\mathrm{cm}^{-3}$. The radiative lifetime of the isomeric state ^{229m}Th is in the region of several hours, $\tau \approx 6$ h [72], and $\tau \approx 2.5$ h [$\mathbb{B}_\downarrow(M1) \approx 0.007$ Wu. [3]], see Appendices A.3 and A.4. We consider the decay rate as $\Gamma_\gamma = 1/\tau \approx 1 \times 10^{-4}\,\mathrm{s}^{-1}$, which is consistent with recent measurements of the internal conversion rate of ^{229m}Th [17]. The resonant cross section is $\sigma = 3\lambda^2/\pi \approx 2.4 \times 10^{-10}\,\mathrm{cm}^2$, as a result the effective resonant thickness is $\xi \approx 6 \times 10^5$.

The scattered intensity for driving the two-level system is illustrated in Figure 2.4, which shows the exponential decay of the isomeric state. This system is described by the same set of equations presented above where $\Omega_c = 0$. The rate of decay of the NFS spectrum intensity is dependent not only on the radiative decay of the level population but also on the decay of the coherence in the system, see Appendix A.5. As such the exponential decay rate that can be observed in the calculated NFS spectrum is $\Gamma_F = \Gamma_{coh} + \xi\Gamma_\gamma + f(\Delta)$, where $f(\Delta)$ is a function of the laser detuning to the driven transitions where $f(0) = 0$. The NFS intensity for this two-level system displays an exponential decay rate $\Gamma_F = 2\gamma^c_{31} + \Gamma + \xi\Gamma + f(\Delta_p)$ where the largest contribution comes from the decay of the coherence $\Gamma_{coh} = 2\gamma^c_{31} + \Gamma$. Other than the exponential decay of the intensity, this two-level system does not provide any unique features that could help us differentiate it from other decay channels experimentally.

When the strong couple laser is active, both the second and third levels experience Autler-Townes splitting whereby each level splits into two. For a small detuning $\Delta_c \ll \omega_{32}$, the energy separation of the splitting is $\hbar\Omega_{32} = \hbar|C_{23}|\Omega_c$, where each split level is displaced $\pm\hbar\Omega_{32}/2$ around

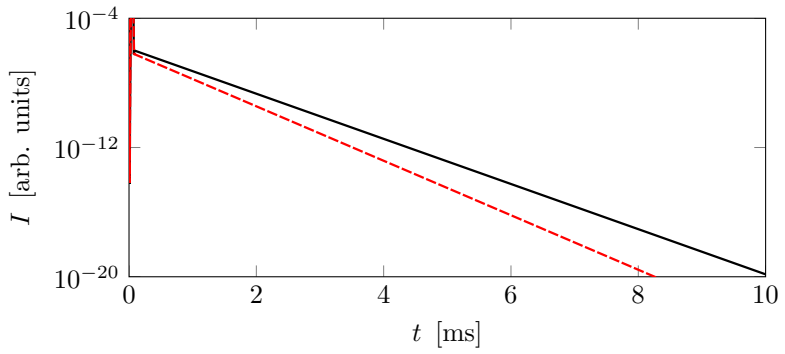

Figure 2.4: Scattered intensity for the case of the two-level system for $\Delta = 0 \sim 10^8\Gamma$ (black solid line) and $\Delta = 10^9\Gamma$ (red dashed line). The excitation occurs for $\Delta < 10^{10}\Gamma \approx \hbar/E_p$.

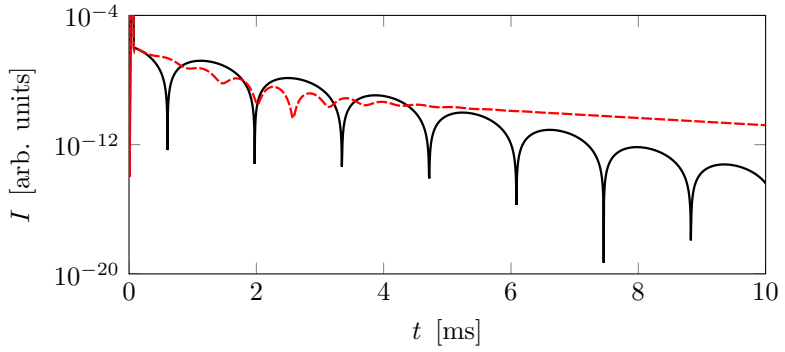

Figure 2.5: Scattered intensity for the case of the three-level system for $\Delta = 0 \sim 10^6\Gamma$ (black solid line) and $\Delta = 10^8\Gamma$ (red dashed line). The excitation occurs for $\Delta < 10^{10}\Gamma \approx \hbar/E_p$.

the unsplit level energy [45, 49]. The quantum beat in the NFS spectrum as a result of the split third state, $|\frac{3}{2}, \frac{3}{2}\rangle$, decaying to the first, $|\frac{5}{2}, \frac{5}{2}\rangle$, is shown in Figure 2.5. The frequency of the quantum beat depends on the difference in energy of the two transitions [73] and hence the energy splitting of the third state. In this case, the frequency of the quantum beat is $f_{QB} = \Omega_{32}/2\pi$ and the minima occur at times $t_n^{min} = (n + \frac{1}{2})/f_{QB} + t_p$, where n is an integer. Hence the larger the splitting, the smaller the time separation between minima. Note that the beat frequency in Figure 2 of [26] is in error by $\sqrt{2I_g + 1} = \sqrt{6}$ due to this missing factor in the initial calculation of Ω_c.

2.1 Modified couple laser Ω_c

The experimental realization of a cw VUV laser is technically difficult. As such, the use of a pulsed coupling laser Ω_c would simplify the experimental implementation of the thorium three-level system shown above. In the following we consider the case of a three-level system driven by pulsed probe and couple lasers for two couple pulse shapes.

2.1.1 Square pulse

Before considering a Gaussian pulse shape we examine the result of abruptly turning the cw laser on and off again after excitation by the probe pulse. For this we modify the initial conditions of the couple to be that of a square pulse

$$\Omega_c(z, 0) = 0 \tag{2.22}$$

$$\Omega_c(0, t) = \begin{cases} \Omega_{c0}, & t_\uparrow < t < t_\downarrow \\ 0, & \text{otherwise} \end{cases} \tag{2.23}$$

where $(t_\uparrow, t_\downarrow)$ are the turn on and off times, respectively. As expected the beating only occurs while the couple laser is on, i.e., while the upper state is split; otherwise the intensity spectrum returns to that of the two-level system. Furthermore, the beating does not restart every time the

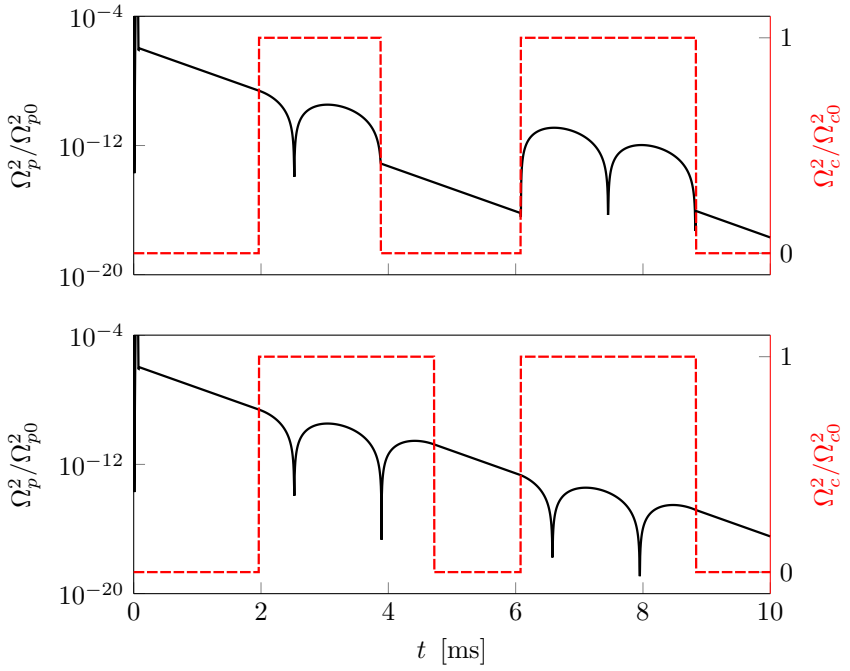

Figure 2.6: NFS intensity of the three-level thorium system resulting from abruptly switching the couple laser on and off (black solid line, left axis) together with the relative intensity of the couple pulse (red dashed line, right axis).

couple is turned off and then on, but rather continues from where it previously ended. Similar to the ideas of storage via magnetic switching [74], if the couple is switched off at a minimum of the quantum beat, the beating can be revived with maximal intensity in the next on cycle as illustrated in Figure 2.6.

If we then consider many on-off cycles where the time spacing between the end of one cycle and the start of the next goes to zero, the NFS spectrum will approach that of a cw laser, i.e., Figure 2.5. As such we can envisage the use of a pulsed couple laser where the pulse spacing is far less than the time scale of the quantum beat, i.e., $\ll 2\pi/\Omega_{32}$.

2.1.2 Gaussian pulse

To convert Ω_c from cw to a Gaussian pulse laser we introduce a Gaussian pulse shape to the initial conditions

$$\Omega_c(z,0) = \Omega_{c0}e^{-(t_c/T_c)^2}, \tag{2.24}$$
$$\Omega_c(0,t) = \Omega_{c0}e^{-((t-t_c)/T_c)^2}, \tag{2.25}$$

where t_c is the delay of the pulse and T_c is the half width of the pulse. Similar to the case of the square pulse, the choice of t_c and T_c determine the time interval over which the quantum beat is visible. Provided there is no time delay between the couple and probe, $t_c = t_p$, and the width of the pulse $T_c \gg 10$ ms, the result is the same as shown in Figure 2.5.

Our numerical results for the Gaussian couple pulse are illustrated in Figure 2.7. Reducing the temporal width of the couple pulse will begin to erase the quantum beat in the region outside T_c. This is because, for a Gaussian pulse, the period of the induced quantum beat

$$T_{QB} = \frac{2\pi}{|C_{23}|\Omega_{c0}e^{-((t-t_c)/T_c)^2}} \tag{2.26}$$

increases gradually as the pulse intensity diminishes. This is in contrast to $T_{QB} \to \infty$ in the case of the square-pulse couple-laser abruptly turning off, $\Omega_{c0} \to 0$.

This can be easily generalized to a pulse train with pulse spacing δ

$$\Omega_c = \Omega_{c0}\sum_{n=1}^{N} e^{-((t-t_c-n\delta)/T_c)^2}. \tag{2.27}$$

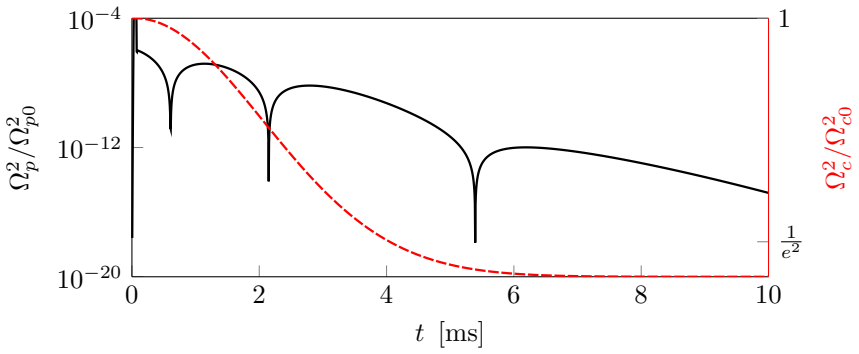

Figure 2.7: NFS scattered intensity for the three-level thorium system with a Gaussian pulse couple laser (black solid line, left axis) together with the couple pulse relative intensity (red dashed line, right axis) for $t_c = t_p = 50$ μs and $T_c = 4$ ms.

When both width and spacing of the Gaussian pulses become small compared to the time scale of the quantum beat at peak intensity, $(T_c, \delta) \ll 2\pi/(|C_{23}|\Omega_{c0})$, the resultant spectrum tends towards that of a cw laser.

2.2 Train of probe pulses

In experiment the intensity of the resonant pulse is usually weak, i.e., much fewer resonant photons per pulse than number of nuclei in the sample. As such, to generate the NFS signal, many pulses are used and the sum of the measured counts and time delays are used to build the final intensity spectrum. A variety of pulse shapes can be constructed from a single mode wave $E(t) = \cos(\nu t + \phi)$ by multiplying with the desired envelope; for simplicity we use a Gaussian $E(t) = e^{-((t-t_0)/T)^2}\cos(\nu t + \phi)$. Here we study the effect of introducing multiple excitation pulses varying both time delay and relative phase.

2.2.1 Two-level system with $\Delta = 0$

First, in order to identify the main features of the problem we consider for simplicity driving the two-level system seen in Figure 2.3 with no laser detuning $\Delta = 0$ such that the exciting field has the same frequency as the transition. For further discussion we consider next to the total scattered intensity also the square of the real $\Re\{\Omega\}^2$ and imaginary $\Im\{\Omega\}^2$ components. In the case of zero detuning $(\Im\{\Omega\})^2 = 0$, and the NFS intensity is $I = |\Omega/\Omega_0|^2 = (\Re\{\Omega\}/\Omega_0)^2$. By changing the initial conditions of the calculation we can add a phase shift to the pulse

$$\Omega(0,t) \quad = \quad \Omega_0 e^{-(t/T)^2} e^{i\phi}, \tag{2.28}$$

which for a single pulse has no effect on the resultant intensity spectrum, proof of this is given in Appendix A.6. When introducing multiple excitation pulses the relative phase becomes important. Figure 2.8 shows the result of considering two pulses with a relative phase shift of $\phi = (0, \pi)$,

$$\Omega(0,t) \quad = \quad \Omega_0 \left(e^{-(t/T)^2} + e^{-((t-t_0)/T)^2} e^{i\phi} \right), \tag{2.29}$$

with a time delay $t_0 = 50$ μs and pulse width $T = 0.1$ μs, where both incoming pulses have the same intensity. The incoming pulses arriving in phase to each other lead to constructive interference and an increased signal, while the pulses arriving in antiphase cancel each other and lead to a decreased signal in comparison with the case of a single incident pulse.

In more detail, this variation in NFS intensity is a manifestation of superposition where the intensity is proportional to the number of excited nuclei. The m^{th} pulse excites $N_m(0)$ nuclei which have the option to decay back to the ground state $N_m(t) = N_m(0)e^{-\Gamma_F t/2}$, but cannot be excited further in the two-level system. Provided there are enough nuclei in the ground state and all weak pulses m have the same resonant intensity, then all $N_m(0)$ are equal. In such a case the total intensity of the emitted decay signal after a train of excitation pulses is

$$I(t) \propto \left| \sum_m N_m(t) e^{i\phi_m} \right|^2 . \tag{2.30}$$

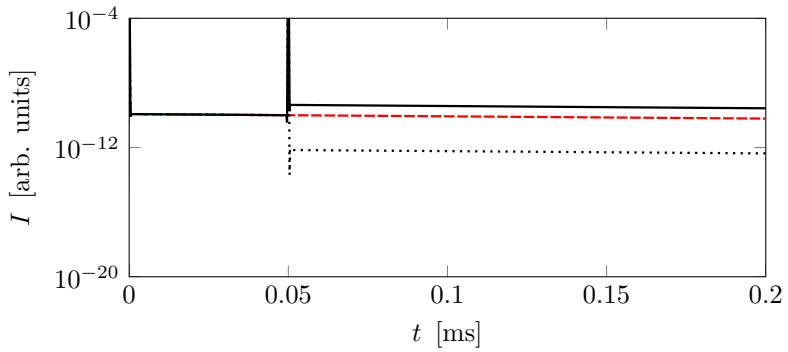

Figure 2.8: Scattered intensity for the two-level thorium system with $\Delta = 0$, $t_0 = 50$ μs, and $T = 0.1$ μs. (Red dashed line) NFS intensity after the first pulse impacting at $t = 0$. (Black solid line) with the additional excitation of a second pulse in phase with the first $\phi = 0$. (Black dotted line) with the additional excitation of a second pulse with $\phi = \pi$.

Considering just two pulses as before where t_0 is the delay time, the intensity $\{I(t)|t > t_0\}$ is

$$\begin{aligned} I(t) &\propto \left| Ne^{-\Gamma_F t/2} + Ne^{-\Gamma_F (t-t_0)/2} e^{i\phi} \right|^2 \\ &= N^2 \left(e^{-\Gamma_F t} + e^{-\Gamma_F (t-t_0)} + 2e^{-\Gamma_F (2t-t_0)/2} \cos\phi \right). \end{aligned} \tag{2.31}$$

The maximal (minimal) intensity is reached when there is no separation between the pulses and they add constructively $\phi = 0$ (destructively $\phi = \pi$). Furthermore, it should be clear that, for long delay time, i.e., $t_0 \gg 1/\Gamma_F$, the initial excited population decays to the ground state and the intensity after the second pulse becomes once again independent of phase $I(t) \approx N^2 e^{-\Gamma_F (t-t_0)}$. See Appendix A.7 for further discussion on testing this superposition model.

2.2.2 Two-level system with $\Delta \neq 0$

Next, we consider the same system as above but now driven with a detuning $\Delta = 10^9\Gamma$. In the case $\Delta \neq 0$ both the real $\Re\{\Omega\}$ and imaginary $\Im\{\Omega\}$ components of the NFS intensity have a nonzero value. Figure 2.9(a) shows the oscillation of the squared real (red dashed line) and imaginary (blue dash-dotted line) components along with the NFS intensity (black solid line) as a result of a single pulse centered at $t = 0$. The oscillation frequencies of $\Re\{\Omega\}$ and $\Im\{\Omega\}$ correspond to the detuning of the laser to the transition frequency, $f_\Omega = \Delta/2\pi$. Alternatively for the intensity, due to the square of the amplitude, i.e., $\Re\{\Omega\}^2$ and $\Im\{\Omega\}^2$, the oscillation frequency is $f_{\Omega^2} = \Delta/\pi$.

Introducing additional pulses is implemented by modifying the initial conditions as shown earlier in Eq. (2.29). The results for $\phi = (0, \pi)$ with $t_0 = (\pi/\Delta, 3\pi/2\Delta, 2\pi/\Delta)$ are shown in Figs. 2.9(b)−2.9(d). Clearly in the case of $\Delta \neq 0$, not only the relative phase ϕ but also the time separation t_0 are of critical importance. This is expressed in the intensity as

$$\begin{aligned} I(t) &\propto \left| Ne^{-\Gamma_F t/2} e^{i\Delta t} + Ne^{-\Gamma_F (t-t_0)/2} e^{i(\Delta(t-t_0)+\phi)} \right|^2 \\ &= N^2 \Big(e^{-\Gamma_F t} + e^{-\Gamma_F (t-t_0)} \\ &\qquad + 2e^{-\Gamma_F (2t-t_0)/2} \cos(\Delta t_0 - \phi) \Big). \end{aligned} \tag{2.32}$$

For $\phi = 0$, maximal (minimal) intensity happens for $t_0 = n\pi/\Delta$, where n is an even (odd) integer. Therefore, by choosing the correct timing and phase we can use multiple pulses to cause increased excitation within the sample that will add constructively at the detector resulting in increased signal intensity.

When searching for a transition with an unknown energy, the case of zero laser detuning is experimentally unlikely. Excitation will first be seen when driven with some nonzero detuning. However, to cause excitation we need to know the energy of the transition well enough to enforce $E_{\Delta i} < E_p$, i.e., the energy width of our pulse has to be wider than the detuning.

To reliably increase the NFS decay intensity with a train of pulses, each successive pulse must cause a constructive excitation in the sample. For this to be the case the detuning of the laser to the excitation must be known. Because this is not the initially true in the search for the Th isomeric

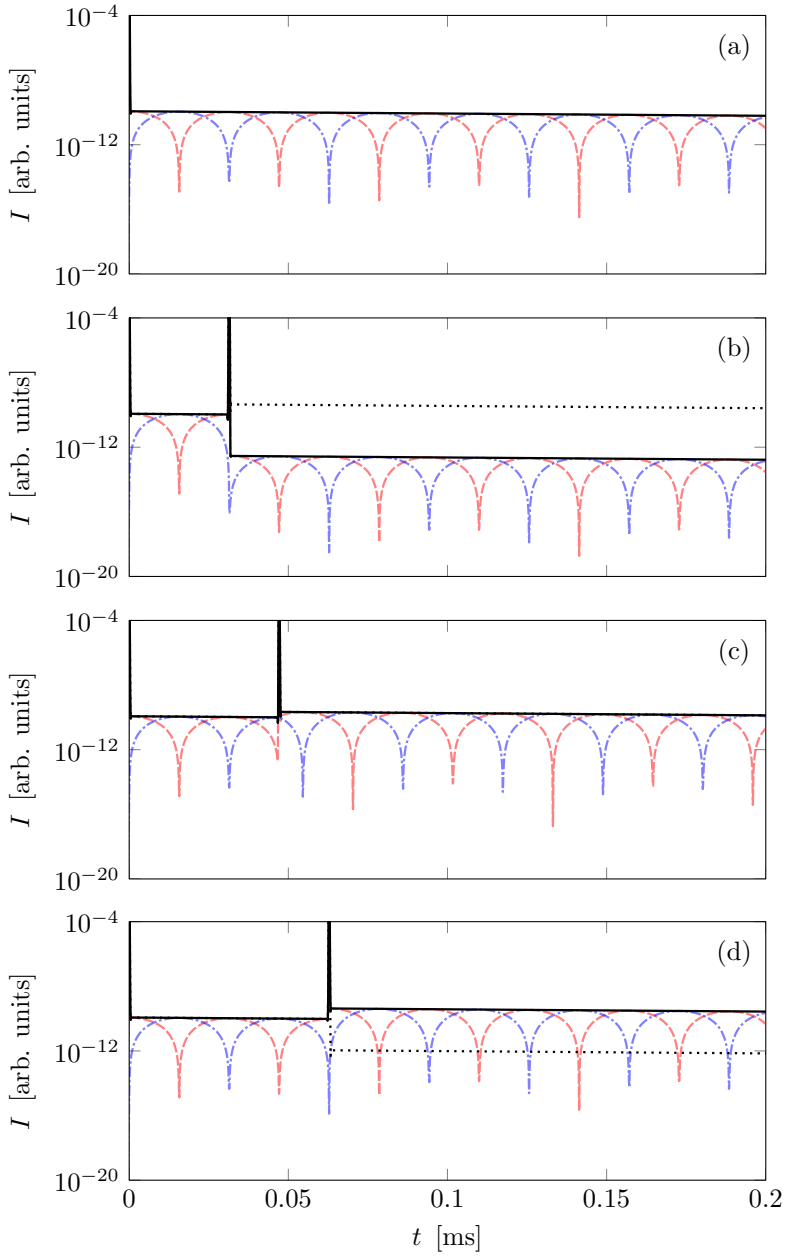

Figure 2.9: Scattered intensity for the two-level thorium system with $\Delta = 10^9\Gamma$ and $T = 0.1$ μs for (a) a single pulse at $t = 0$, (b) the first pulse at $t = 0$ followed by the second one at $t_0 = \pi/\Delta$, (c) the same but with delay between pulses $t_0 = 3\pi/2\Delta$, and (d) for delay between pulses $t_0 = 2\pi/\Delta$. (Black solid line) NFS intensity $|\Omega/\Omega_0|^2$ when using two pulses of the same phase. (Black dotted line) NFS intensity $|\Omega/\Omega_0|^2$ when using two pulses with phase shift π. (Red dashed line) $(\Re\{\Omega\}/\Omega_0)^2$. (Blue dash-dotted line) $(\Im\{\Omega\}/\Omega_0)^2$.

state, we must prevent the chance of destructive interference between the excitation caused by neighboring pulses. To this end, excitation pulses should be spaced out such that $t_0 \gg 1/\Gamma_F$. In this scenario, increasing the NFS intensity can only be accomplished by increasing the number of resonant photons in a single pulse.

If resonance is found in the two-level system, then additional excitation pulses can be introduced. The time delay between the additional excitation pulse can then be varied to find the peak intensity. By plotting the change in intensity as a function of pulse delay, the detuning could be more accurately determined. Repeating the process with a larger pulse train will serve to increase the accuracy of this determination.

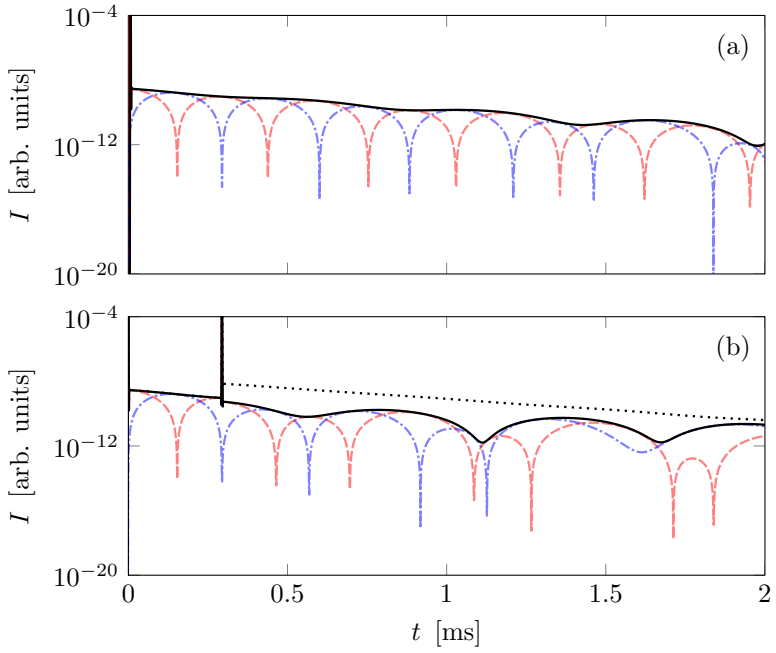

Figure 2.10: Three-level thorium system driven by (a) a single pulse at $t = 0$ or (b) a single pulse at $t = 0$ followed by a second identical pulse at $t = t_0$, which is chosen as the first minimum of $(\Im\{\Omega\}/\Omega_0)^2$. (Black solid line) NFS intensity $|\Omega/\Omega_0|^2$ when using two pulses of the same phase. (Black dotted line) NFS intensity $|\Omega/\Omega_0|^2$ when using two pulses with phase shift π. (Red dashed line) $(\Re\{\Omega\}/\Omega_0)^2$. (Blue dash-dotted line) $(\Im\{\Omega\}/\Omega_0)^2$. For the calculation we have used $\Delta = 10^8\Gamma$, and $T = 0.5$ μs.

2.2.3 Three-level system

The same train of probe pulses can also be applied to drive the three-level thorium system. Analogous to the two-level system, when there is zero detuning the probe pulses of the same phase will always add constructively to the excitation in the sample. However, for nonzero detuning, as shown in the two-level case, both the phase and delay time between pulses play a critical role in the intensity of the NFS spectrum. It is clear here, however, that the complication of this functionality grows quickly with the number of energy levels participating in the signal's generation, as illustrated in Figure 2.10, which shows the calculated spectrum for the three-level system. Our earlier approximation of the $(\Re\{\Omega_p\})^2$ and $(\Im\{\Omega_p\})^2$ oscillation frequency as $f_{\Omega^2} = \Delta_p/\pi$ is inapplicable here. As a result, multiple pulses spaced equally in time will not cause the same constructive effect for $\Delta_p \neq 0$.

To take advantage of a pulse train one must start by exciting the two-level system. Immediately after excitation is generated, the couple laser between states $|\frac{5}{2}, \frac{3}{2}\rangle \rightarrow |\frac{3}{2}, \frac{3}{2}\rangle$ can be introduced. During the time interval when Ω_c is on, the quantum beat is visible with an increased intensity due to the larger excitation in the sample. Then, only after the couple laser is turned off should the sample be further excited with the probe pulse.

2.3 Applied static magnetic field

As mentioned at the start of this chapter, quantum beating can be induced also without the use of a second laser. Instead, we can consider two crystals excited one after the other by the same laser pulse as illustrated in Figure 2.11. By placing one of the two crystals in a static magnetic field the energy levels will be shifted by $\Delta_B = (m_g\mu_g + m_e\mu_e)B/\hbar$, where $(\mu_g, \mu_e, B) = (0.45\mu_N, -0.08\mu_N, 10^{-4}\text{T})$ and $\mu_N = 5.05 \times 10^{-27}$ J/T. The NFS spectrum is then the result of a pair of two-level systems which mimic the results of a three-level system. The resulting quantum beat shown in Figure 2.12 is due to the additional energy shift of the levels in the static magnetic field, resulting in a period $T_{QB} = 2\pi/\Delta_B$.

Analogous to the role of the coupling laser in the three-level system, the static magnetic field can be turned off and on as well as adjusted in magnitude. This allows for switching between a

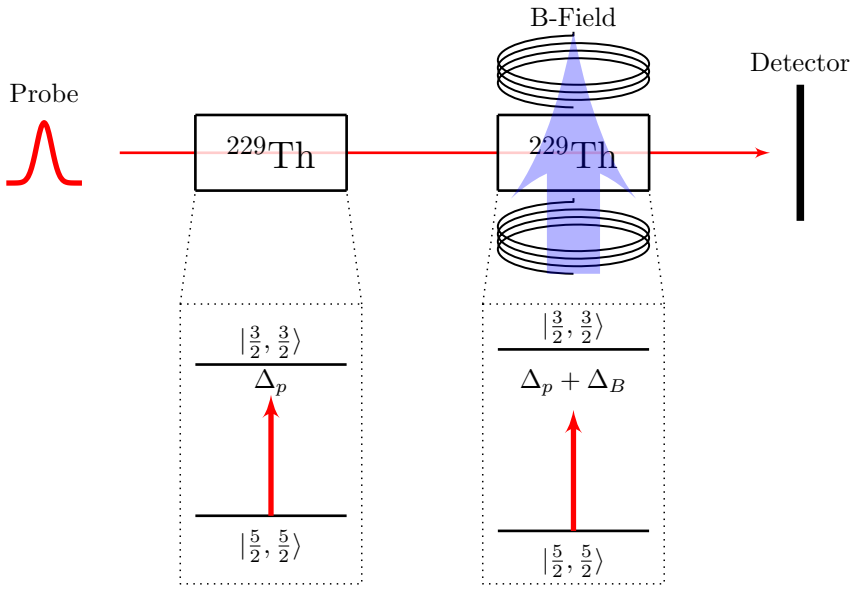

Figure 2.11: Two ^{229}Th:CaF_2 target setup. A left circularly polarized probe field drives the $|\frac{5}{2},\frac{5}{2}\rangle \leftrightarrow |\frac{3}{2},\frac{3}{2}\rangle$ isomeric transitions in both crystals. The detuning of the probe to the unperturbed resonance frequency is denoted by Δ_p. Δ_B denotes the total Zeeman shift due to the external magnetic field B.

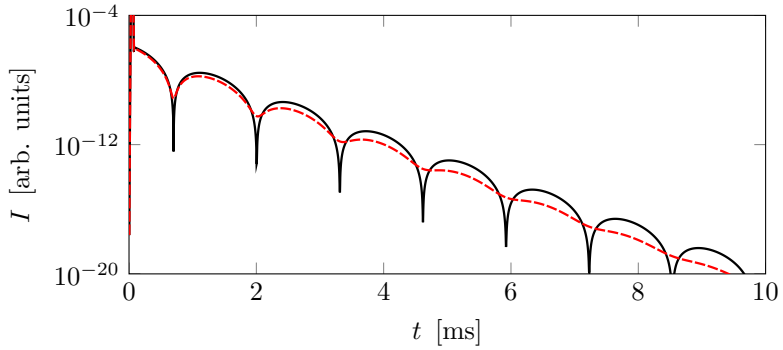

Figure 2.12: Scattered intensity for the case of the two-level system for $\Delta = 0 \sim 10^8\Gamma$ (black solid line) and $\Delta = 10^9\Gamma$ (red dashed line) with static magnetic field $B = 10^{-4}$ T . The excitation occurs for $\Delta < 10^{10}\Gamma \approx \hbar/E_p$.

two-level decay and a three-level quantum beat of variable frequency seen in Figure 2.13, where the applied external magnetic field changes value at the start or end of a beat cycle corresponding to times $t_{switch} \approx (2, 4, 6.6)$ ms.

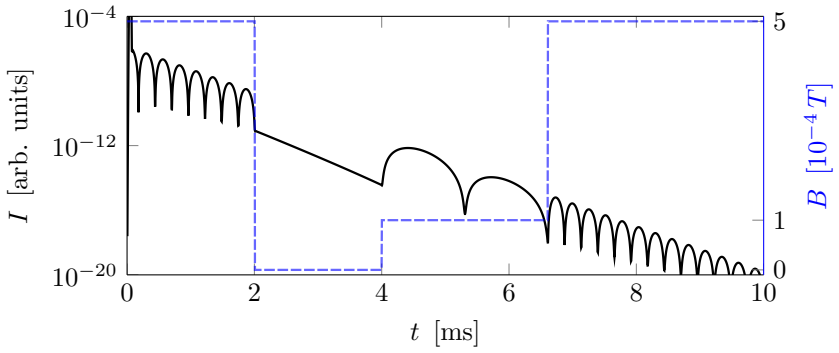

Figure 2.13: Scattered intensity for the two crystal system considering $\Delta = 0$. The applied external magnetic field takes the values $B = 5 \times 10^{-4}$ T, 0 T, 10^{-4} T, and again 5×10^{-4} T.

This setup is more advantageous than the three-level system outlined above because it requires only one tunable laser. Furthermore, when undergoing multipulsed excitation the oscillation frequencies of $\Re\{\Omega\}$ and $\Im\{\Omega\}$ are the same as that of the two-level system $f_\Omega = \Delta/2\pi$ ($f_{\Omega^2} = \Delta/\pi$) and thus the intensity can be reliably changed by varying the frequency of probe pulses while the static field is on. This removes the complication of switching off the couple laser during excitation as would be required in the three-level case.

As a side remark, a slightly modified level scheme becomes available when considering the 90° interstitial configuration or when thorium is doped in a different crystal such as $LiCaAlF_6$. In these cases, due to the change in sign of the electric-field gradient, the lowest-energy level corresponds to $|\frac{5}{2}, \pm\frac{1}{2}\rangle$, seen in Figure 2.2. This state will be initially populated, allowing for two $\Delta m = 0$ transitions to be driven at the same energy. Applying a static magnetic field will split these two transitions in opposite directions due to the sign of m, which results in quantum beating without the use of a second crystal. Thus, in such crystals the two-crystal setup discussed here can be reduced to only a single crystal in a static magnetic field.

Chapter 3

The role of crystal structure and quantization axis

The orientation of the quantization axis (q-axis) plays an important role for the NFS modeling. The q-axis along with the polarization of the exciting field determine the allowed transitions based on angular momentum selection rules. Dopant nuclei with aligned q-axes will undergo the same transitions when exposed to fields of like polarization, however, the same can in general not be said for nuclei with misaligned q-axes. The use of polarized fields to selectively drive transitions is therefore only possible if the majority of the dopant nuclei share a q-axis, or if misaligned nuclei do not contribute to the signal. Thus it is compulsory that one considers the impact of the crystal structure and q-axes at the different Th dopant sites for a reliable modeling of the scattering.

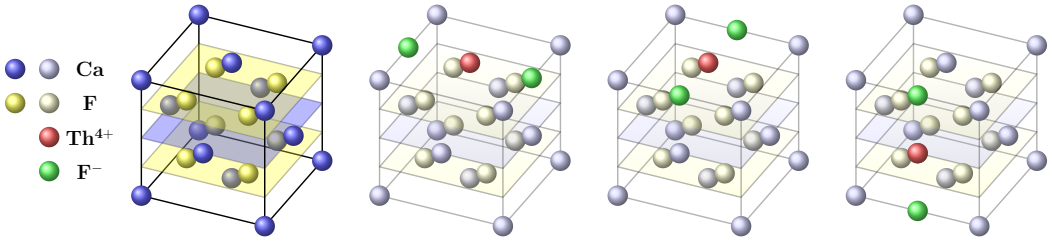

Figure 3.1: Th:CaF_2 structure with 180° fluoride interstitials showing the three possible rotations allowed in a bulk crystal.

As a starting case we will consider the more straightforward treatment of the 180° dopant configuration shown in Figure 2.1 (b). The cubic lattice of CaF_2 is identical when rotated in the xy, yz, or zx planes in increments of 90°. As a result of this rotational symmetry, at low dopant densities where dopant sites do not interact there are three possible orientations of the 180° F-Th-F bond, Figure 3.1. As no orientation is favored, all three options are populated by 1/3 of the total dopant density N. The quantization axis is fixed by the electric-field gradient at the location of the Th nuclei, which in this case is along the F-Th-F bond as shown in Appendix A.8. Hence the three q-axes are mutually perpendicular and can be aligned with the laboratory-frame axes by rotating the crystal and viewing the resulting spectrum.

The energy splitting of all three orientations are the same; however, the angular momentum projections are along the mutually perpendicular q-axis directions. To understand what transitions will be driven we transform the driving field polarization vector into the reference frame of the dopant nuclei. There is no parity change from the ground to excited state making the transition that of a magnetic dipole (M1), therefore as shown in Appendix A.9, $\Delta m = 0$, i.e., π transitions, require a linearly polarized magnetic component of the field parallel to the quantization axis and moving perpendicular to it. $\Delta m = +(-)1$, i.e., $\sigma^{+(-)}$ transitions, require right(left)-circular polarization of the the impinging magnetic component of the field, moving in a direction parallel to the subsystems q-axis[29]. The resultant spectrum is then a combination of the excitation of all three orientations and all driven states.

[29]In this semi classical approach, the wording is meant to draw the parallel between the selection rules of electric and magnetic dipole transitions. If one chooses to strictly talk about the electric field, then the polarization is opposite in the case of magnetic dipole transitions i.e., a M1 transition with $\Delta m = -1$ requires as σ^- B field or equivalently σ^+ E field moving along the quantization axis.

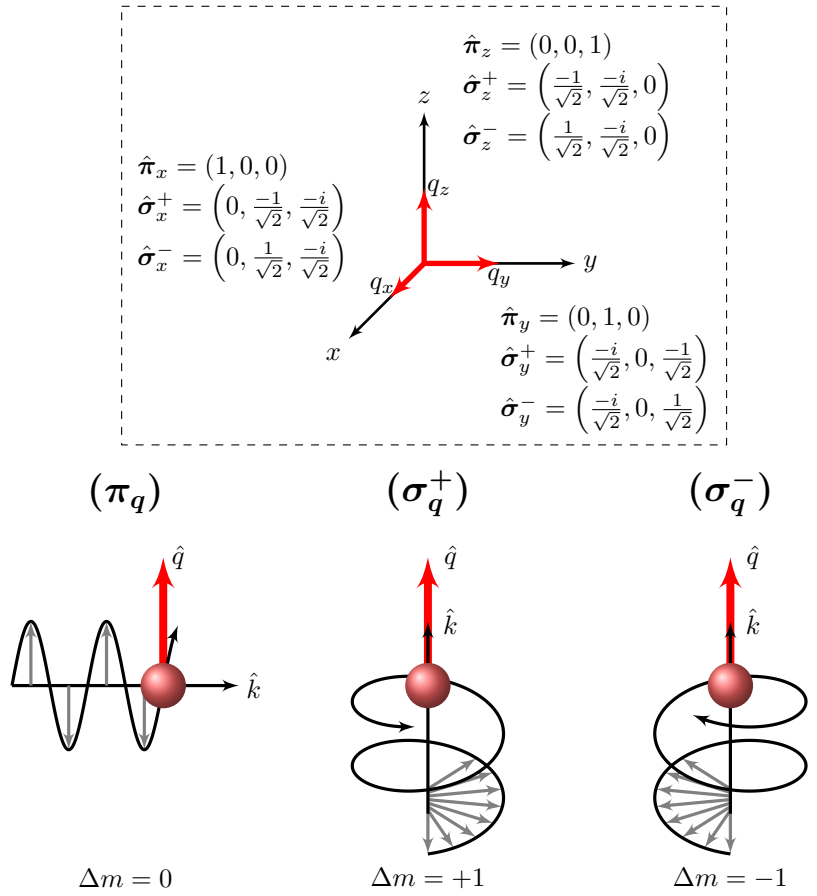

Figure 3.2: Polarization vectors of fields used to drive the $(\pi, \sigma^+, \sigma^-)$ transitions relative to the laboratory frame (x, y, z).

Looking at the 180° case in Figure 2.2 there are 10 states and 12 possible transitions, four of each $(\pi, \sigma^+, \sigma^-)$, for each of the three q-axes $q = (x, y, z)$. By introducing a polarized field, for example σ_y^- (left-circular polarization in the direction y in the laboratory frame), only σ^- transitions can be driven for dopant nuclei with q-axis along y (1/3 of the total). The same σ_y^- polarization can be broken down into components which satisfy the selection rules for driving all transitions in the other two orientations $(\pi_{x/z}, \sigma^+_{x/z}, \sigma^-_{x/z})$ (see Figure 3.2) albeit with lower intensity.

Clearly this situation appears complicated; however, excitation by one and two fields can be simplified to resemble the two- and three-level schemes, respectively shown in Figure 2.3. The key to this simplification becomes obvious only when you consider the relative energy scales of the level widths and their separation, as well as that of the laser field used for excitation. Introducing some notation, let the linewidth of the ^{229m}Th transition in energy be E_γ, the energy spread of a laser pulse with half width in time T be $E_p = \hbar/T$, and let the detuning of the laser to the i^{th} transition be $E_{\Delta i} = \hbar\Delta_i$. $E_\gamma \approx 7 \times 10^{-20}$ eV, which is so narrow that it can be considered an exact energy on the scale of the energy spread of the laser pulses used as well as on the scale of the quadrupole level splitting which is $E_Q = \mathcal{O}(10^{-6})$ eV.

If $E_{\Delta i} > E_p$ there is negligible excitation of the i^{th} transition by the pulse when compared to transitions of smaller detuning. Based on numerical limitations we use pulse widths on the order of μs making the energy spread $E_p = \mathcal{O}(10^{-10})$ eV[30]. Therefore, when considering driving a transition close to resonance, the quadrupole splitting rules out the possibility for the same pulse driving more than two transitions, where the two transitions are degenerate in energy differing only in the sign of the momentum projections $\pm\Delta m$. As a result, for resonance we have $E_\gamma \ll E_{\Delta_i} < E_p < E_Q$ and transitions away from resonance and corresponding states can be safely neglected during calculation. This energy consideration is depicted in Figure 3.3, showing transition $|0\rangle \leftrightarrow |1\rangle$ is resonance and state $|2\rangle$ can be neglected.

Continuing the earlier example with a σ_y^- field is used in resonance with $|\frac{5}{2}, \pm\frac{5}{2}\rangle \rightarrow |\frac{3}{2}, \pm\frac{3}{2}\rangle$ transition, we will compare calculations of the full 10-state level scheme with that of the two-state

[30]Throughout this work we use the notation $\mathcal{O}()$ to denote the order of magnitude of a given quantity.

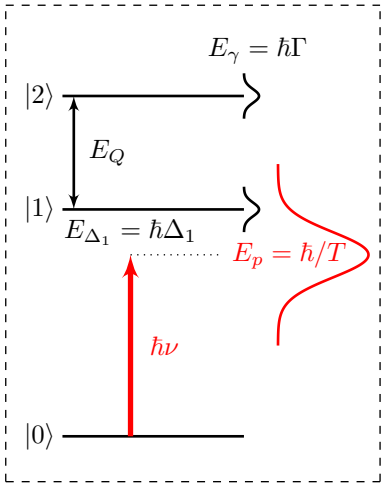

Figure 3.3: Pictorial representation of notation (not to scale). E_γ is the linewidth of the transition in energy; $E_p = \hbar/T$ the energy spread of a laser pulse; $E_{\Delta i} = \hbar\Delta_i$ the detuning of the laser to the i^{th} transition and E_Q the quadrupole splitting.

system shown in Figure 2.3, both with a single q-axis along y. The dopant density used in the two calculations are normalized to that of a crystal with three quantization axes. As such the dopant density of the 10-state system with one q-axis is $N/3$. The initial occupation probability is split equally among the two lowest states $|\frac{5}{2}, \pm\frac{5}{2}\rangle$, i.e. $\rho_{11} = \rho_{22} = 1/2$. Equivalently, the two-state system has an dopant density of of $N/6$ where there is only a single ground state $|\frac{5}{2}, \frac{5}{2}\rangle$ with initial population of unity. The relative difference in spectrum intensity $(I_a - I_b)/I_a$ was calculated as a function of time showing a difference of 0.01%, however this value is dependent on how accurately one solves the set of MBE. Higher accuracy can be reached albeit with increasing computation time. As a result, it is clear that removing the additional levels for which $E_{\Delta i} > E_p$ has a negligible effect on the spectrum, making both calculations effectively identical. This can be understood as follows: For the 10-state system and referring to the state notation in Figure 2.3, the $|1\rangle \rightarrow |7\rangle$ and $|2\rangle \rightarrow |8\rangle$ are the only transitions that are in resonance, however only $|1\rangle \rightarrow |7\rangle$ is driven due to selection rules for σ^-. Furthermore, though there is a minor increase in population of levels $|3\rangle$ and $|5\rangle$ due to radiative decay from $|7\rangle$, they cannot be re-excited due to energy conservation. As such the dominant effect is that of the two-state resonance $|1\rangle \rightarrow |7\rangle$.

At this point it is clear that the calculation can be simplified by removing levels far out of resonance. Now let us consider the effect of multiple quantization axes in a single sample. We recall that σ_y^- field has components along $(\pi_{x/z}, \sigma_{x/z}^+, \sigma_{x/z}^-)$, i.e., fractions of the field have correct polarization to drive all transitions in the other two q-axis orientations. However, the frequency of the field is only in resonance with the $\sigma^\pm$ corresponding to $|\frac{5}{2}, \pm\frac{5}{2}\rangle \rightarrow |\frac{3}{2}, \pm\frac{3}{2}\rangle$. Hence we neglect all other levels which reduces the 10 states to the four states $(|1\rangle, |2\rangle, |7\rangle, |8\rangle)$. As discussed, there is no preferred orientation so the total dopant density N is split with 1/3 in each possible q-axis orientation. Initial occupation probability is equal among the two lowest states $|\frac{5}{2}, \pm\frac{5}{2}\rangle$. Figure 3.4 compares the numerical results of the four-state calculation with three q-axes to that of the simple two-state system of only one q-axis.

As with the last case, here the calculations compare in their functional behavior, however, now yield differing intensities. If the intensity of the signal at time t for the two-state calculation with one q-axis is $I_1^2(t)$ and four state calculation with three q-axes is $I_3^4(t)$, respectively, then $I_3^4(t) \approx 4I_1^2(t)$. This is because the intensity of the signal is proportional to the square of the total number of nuclei making the transition. The intensity of the three q-axis system is greater because σ_y^- can drive more nuclei to the excited state due to its projection on the other two q-axes, which were neglected in the simplified two-state calculation. Vector projection gives fields of half amplitude driving $\sigma_{x/z}^{+/-}$, which result in a contribution of $\approx \frac{1}{2}I_1^2(t)$ from each of the x and z q-axis populations. These then add in superposition with matching polarization to give the final result,

$$\begin{aligned} I_3^4 &\approx \left(A_x + \frac{A_x}{2} + \frac{A_x}{2}\right)^2 + \left(A_z + \frac{A_z}{2} + \frac{A_z}{2}\right)^2 \\ &= 4(A_x^2 + A_z^2) = 4I_1^2. \end{aligned} \tag{3.1}$$

The intensity differences written here correspond to exactly a combination of independent sys-

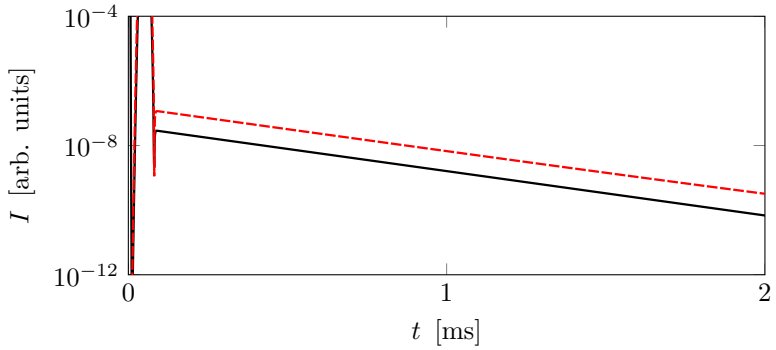

Figure 3.4: Scattered intensity for (black solid line) two-state system, one q-axis, dopant density $N/6$ with initial population of $|\frac{5}{2}, \frac{5}{2}\rangle$ and (red dashed line) four-state system, three q-axes, dopant density N with 1/3 in each possible q-axis orientation, initial population split equally among two lowest states $|\frac{5}{2}, \pm\frac{5}{2}\rangle$. The calculations were performed considering $\Delta = 0$ for the transition $|\frac{5}{2}, \pm\frac{5}{2}\rangle \rightarrow |\frac{3}{2}, \pm\frac{3}{2}\rangle$.

tems. Our numerical calculations show a slight deviation from this independent system treatment due to multiple scattering between q-axis subsystems. This difference is on the order of a few percent which can easily be neglected when looking at the main effects involved. A detailed description of the implementation of multi-quantization axis calculations is presented in Appendix A.10.

3.1 Lowest energy configuration: $\eta \neq 0$

The lowest-energy dopant configuration found in [8] requires fluoride interstitials making a 90° angle with the dopant thorium, which takes the position of a Ca shown in Figure 2.1(a). The same symmetry applies where the crystal can be rotated in the xy, yz, or zx planes in increments of 90°; only in this case due to the angled F-Th-F bond there are 12 orientations. This is not a problem as the electric-field gradient runs perpendicular to the plane defined by the angled F-Th-F bond making the 12 orientations fourfold degenerate. As such there are only three orientations of the quantization axis, just like before.

In this dopant orientation $V_{zz} = 223$ VÅ^{-2} [8], and the change in sign of the electric-field gradient reverses the ordering of the split levels in terms of energy as compared to the 180° case shown in Figure 2.3. Furthermore, the 90° configuration has a nonzero asymmetry parameter $\eta = 0.48$. In this case, the angular momentum projection m is no longer a good quantum number to define the nuclear states. $0 \leq \eta \leq 1$ and the larger η becomes, the more mixing there is between sublevels. The E2 Hamiltonian (2.1) given again here,

$$\hat{H}_{E2} = \frac{eQV_{zz}}{4I(2I-1)}\left[3\hat{I}_z^2 - \hat{I} + \frac{\eta}{2}\left(\hat{I}_+^2 + \hat{I}_-^2\right)\right],$$

can be diagonalized to find the eigenvalues and eigenvectors, which are shown here for the relevant angular momentum $(I_g, I_e) = \left(\frac{5}{2}^+, \frac{3}{2}^+\right)$ [75–78]. Figures 3.5 and 3.7 show the energy of the split ground and excited states where $C_{g/e} = eQ_{g/e}V_{zz}/(4I_{g/e}(2I_{g/e}-1))$. Figures 3.6 and 3.8 show the squared projection of the state vectors with the eigenstates of nuclear spin angular momentum. The energy splitting is still of the order 10^{-6} eV. Therefore, once again when driving a transition close to resonance, the quadrupole splitting rules out the possibility for the same pulse driving more than two transitions, where the two transitions are degenerate in energy differing only by the sign of the states' m projections.

What is different in this case is that the angular momentum selection rules can be satisfied in more than one way for a given transition. Each state can now be defined as a superposition of angular momentum eigenstates where the probability to be in a given eigenstate is given by $|\langle I, m'|I, \psi_m(\eta)\rangle|^2$, where $|I, m\rangle$ is an eigenstate of angular momentum with projection m and $|I, \psi_{m'}(\eta)\rangle = \sum_m a_m(\eta)|I, m\rangle$ is the state vector with the largest contributing component coming from state $|I, m'\rangle$. For example, consider the transition from $|\frac{5}{2}, \xi_{1/2}(\eta)\rangle \rightarrow |\frac{3}{2}, \phi_{1/2}(\eta)\rangle$. If the laser has the correct energy within the energy width of the pulse, then only the polarization determines

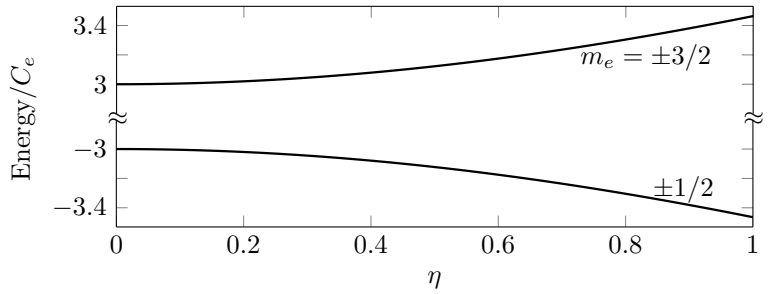

Figure 3.5: Energy eigenvalues of $\hat{H}_{E2}$ for $I = I_e = 3/2$ as a function of the asymmetry parameter η. Labeled with the spin projection m_e with respect to the largest field component.

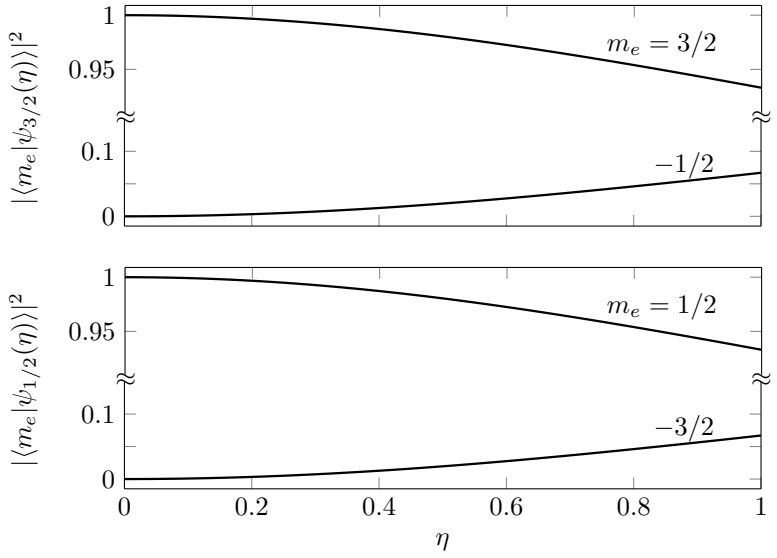

Figure 3.6: Squared projection of state vector $|\frac{3}{2}, \psi_m(\eta)\rangle$ on overlapping eigenstates of angular momentum as a function of the asymmetry parameter η.

whether the transition will be driven. Expanding the state vectors we see

$$\begin{aligned} |\tfrac{5}{2}, \xi_{1/2}(\eta)\rangle &= a_1|\tfrac{5}{2}, \tfrac{1}{2}\rangle + a_2|\tfrac{5}{2}, -\tfrac{3}{2}\rangle + a_3|\tfrac{5}{2}, \tfrac{5}{2}\rangle, \\ |\tfrac{3}{2}, \phi_{1/2}(\eta)\rangle &= b_1|\tfrac{3}{2}, \tfrac{1}{2}\rangle + b_2|\tfrac{3}{2}, -\tfrac{3}{2}\rangle, \end{aligned} \tag{3.2}$$

and hence only $\Delta m = 0$ transitions are possible. To understand the relative strength of the transitions we calculate the square of the overlap integral $|\langle I_g, m_g|\langle J, M|I_e, m_e\rangle|^2$ [76, 79], where the excited state $|I_e, m_e\rangle$ is connected to the ground state $|I_g, m_g\rangle$ and the emitted photon $|J, M\rangle$ via the Clebsch-Gordan coefficients,

$$|I_e, m_e\rangle = \sum_M C^{I_g\ J\ I_e}_{m_g M m_e} |J, M\rangle|I_g, m_g\rangle. \tag{3.3}$$

For the above transition

$$\begin{aligned} \langle \tfrac{5}{2}, \xi_{1/2}(\eta)|\langle J, M|\tfrac{3}{2}, \phi_{1/2}(\eta)\rangle = b_1\langle \tfrac{5}{2}, \xi_{1/2}(\eta)|\langle J, M| \sum_{m_g, M} C^{\frac{5}{2}\ J\ \frac{3}{2}}_{m_g M \frac{1}{2}} |J, M\rangle|\tfrac{5}{2}, m_g\rangle \\ + b_2\langle \tfrac{5}{2}, \xi_{1/2}(\eta)|\langle J, M| \sum_{m_g, M} C^{\frac{5}{2}\ J\ \frac{3}{2}}_{m_g M -\frac{3}{2}} |J, M\rangle|\tfrac{5}{2}, m_g\rangle, \end{aligned} \tag{3.4}$$

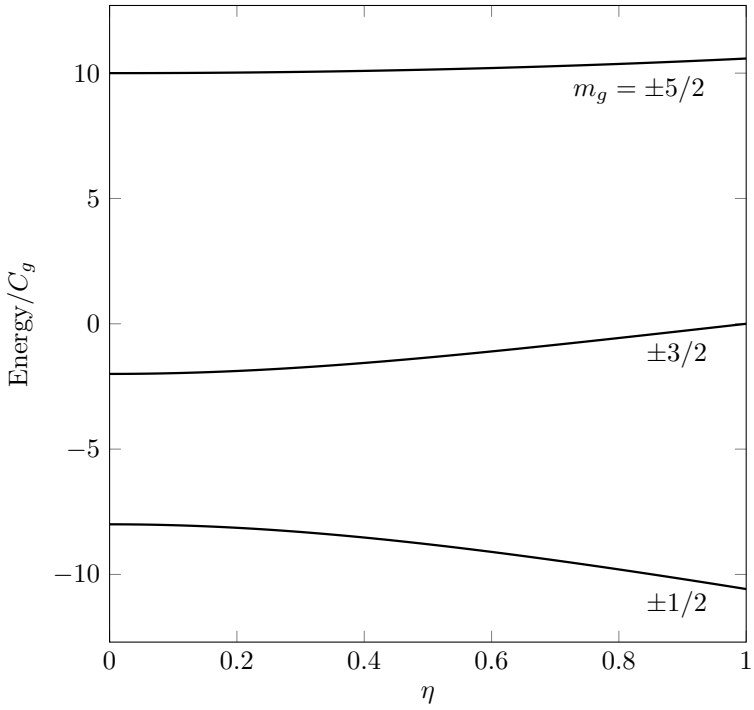

Figure 3.7: Energy eigenvalues of $\hat{H}_{E2}$ for $I = I_g = 5/2$ as a function of the asymmetry parameter η. Labeled with the spin projection m_g with respect to the largest field component.

Focusing on M1 type transitions we can have $J = 1$ with $M = \{1, 0, -1\}$ which leaves only,

$$\begin{aligned}\langle \tfrac{5}{2}, \xi_{1/2}(\eta)|\langle 1, M|\tfrac{3}{2}, \phi_{1/2}(\eta)\rangle &= b_1\langle \tfrac{5}{2}, \xi_{1/2}(\eta)| \sum_{m_g,M} C^{\frac{5}{2}\ 1\ \frac{3}{2}}_{m_g M \frac{1}{2}} |\tfrac{5}{2}, m_g\rangle \\ &\quad + b_2\langle \tfrac{5}{2}, \xi_{1/2}(\eta)| \sum_{m_g,M} C^{\frac{5}{2}\ 1\ \frac{3}{2}}_{m_g M -\frac{3}{2}} |\tfrac{5}{2}, m_g\rangle, \qquad (3.5)\\ &= a_1 b_1 C^{\frac{5}{2}1\frac{3}{2}}_{\frac{1}{2}0\frac{1}{2}} + a_2 b_2 C^{\frac{5}{2}\ 1\ \frac{3}{2}}_{-\frac{3}{2}0-\frac{3}{2}}, \qquad (3.6)\\ & \qquad (3.7)\end{aligned}$$

where the Clebsch-Gordan coefficients require $m_g + M = m_e$ to be non zero. The coefficients for $\eta = 0.48$ are $(a_1, a_2, a_3, b_1, b_2) = (0.95, 0.29, 0.08, 0.99, 0.13)$ and correspond to the square root of values taken from Figs. 3.6 and 3.8. Comparing the intensity to a transition between pure eigenstates of angular momentum (i.e., the unmixed case of $\eta = 0$) results in

$$\frac{\left|\langle \tfrac{5}{2}, \xi_{1/2}(0.48)|\langle 1, 0|\tfrac{3}{2}, \phi_{1/2}(0.48)\rangle\right|^2}{\left|\langle \tfrac{5}{2}, \tfrac{1}{2}|\langle 1, 0|\tfrac{3}{2}, \tfrac{1}{2}\rangle\right|^2} \approx 0.98. \qquad (3.8)$$

Hence the intensity of this transition is lowered by $\approx 2\%$ due to mixing of states. In general, for our case $|\langle I, m|I, \psi_m(0.48)\rangle|^2 > 0.9$ for all I and m. As a result the intensity of the signal will drop in relation to the smaller population undergoing the transition. Clearly, this is negligible for our purposes. As such the results shown in Chapter 2 apply in this case with minor intensity corrections.

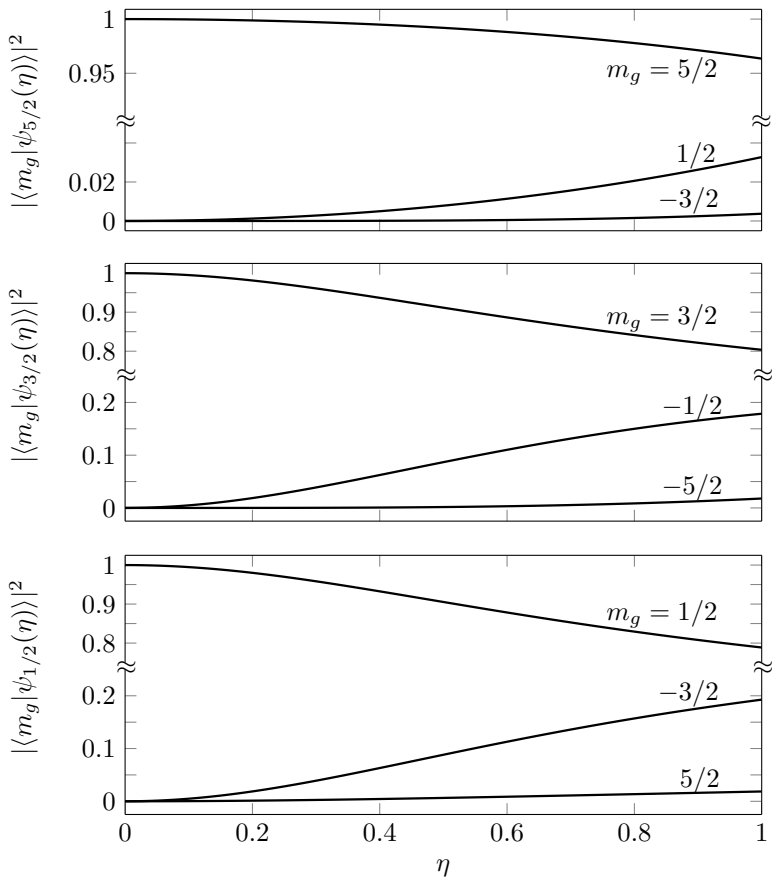

Figure 3.8: Squared projection of state vector $|\frac{5}{2}, \psi_m(\eta)\rangle$ on overlapping eigenstates of angular momentum as a function of the asymmetry parameter η.

Part II

Electronic Bridge process in Doped Crystals

Chapter 4

Theoretical Background for Electronic Bridge

The large band gap of VUV-transparent crystals would ideally make them transparent in the energy region of interest for the nuclear excitation of thorium's isomeric state. In practice however, crystals such at CaF_2 do not provide us with an inert host. As discussed in the introduction, the act of doping thorium into CaF_2 results in crystal defects in the form of localized electronic states around the thorium nuclei, termed color-center states. These states are believed to sit within the band gap of the crystal [8, 22]. Their presence makes not only the direct nuclear excitation more difficult but also the measurement of the nuclear decay via schemes such as NFS. This is because during experiment there are additional parasitic signals coming form the electronic shell which are not considered in NFS. The previous part of this dissertation covering NFS neglects the role of the color-center states, and focuses on direct nuclear excitation alone. In this part, we are interested in the use of color-center states for nuclear excitation via Electronic Bridge (EB). We will calculate of the rate of excitation of the isomeric state via EB and compare it to rate of direct excitation.

In this chapter we will begin with a general treatment of EB theory and outline the non-relativistic operators involved. In Chapter 5 we contrast the electronic wave functions of the crystal environment with atomic wave functions of ions, both within the context of EB rate calculation. We then apply for the first time the general EB formalism to thorium-doped crystals. Our results for a variety of spontaneous and stimulated EB schemes are given in Chapter 6. EB will be shown to provide a promising channel of excitation that exploits color-center states for the purpose of nuclear excitation. Finally, Chapter 7 outlines the computational difficulties and approximations related to calculation of EB rates within the crystal.

EB describes a process whereby the nucleus decays via transfer of energy to the electronic shell with the emission of a photon. It is assumed that there is a mismatch between the nuclear transition energy and the available electronic transitions. Note that in EB, the decaying nucleus does not provide enough energy to cause ionization as is the case in IC [37, 80].

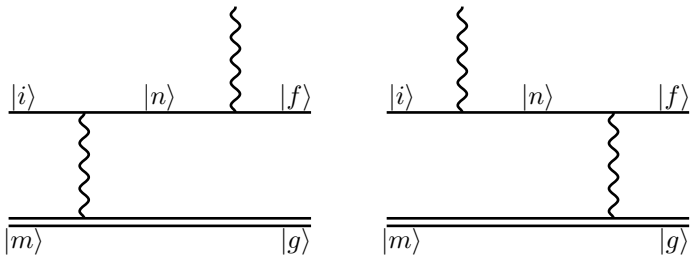

Figure 4.1: Electronic transition moves along single solid line from $|i\rangle \rightarrow |n\rangle \rightarrow |f\rangle$, and nuclear transition moves along double solid line from $|m\rangle \rightarrow |g\rangle$. The initial, intermediate and final electronic states are $|i\rangle$, $|n\rangle$ and $|f\rangle$ respectively. The nuclear isomeric and ground states are $|m\rangle$ and $|g\rangle$ respectively. The wiggly lines represent transfer of energy via photon.

The Feynman diagrams describing this process [38] are shown in Figure 4.1 where the electronic state moves along the single solid line from initial state $|i\rangle$ to intermediate $|n\rangle$ to final $|f\rangle$, and nuclear state moves along the double solid line from the isomeric $|m\rangle$ to the ground state $|g\rangle$. The

wiggly lines represent photons. There are two Feynman diagrams differing in the order in which the transition happens, i.e., first a transfer of energy between the nucleus and the electronic shell or first the emission of a photon from the electronic shell. Moving from left to right in Figure 4.1 describes decay of the isomeric state. Both diagrams contribute to the EB process.

An alternative illustration of EB is given in Figure 4.2. The combined nuclear and electronic system moves from its initial to final state (labeled "Start" and "Finish" respectively) via the two possible paths corresponding to the two Feynman diagrams of Figure 4.1. The top and bottom paths of Figure 4.2 correspond to the first and second Feynman diagrams of Figure 4.1. Following the top path, upon the decay of the nucleus the electron is excited to a virtual state at the energy of the nuclear transition, $\omega_v - \omega_i \equiv \omega_{vi} = \omega_{mg}$. This virtual state decays to a real electronic state emitting a real photon of energy equal to the energy difference of the nuclear and electronic transitions, $\omega_p = \omega_{mg} - \omega_{fi}$. Alternatively on the bottom path, the electron first decays to a virtual state emitting a photon and is then excited to the final state via the decay of the nucleus.

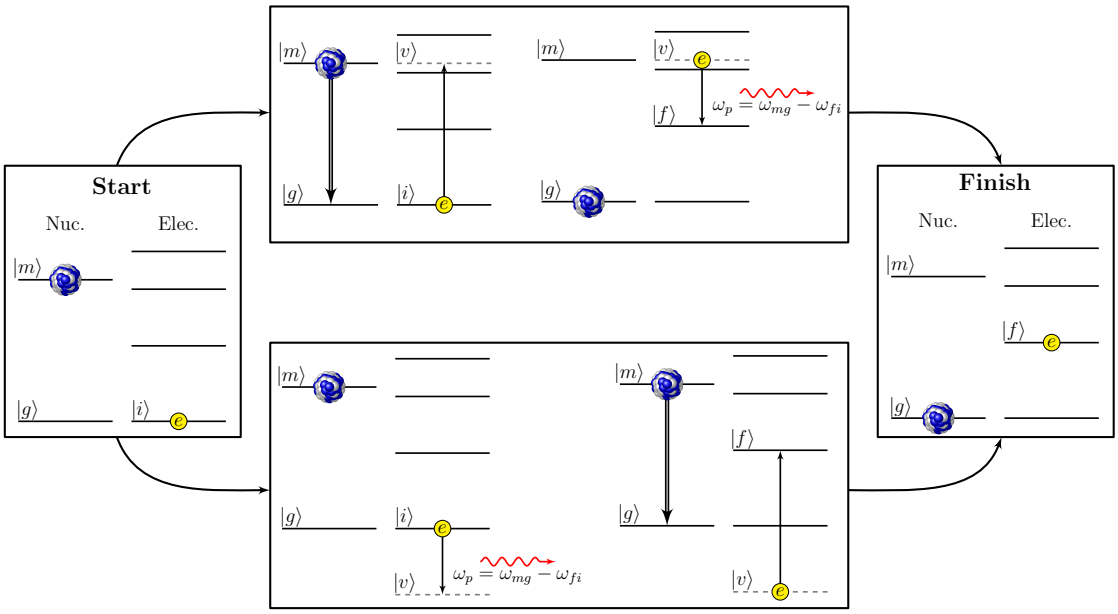

Figure 4.2: Illustration of nuclear decay via EB process. Both possible EB paths from Start to Finish are shown. In the top path, the excited nucleus decays $|m\rangle \to |g\rangle$ passing its energy to an electron which is excited to a virtual (dashed) state $|i\rangle \to |v\rangle$. The virtual electronic state then decays to a real state $|v\rangle \to |f\rangle$ emitting a real photon. In the bottom path, first the electronic state under goes decay emitting a photon and is then excited to the final state by the decaying nucleus.

Following [38], provided the intermediate and final electronic states are of opposite parity, the rate can be effectively described as an electric dipole (E1) transition. Thus, the outgoing photon lines from the electronic shell in Figure 4.1 are E1 photons. As such the EB process can be described by the amplitude of the electric dipole transition mediated by the nuclear transition from isomeric state to ground state. The effective E1 bridge operator $\widetilde{\boldsymbol{D}}_{E1}$ is given by,

$$\langle g, f|\widetilde{\boldsymbol{D}}_{E1}|m, i\rangle = \sum_n \frac{\langle f|\boldsymbol{D}_{E1}|n\rangle\langle g, n|H_{int}|m, i\rangle}{\varepsilon_i + E_m - \varepsilon_n - E_g + i\Gamma_n/2} + \sum_k \frac{\langle g, f|H_{int}|m, k\rangle\langle k|\boldsymbol{D}_{E1}|i\rangle}{\varepsilon_f + E_g - \varepsilon_k - E_m + i\Gamma_k/2} \tag{4.1}$$

where the states are denoted for example $|m, i\rangle = |m\rangle|i\rangle$ where m represents the quantum numbers defining the nuclear state (in this case the isomer) and i the quantum numbers of the electronic state (in this case the initial state). The energy of the i^{th} electronic state is ε_i, and the energy of the nuclear isomer and ground states are E_m and E_g respectively. The widths of the intermediate states, Γ_n, are assumed small in comparison to the energies of the involved transitions and thus are neglected.

Our units of choice for this section are atomic units with $\hbar = e = m_e = 4\pi\varepsilon_0 = 1$ where $c \approx 137$, unless otherwise stated. The interaction Hamiltonian is given by separating the nuclear and electronic components. In spherical basis, see Appendix A.11, we can write

$$H_{int} = \sum_{\lambda K, q} \mathcal{M}^q_{\lambda K} \mathcal{T}_{\lambda K, q} = \sum_{\lambda K, q} (-1)^q \mathcal{M}_{\lambda K, -q} \mathcal{T}_{\lambda K, q} \tag{4.2}$$

where $\mathcal{M}_{\lambda K,q}$ are the multipole nuclear moments and $\mathcal{T}_{\lambda K,q}$ the electronic coupling operators with $\lambda = (E, M)$ referring to the interaction type electric or magnetic, where K is the rank and $q = \{K, K-1, \ldots, -K\}$ the spherical basis component. As a result the effective electric dipole operator is,

$$\langle g, f|\widetilde{\boldsymbol{D}}_{E1}|m, i\rangle = \sum_{\lambda K,q}(-1)^q \left[\sum_n \frac{\langle f|\boldsymbol{D}_{E1}|n\rangle\langle n|\mathcal{T}_{\lambda K,q}|i\rangle}{\omega_{in}+\omega_N} + \sum_k \frac{\langle f|\mathcal{T}_{\lambda K,q}|k\rangle\langle k|\boldsymbol{D}_{E1}|i\rangle}{\omega_{fk}-\omega_N}\right]\langle g|\mathcal{M}_{\lambda K,-q}|m\rangle,$$

where $\omega_{in} = \omega_i - \omega_n$, $\omega_{fk} = \omega_f - \omega_k$ and $\omega_N = \omega_{mg} = \omega_m - \omega_g$ are transition energies between the respective states. The two summations over intermediate states $\{n, k\}$ correspond to the two Feynman diagrams in Figure 4.1. It is these summations that contribute to the so called virtual state $|v\rangle$. All states that take part are assumed to be unoccupied such that a transition, however unlikely, could take place via these levels, i.e., occupied levels cannot be used. The contribution of each term in the summation to the rate depends on the energy difference between these states as seen in the denominators of the summands. If the electronic transition energy to the intermediate state is far greater $(\omega_{in}, \omega_{fk}) \gg \omega_N$ or far less $(\omega_{in}, \omega_{fk}) \ll \omega_N$ than the nuclear transition, the denominator becomes large and the intermediate state does not contribute significantly to the total rate. Hence, the number of intermediate states must be increased until the matrix elements of the effective electric dipole operator converge.

The decay rate of the EB process is given by,

$$\Gamma_{EB} = \frac{4}{3}\left(\frac{\omega_p}{c}\right)^3 \frac{1}{N_m N_i}\sum_{\substack{m,g,\\ i,f,q}} |\langle g, f|\widetilde{D}_{E1,q}|m, i\rangle|^2,$$

where we sum over all possible intermediate and final states and average over initial states, and N_m and N_i are the number of degenerate states in the set of nuclear $\{|m\rangle\}$ and electronic $\{|i\rangle\}$ levels respectively. $\widetilde{D}_{E1,q}$ are the spherical basis components of the effective electric dipole operator where $q = \{1, 0, -1\}$. The energy of the emitted photon is given by ω_p and depends on the energy of the initial and final states of the electronic shell as well as that of the nucleus. In the case of spontaneous decay of the isomeric state via EB, we require that $\omega_N > \omega_{fi}$ and hence $\omega_p = \omega_N - \omega_{fi}$.

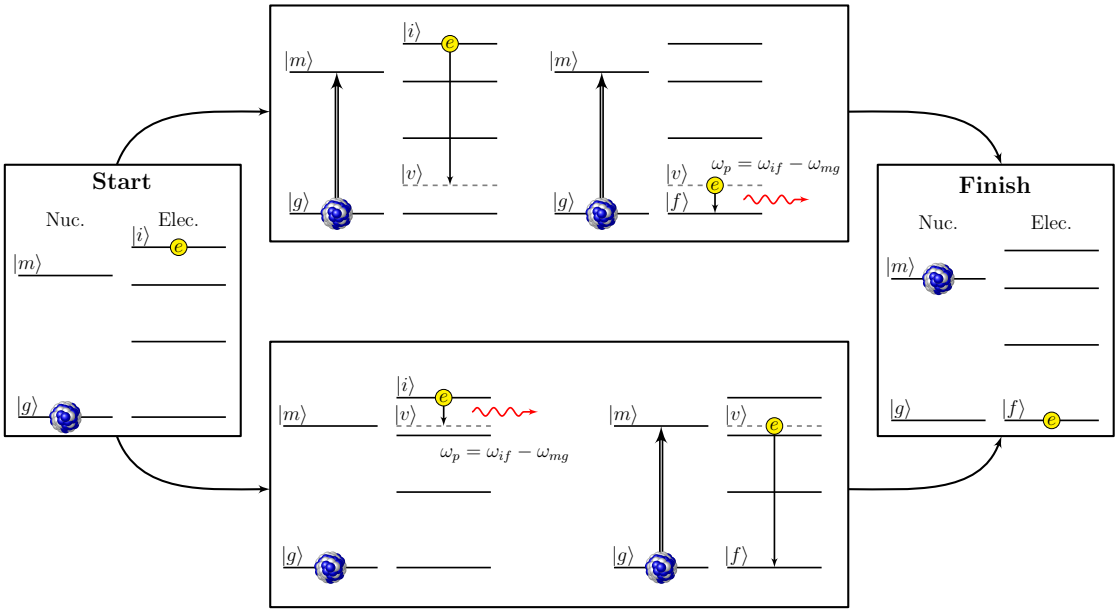

Figure 4.3: Illustration of nuclear excitation via EB process. Both possible EB paths from Start to Finish are shown. In the top path, the excited electron decays $|i\rangle \to |v\rangle$ exciting the nucleus first $|g\rangle \to |m\rangle$ and then further decays $|v\rangle \to |f\rangle$ emitting a photon of energy $\omega_p = \omega_{if} - \omega_{mg}$. In the bottom path, the electron decays by first emitting a photon and then exciting the nucleus.

Up until this point we have discussed the EB process in the context of a decaying nucleus. EB can however be used for excitation of the nucleus provided we have initially excited an electron to a bound state with energy larger than that of the nuclear transition. This is depicted in Figure

4.3, where once again there are two EB paths corresponding to the two the Feynman diagrams in Figure 4.1 with the nuclear states swapped in position $|m\rangle \leftrightarrow |g\rangle$. In the top path, the electron decays to a virtual state exciting the nucleus and then further decays to a real final state emitting a photon with energy $\omega_p = \omega_{if} - \omega_N$. In the bottom path, the electron decays to a virtual state emitting a real photon with energy $\omega_p = \omega_{if} - \omega_N$, and then further decay to a real state passing the difference in energy, $\omega_{vf} = \omega_{mg}$, to the nucleus. To avoid clutter, all following figures will display only one of these paths, however unless otherwise stated both contribute and are considered.

Both of these EB processes are spontaneous in that with the nucleus and electronic shell prepared in the described initial states the processes require no additional energy to take place. This being said, to differentiate the schemes while making note that we are discussing the spontaneous EB process, we will refer to the direction of the nuclear transition involved. As such, Figure 4.2, refers to spontaneous decay of the isomeric state via EB, and Figure 4.3, refers to spontaneous excitation of the isomeric state via EB. It should be clear that both cases happen spontaneously with a release of a real photon. The only difference is the direction of energy transfer, either from the nucleus to the electronic shell or vice versa.

Rewriting the relevant equations we have first for spontaneous decay via EB

$$\Gamma^{sp}_{EB}(g,f;m,i) = \frac{4}{3}\left(\frac{\omega_p}{c}\right)^3 \frac{1}{N_m N_i} \sum_{\substack{m,g,\\ i,f,q}} |\langle g,f|\widetilde{D}_{E1,q}|m,i\rangle|^2, \tag{4.3}$$

$$\langle g,f|\widetilde{\boldsymbol{D}}_{E1}|m,i\rangle = \sum_{\lambda K,q}(-1)^q \left[\sum_n \frac{\langle f|\boldsymbol{D}_{E1}|n\rangle\langle n|\mathcal{T}_{\lambda K,q}|i\rangle}{\omega_{in}+\omega_N} + \sum_k \frac{\langle f|\mathcal{T}_{\lambda K,q}|k\rangle\langle k|\boldsymbol{D}_{E1}|i\rangle}{\omega_{fk}-\omega_N}\right]\langle g|\mathcal{M}_{\lambda K,-q}|m\rangle, \tag{4.4}$$

where the emitted photon energy is $\omega_p = \omega_N - \omega_{fi}$. Similarly, for spontaneous excitation via EB

$$\Gamma^{sp}_{EB}(m,f;g,i) = \frac{4}{3}\left(\frac{\omega_p}{c}\right)^3 \frac{1}{N_g N_i} \sum_{\substack{m,g,\\ i,f,q}} |\langle m,f|\widetilde{D}_{E1,q}|g,i\rangle|^2, \tag{4.5}$$

$$\langle m,f|\widetilde{\boldsymbol{D}}_{E1}|g,i\rangle = \sum_{\lambda K,q}(-1)^q \left[\sum_n \frac{\langle f|\boldsymbol{D}_{E1}|n\rangle\langle n|\mathcal{T}_{\lambda K,q}|i\rangle}{\omega_{in}-\omega_N} + \sum_k \frac{\langle f|\mathcal{T}_{\lambda K,q}|k\rangle\langle k|\boldsymbol{D}_{E1}|i\rangle}{\omega_{fk}+\omega_N}\right]\langle m|\mathcal{M}_{\lambda K,-q}|g\rangle, \tag{4.6}$$

where the emitted photon energy is now $\omega_p = \omega_{if} - \omega_N$. The notation used here is similar to Sobelman [81]: $\Gamma_\zeta(\beta,b;\alpha,a)$ represents the transition rate from the nuclear state $|\alpha\rangle$ with electronic state $|a\rangle$ to that of nuclear state $|\beta\rangle$ and electronic state $|b\rangle$ via process ζ. The notation can explicitly state if the process happens spontaneously (sp) or is stimulated (st) or requires absorption (a) of photon with energy E_ω coming from a source with power P_ω and where $\omega = \omega_p$. By calculating the rate of the spontaneous process we can determine the rate of the stimulated process or inverse process requiring absorption of an externally provided laser photon. This is done using the following formula [81, p.204][82][37, p.40],

$$\Gamma^{st}(b;a) = \Gamma^{sp}(b;a)\frac{4\pi^3 c^2\hbar^2}{E^3_\omega}P_\omega = \Gamma^{sp}(b;a)F_\omega P_\omega \tag{4.7}$$

$$\Gamma^{a}(a;b) = \Gamma^{sp}(b;a)F_\omega P_\omega \delta(b;a) \tag{4.8}$$

where $\Gamma^{sp}(b;a)$ is the rate of the spontaneous process from $|a\rangle \to |b\rangle$, $\Gamma^{st}(b;a)$ is the rate of the stimulated process from $|a\rangle \to |b\rangle$, and $\Gamma^{a}(a;b)$ is the rate of the inverse absorption process from $|b\rangle \to |a\rangle$. The spectral power of the laser source is P_ω in W/(m^2 Hz), with the required photon energy $E_\omega = \hbar\omega$, and $\delta(b;a) = N_a/N_b$ is the ratio of number of levels in the sets $\{|a\rangle\}$ vs $\{|b\rangle\}$. As can be seen for example in (4.3) the rate is averaged over the number of initial nuclear and electronic states, and hence $N_a = N_m N_i$ is the total degeneracy of the initial state of the combined nuclear and electronic system. Therefore, δ takes into account the change in averaging when reversing the process, i.e., change in degeneracy or change in number of levels considered for initial and final states. Note that $F_\omega P_\omega \delta(b;a)$ is dimensionless. In this section all equations are in atomic units, however here we chose to use SI and quote the powers in the more standard W/(m^2 Hz). Energy is still listed in eV but must be converted to J for use here or Hartree in the case of atomic units.

In the following section we will discuss application of these equations to EB in the crystal environment along with the operators, $\mathcal{M}_{\lambda K,-q}$ $\mathcal{T}_{\lambda K,q}$ and $\boldsymbol{D}_{E1}$, required to calculate EB transition rates.

4.1 Operators

The operators of interest here are electric dipole (E1), as well and magnetic dipole (M1) electric quadrupole (E2) coupling operators. The nuclear transition decays via both M1 and E2 channels as shown in [3, 36]. Depending on the situation the higher multipolarity E2 transition may even dominate and as such it cannot be ignored.

4.1.1 Nuclear operators

The absolute value of matrix elements of the nuclear transition operator are found using reduced transition probabilities from [3] given as $\mathbb{B}_\downarrow$ values in Weisskopf units

$$\mathbb{B}_W(M1, m \to g) = 0.0076 \text{ W.u.}, \tag{4.9}$$
$$\mathbb{B}_W(E2, m \to g) = 27.04 \text{ W.u.}, \tag{4.10}$$

which convert to usual units of μ_N^2 and $e^2(fm)^4$ respectively via [62],

$$\mathbb{B}(M1, m \to g) = \mathbb{B}_W(M1, m \to g) \cdot 1.790 \cdot \mu_N^2, \tag{4.11}$$
$$\mathbb{B}(E2, m \to g) = \mathbb{B}_W(E2, m \to g) \cdot 5.940 \cdot 10^{-2} \cdot A^{4/3} e^2(fm)^4, \tag{4.12}$$

where A is the number of nucleons, $\mu_N = e\hbar/(2m_p c)$ is the nuclear magneton and $fm = 10^{-15}m$. In atomic units $e = 1,\ \mu_N = 1/(2m_p c),\ m_p \approx 1836,\ c \approx 137,\ fm \approx 1.89 \times 10^{-5}$. The reduced nuclear matrix element is given by,

$$|\langle I_g||\mathcal{M}_{\lambda K}||I_m\rangle| = \sqrt{\frac{4\pi(2I_m+1)}{2K+1}\mathbb{B}(\lambda K, I_m \to I_g)}, \tag{4.13}$$

and the matrix element is then found with the use of the Wigner-Eckhart theorem [63],

$$|\langle I_g, M_g|\mathcal{M}_{\lambda K,q}|I_m, M_m\rangle| = \frac{(-1)^{I_m - M_m}}{\sqrt{2K+1}} C^{\,I_g \;\; I_m \;\; K}_{M_g - M_m \;\; q} \langle I_g||\mathcal{M}_{\lambda K}||I_m\rangle. \tag{4.14}$$

where I and M the total nuclear angular momentum and its projection quantum number respectively, $(I_g, I_m) = \left(\frac{5}{2}^+, \frac{3}{2}^+\right)$. Note also that,

$$\mathbb{B}_\uparrow^{\lambda K} = \frac{2I_m + 1}{2I_g + 1}\mathbb{B}_\downarrow^{\lambda K}, \tag{4.15}$$

where $\mathbb{B}_\uparrow^{\lambda K} = \mathbb{B}(\lambda K, g \to m)$, and $\mathbb{B}_\downarrow^{\lambda K} = \mathbb{B}(\lambda K, m \to g)$.

4.1.2 Electronic operators

The most general form of EB was presented in the last section with no strict requirements placed on the form of the nuclear and electronic wave functions. Current literature surrounding EB in Th ions [35–38, 82, 83] use the relativistic formalism of the electronic states. Here as a first approximation of EB in thorium-doped crystals, non-relativistic wave functions will be used. This is due to the increased complexity of generating wave functions in the crystal, which will be done using Density Functional Theory (more on this in Chapter 5). In this section we will outline the operators required for this non-relativistic treatment.

Let $\{|\beta\rangle\}$, be our set of non-relativistic electronic wave functions, where β represents all of the quantum numbers that define the state, apart from the spin[31]. These are only functions of spatial variables, thus each of these wave functions can define a spin up or down electron and therefore spin sub-states are degenerate. To introduce the spin $|\beta, m_s\rangle$ we define,

$$\psi_\beta^\uparrow(\boldsymbol{r}) = |\beta\rangle|\tfrac{1}{2}\rangle = |\beta\rangle \begin{pmatrix}1\\0\end{pmatrix}, \quad \psi_\beta^\downarrow(\boldsymbol{r}) = |\beta\rangle|-\tfrac{1}{2}\rangle = |\beta\rangle \begin{pmatrix}0\\1\end{pmatrix}. \tag{4.16}$$

The matrix elements of electronic operators will therefore be given below in the form $\langle m_s|O_{\lambda K,q}|m_s'\rangle$ where the spin component is solved. In this form they are ready to act directly on non-relativistic wave functions of spatial variables only.

[31] For example, in the case of eigenstates of orbital angular momentum we have $|\beta\rangle = |n, l, m_l\rangle$, or in the case of states defined only by energy $|\beta\rangle = |E\rangle$.

Electric dipole operator

$$\boldsymbol{D}_{E1} = -\boldsymbol{r} \tag{4.17}$$

The electric dipole operator does not act on spin, therefore we can easily write this in the spherical basis with the spin component solved giving,

$$\langle m_s|D_{E1,1}|m_s'\rangle = \frac{1}{\sqrt{2}}(x+iy)\delta_{m_s m_s'} = \frac{1}{\sqrt{2}}(r\sin\theta\cos\phi + ir\sin\theta\sin\phi)\delta_{m_s m_s'} \tag{4.18}$$

$$\langle m_s|D_{E1,-1}|m_s'\rangle = -\frac{1}{\sqrt{2}}(x-iy)\delta_{m_s m_s'} = -\frac{1}{\sqrt{2}}(r\sin\theta\cos\phi - ir\sin\theta\sin\phi)\delta_{m_s m_s'} \tag{4.19}$$

$$\langle m_s|D_{E1,0}|m_s'\rangle = -z\,\delta_{m_s m_s'} = -r\cos\theta\,\delta_{m_s m_s'}. \tag{4.20}$$

Magnetic dipole coupling operator

The Hamiltonian we are interested in describes the interaction of the nucleus with the electron shell. As such we can model this as an electron in the field created by the nucleus. In the case of M1 transitions, this is simply the hyperfine interaction Hamiltonian where the matrix element of the nuclear transition $\langle g|\mathcal{M}_{\lambda K,q}|m\rangle$ is non-diagonal allowing for nuclear transitions.

The relativistic treatment can be found in [84, p.137] starting with the interaction Hamiltonian,

$$H = e\phi - ec\boldsymbol{\alpha}\cdot\boldsymbol{A}, \tag{4.21}$$

where $\boldsymbol{A}$ and ϕ are the vector and scalar potentials respectively. A more general treatment can also be seen in [37, 38].

As discussed earlier, we will be making the non-relativistic approximation. To do so we begin with the relativistic Hamiltonian of a Dirac particle in an electromagnetic field. In Gaussian units we follow [85, p.124] and [86, p.171], see also [87, 88] [61, p.1025].

$$H = c\boldsymbol{\alpha}\cdot\left(\boldsymbol{p} + \tfrac{e}{c}\boldsymbol{A}\right) - e\phi + \beta m_e c^2, \tag{4.22}$$

where $\beta = \left(\begin{smallmatrix}\mathbb{1} & 0\\ 0 & -\mathbb{1}\end{smallmatrix}\right)$, $\boldsymbol{\alpha} = \left(\begin{smallmatrix}0 & \boldsymbol{\sigma}\\ \boldsymbol{\sigma} & 0\end{smallmatrix}\right)$, $\boldsymbol{\sigma} = (\sigma_x, \sigma_y, \sigma_z)$ are the Pauli matrices and $\boldsymbol{p}$ is the momentum operator. Acting on the relativistic wave function $\begin{pmatrix}\tilde{\psi}_L\\ \tilde{\psi}_S\end{pmatrix}$ where $\tilde{\psi}_L$ and $\tilde{\psi}_S$ are the large and small components we have,

$$i\hbar\frac{\partial}{\partial t}\begin{pmatrix}\tilde{\psi}_L\\ \tilde{\psi}_S\end{pmatrix} = c\boldsymbol{\alpha}\cdot\left(\boldsymbol{p} + \tfrac{e}{c}\boldsymbol{A}\right)\begin{pmatrix}\tilde{\psi}_L\\ \tilde{\psi}_S\end{pmatrix} - e\phi\begin{pmatrix}\tilde{\psi}_L\\ \tilde{\psi}_S\end{pmatrix} + \beta m_e c^2\begin{pmatrix}\tilde{\psi}_L\\ \tilde{\psi}_S\end{pmatrix},$$

now separating out the rest energy $\begin{pmatrix}\tilde{\psi}_L\\ \tilde{\psi}_S\end{pmatrix} = \begin{pmatrix}\psi_L\\ \psi_S\end{pmatrix}e^{-i(m_e c^2/\hbar)t}$ gives,

$$\begin{aligned} i\hbar\frac{\partial}{\partial t}\begin{pmatrix}\psi_L\\ \psi_S\end{pmatrix} &= c(\boldsymbol{\sigma}\cdot\boldsymbol{\Pi})\begin{pmatrix}\psi_S\\ \psi_L\end{pmatrix} - e\phi\begin{pmatrix}\psi_L\\ \psi_S\end{pmatrix} + m_e c^2\begin{pmatrix}\psi_L\\ -\psi_S\end{pmatrix} - m_e c^2\begin{pmatrix}\psi_L\\ \psi_S\end{pmatrix},\\ &= c(\boldsymbol{\sigma}\cdot\boldsymbol{\Pi})\begin{pmatrix}\psi_S\\ \psi_L\end{pmatrix} - e\phi\begin{pmatrix}\psi_L\\ \psi_S\end{pmatrix} - 2m_e c^2\begin{pmatrix}0\\ \psi_S\end{pmatrix}, \end{aligned}$$

where $\boldsymbol{\Pi} = \boldsymbol{p} + \frac{e}{c}\boldsymbol{A}$. Focusing on the small component equation,

$$\begin{aligned} i\hbar\frac{\partial}{\partial t}\psi_S &= c(\boldsymbol{\sigma}\cdot\boldsymbol{\Pi})\psi_L - e\phi\psi_S - 2m_e c^2\psi_S,\\ \psi_S &\overset{non-rel.}{=} \frac{\boldsymbol{\sigma}\cdot\boldsymbol{\Pi}}{2m_e c}\psi_L. \end{aligned}$$

In the non-relativistic approximation the kinetic energy and potential energy are small compared to the rest energy, $|e\phi\psi_S| \ll |m_e c^2\psi_S| \gg \left|i\hbar\frac{\partial}{\partial t}\psi_S\right|$ [85, p.124]. Then for the large component we have,

$$i\hbar\frac{\partial}{\partial t}\psi_L = \frac{(\boldsymbol{\sigma}\cdot\boldsymbol{\Pi})(\boldsymbol{\sigma}\cdot\boldsymbol{\Pi})}{2m_e}\psi_L - e\phi\psi_L,$$

and can write the non-relativistic Hamiltonian[32] as,

$$H \overset{non-rel.}{=} \frac{1}{2m_e}\left(\boldsymbol{p} + \tfrac{e}{c}\boldsymbol{A}\right)^2 + \frac{e\hbar}{2m_e c}\boldsymbol{\sigma}\cdot\boldsymbol{B} - e\phi. \tag{4.23}$$

[32] Known as the Pauli equation.

Considering now only the magnetic interaction, we drop the electric interaction term $e\phi$ to be covered later, and the kinetic energy term $\boldsymbol{p}^2/(2m_e)$ leaving,

$$\begin{aligned} H_{mag} =& \frac{e}{2m_e c}\left(\boldsymbol{p}\cdot\boldsymbol{A}+\boldsymbol{A}\cdot\boldsymbol{p}\right)+\frac{e\hbar}{2m_e c}\boldsymbol{\sigma}\cdot\boldsymbol{B}, \\ =& \frac{e}{m_e c}\frac{\boldsymbol{l}\cdot\boldsymbol{\mu}_I}{r^3}+\frac{e\hbar}{2m_e c}\boldsymbol{\sigma}\cdot\boldsymbol{B}, \end{aligned}$$

where the vector potential due to the nuclear magnetic dipole moment is $\boldsymbol{A}=\boldsymbol{\mu}_I\times\boldsymbol{r}/r^3$, the orbital angular momentum of the electron is $\boldsymbol{l}=\boldsymbol{r}\times\boldsymbol{p}=-i\hbar\boldsymbol{r}\times\boldsymbol{\nabla}$ and for first-order calculation we have neglected terms quadratic in $\boldsymbol{A}$ [86, p.171].

The magnetic field, $\boldsymbol{B}$, is due to the nuclei's magnetic dipole moment, given by [53, p.188]

$$\boldsymbol{B}(\boldsymbol{r})=\left[-\frac{\boldsymbol{\mu}_I}{r^3}+\frac{3\boldsymbol{r}(\boldsymbol{r}\cdot\boldsymbol{\mu}_I)}{r^5}+\frac{8\pi}{3}\boldsymbol{\mu}_I\delta(\boldsymbol{r})\right], \tag{4.24}$$

which results in the magnetic interaction Hamiltonian [86, p.171] [61, p.258],

$$\begin{aligned} H_{mag} &= \frac{2\mu_B}{\hbar}\left[\frac{\boldsymbol{l}\cdot\boldsymbol{\mu}_I}{r^3}+\boldsymbol{s}\cdot\boldsymbol{B}\right], \\ &= \frac{2\mu_B}{\hbar}\boldsymbol{\mu}_I\cdot\left[\frac{\boldsymbol{l}}{r^3}-\frac{\boldsymbol{s}}{r^3}+\frac{3\boldsymbol{r}(\boldsymbol{s}\cdot\boldsymbol{r})}{r^5}+\frac{8\pi}{3}\boldsymbol{s}\delta(\boldsymbol{r})\right], \end{aligned} \tag{4.25}$$

where $\boldsymbol{s}=\frac{\hbar}{2}\boldsymbol{\sigma}$, $\mu_B=e\hbar/2m_e c$. Writing the nuclear magnetic dipole moment in tensor notation $\boldsymbol{\mu}_I=\boldsymbol{\mathcal{M}}_{M1}$ allows us to deal with transitions, where the interaction matrix element is given by

$$\langle f,g|H_{mag}|m,i\rangle=\frac{2\mu_B}{\hbar}\langle g|\boldsymbol{\mathcal{M}}_{M1}|m\rangle\cdot\langle f|\left[\frac{\boldsymbol{l}}{r^3}-\frac{\boldsymbol{s}}{r^3}+\frac{3\boldsymbol{r}(\boldsymbol{s}\cdot\boldsymbol{r})}{r^5}+\frac{8\pi}{3}\boldsymbol{s}\delta(\boldsymbol{r})\right]|i\rangle. \tag{4.26}$$

The nuclear part was already discussed earlier, so we now concentrate on the electronic part,

$$\boldsymbol{\mathcal{T}}_{M1}=\frac{2\mu_B}{\hbar}\left[\frac{\boldsymbol{l}}{r^3}-\frac{\boldsymbol{s}}{r^3}+3\frac{\boldsymbol{r}(\boldsymbol{s}\cdot\boldsymbol{r})}{r^5}+\frac{8\pi}{3}\boldsymbol{s}\delta(\boldsymbol{r})\right]. \tag{4.27}$$

Converting to our units of choice, atomic units $\hbar=e=m_e=4\pi\varepsilon_0=1$ and $c\approx 137$, yields the final result

$$\boldsymbol{\mathcal{T}}_{M1}=\frac{1}{c}\left[\frac{\boldsymbol{l}}{r^3}-\frac{\boldsymbol{\sigma}}{2r^3}+3\frac{\boldsymbol{r}(\boldsymbol{\sigma}\cdot\boldsymbol{r})}{2r^5}+\frac{8\pi}{6}\boldsymbol{\sigma}\delta(\boldsymbol{r})\right]. \tag{4.28}$$

We then write the vector components in the spherical basis, see Appendix A.11. Starting with the orbital angular momentum,

$$\boldsymbol{l} = -i\boldsymbol{r}\times\boldsymbol{\nabla} \tag{4.29}$$

$$= -i\boldsymbol{r}\times\left(\hat{\boldsymbol{r}}\frac{\partial}{\partial r}+\frac{\hat{\boldsymbol{\theta}}}{r}\frac{\partial}{\partial\theta}+\frac{\hat{\boldsymbol{\phi}}}{r\sin\theta}\frac{\partial}{\partial\phi}\right) \tag{4.30}$$

$$= -i\left(\hat{\boldsymbol{\phi}}\frac{\partial}{\partial\theta}-\frac{\hat{\boldsymbol{\theta}}}{\sin\theta}\frac{\partial}{\partial\phi}\right) \tag{4.31}$$

$$l_x = \hat{\boldsymbol{x}}\cdot\boldsymbol{l}=i\left(\sin\phi\frac{\partial}{\partial\theta}+\cot\theta\cos\phi\frac{\partial}{\partial\phi}\right) \tag{4.32}$$

$$l_y = \hat{\boldsymbol{y}}\cdot\boldsymbol{l}=i\left(-\cos\phi\frac{\partial}{\partial\theta}+\cot\theta\sin\phi\frac{\partial}{\partial\phi}\right) \tag{4.33}$$

$$l_z = \hat{\boldsymbol{z}}\cdot\boldsymbol{l}=-i\frac{\partial}{\partial\phi} \tag{4.34}$$

we construct the spherical basis

$$l_+ = -\frac{1}{\sqrt{2}}(l_x+il_y)=-\frac{e^{i\phi}}{\sqrt{2}}\left(\frac{\partial}{\partial\theta}+i\cot\theta\frac{\partial}{\partial\phi}\right) \tag{4.35}$$

$$l_- = \frac{1}{\sqrt{2}}(l_x-il_y)=\frac{e^{-i\phi}}{\sqrt{2}}\left(-\frac{\partial}{\partial\theta}+i\cot\theta\frac{\partial}{\partial\phi}\right) \tag{4.36}$$

$$l_0 = l_z=-i\frac{\partial}{\partial\phi}. \tag{4.37}$$

Moving on now to the Pauli matrices $\boldsymbol{\sigma} = (\sigma_x, \sigma_y, \sigma_z)$

$$\sigma_x = \begin{pmatrix} 0 & 1 \\ 1 & 0 \end{pmatrix}, \qquad \langle m_s|\sigma_x|m_s'\rangle = 1 - \delta_{m_s,m_s'}, \tag{4.38}$$

$$\sigma_y = \begin{pmatrix} 0 & -i \\ i & 0 \end{pmatrix}, \qquad \langle m_s|\sigma_y|m_s'\rangle = 2im_s'(1 - \delta_{m_s,m_s'}), \tag{4.39}$$

$$\sigma_z = \begin{pmatrix} 1 & 0 \\ 0 & -1 \end{pmatrix}, \qquad \langle m_s|\sigma_z|m_s'\rangle = 2m_s'\delta_{m_s,m_s'}, \tag{4.40}$$

we convert them to spherical basis components giving,

$$\sigma_+ = -\frac{1}{\sqrt{2}}(\sigma_x + i\sigma_y) = -\begin{pmatrix} 0 & \sqrt{2} \\ 0 & 0 \end{pmatrix}, \qquad \langle m_s|\sigma_+|m_s'\rangle = -\sqrt{2}\delta_{m_s,m_s'+1}, \tag{4.41}$$

$$\sigma_- = \frac{1}{\sqrt{2}}(\sigma_x - i\sigma_y) = \begin{pmatrix} 0 & 0 \\ \sqrt{2} & 0 \end{pmatrix}, \qquad \langle m_s|\sigma_-|m_s'\rangle = \sqrt{2}\delta_{m_s,m_s'-1}, \tag{4.42}$$

$$\sigma_0 = \sigma_z = \begin{pmatrix} 1 & 0 \\ 0 & -1 \end{pmatrix}, \qquad \langle m_s|\sigma_0|m_s'\rangle = 2m_s'\delta_{m_s,m_s'}. \tag{4.43}$$

Considering the second term of $\boldsymbol{\mathcal{T}}_{M1}$,

$$3\frac{\boldsymbol{r}(\boldsymbol{\sigma}\cdot\boldsymbol{r})}{2r^5} = \frac{3\boldsymbol{r}}{2r^5}(\sigma_x x + \sigma_y y + \sigma_z z), \tag{4.44}$$

$$= \frac{3\boldsymbol{r}}{2r^4}(\sigma_x \sin\theta\cos\phi + \sigma_y \sin\theta\sin\phi + \sigma_z\cos\theta), \tag{4.45}$$

$$\langle m_s|3\frac{\boldsymbol{r}(\boldsymbol{\sigma}\cdot\boldsymbol{r})}{2r^5}|m_s'\rangle = \frac{3\boldsymbol{r}}{2r^4}\left[(1-\delta_{m_s,m_s'})e^{2m_s'i\phi}\sin\theta + 2m_s'\delta_{m_s,m_s'}\cos\theta\right]. \tag{4.46}$$

In a spherical basis $\boldsymbol{r} = (r_+, r_-, r_0)$ [61, p.203],

$$r_+ = -\frac{1}{\sqrt{2}}(x+iy) = -\frac{1}{\sqrt{2}}(r\sin\theta\cos\phi + ir\sin\theta\sin\phi), \tag{4.47}$$

$$r_- = \frac{1}{\sqrt{2}}(x-iy) = \frac{1}{\sqrt{2}}(r\sin\theta\cos\phi - ir\sin\theta\sin\phi), \tag{4.48}$$

$$r_0 = z = r\cos\theta. \tag{4.49}$$

The magnetic-dipole coupling-operator in the spherical basis that acts on the spatial components of wave functions is then,

$$\langle m_s|\mathcal{T}_{M1,+1}|m_s'\rangle = \frac{1}{c}\left[\frac{l_+\delta_{m_s,m_s'}}{r^3} + \frac{\delta_{m_s,m_s'+1}}{\sqrt{2}r^3} + \frac{3r_+}{2r^5}\langle m_s|\boldsymbol{\sigma}\cdot\boldsymbol{r}|m_s'\rangle - \frac{8\pi}{3\sqrt{2}}\delta_{m_s,m_s'+1}\delta(\boldsymbol{r})\right], \tag{4.50}$$

$$\langle m_s|\mathcal{T}_{M1,-1}|m_s'\rangle = \frac{1}{c}\left[\frac{l_-\delta_{m_s,m_s'}}{r^3} - \frac{\delta_{m_s,m_s'-1}}{\sqrt{2}r^3} + \frac{3r_-}{2r^5}\langle m_s|\boldsymbol{\sigma}\cdot\boldsymbol{r}|m_s'\rangle + \frac{8\pi}{3\sqrt{2}}\delta_{m_s,m_s'-1}\delta(\boldsymbol{r})\right], \tag{4.51}$$

$$\langle m_s|\mathcal{T}_{M1,0}|m_s'\rangle = \frac{1}{c}\left[\frac{l_0\delta_{m_s,m_s'}}{r^3} - \frac{m_s'\delta_{m_s,m_s'}}{r^3} + \frac{3r_0}{2r^5}\langle m_s|\boldsymbol{\sigma}\cdot\boldsymbol{r}|m_s'\rangle + \frac{8\pi m_s'}{3}\delta_{m_s,m_s'}\delta(\boldsymbol{r})\right]. \tag{4.52}$$

See Appendix A.12 for further details on the computation of these matrix elements.

Electric quadrupole coupling operator

The E2 transition operator is given by [89]

$$\mathcal{T}_{E2,q} = -\frac{1}{r^3}\sqrt{\frac{4\pi}{5}}Y_{2,q}(\theta,\phi) \tag{4.53}$$

$$\langle m_s|\mathcal{T}_{E2,q}|m_s'\rangle = -\frac{1}{r^3}\sqrt{\frac{4\pi}{5}}Y_{2,q}(\theta,\phi)\delta_{m_s m_s'} \tag{4.54}$$

where $q \in (-2,-1,0,1,2)$ and $Y_{2,q}$ ar the spherical harmonics given explicitly by,

$$Y_{2,-2}(\theta,\phi) = \frac{1}{4}\sqrt{\frac{15}{2\pi}}e^{-2i\phi}\sin^2\theta, \tag{4.55}$$

$$Y_{2,-1}(\theta,\phi) = \frac{1}{2}\sqrt{\frac{15}{2\pi}}e^{-i\phi}\sin\theta\cos\theta, \tag{4.56}$$

$$Y_{2,0}(\theta,\phi) = \frac{1}{4}\sqrt{\frac{5}{2\pi}}(3\cos^2\theta-1), \tag{4.57}$$

$$Y_{2,1}(\theta,\phi) = -\frac{1}{2}\sqrt{\frac{15}{2\pi}}e^{i\phi}\sin\theta\cos\theta, \tag{4.58}$$

$$Y_{2,2}(\theta,\phi) = \frac{1}{4}\sqrt{\frac{15}{2\pi}}e^{2i\phi}\sin^2\theta. \tag{4.59}$$

4.1.3 Order of computation

Now that we have an understanding of the EB rate equations as well as the operators involved we can discuss how the computation of rates is carried out. First, matrix elements are calculated for all operators involved in the process. Starting with the nuclear transition matrix elements, here only the reduced transition probabilities $\mathbb{B}_{\downarrow}$ are required. From these the nuclear transition matrix elements for decay $|\langle I_g M_g|\mathcal{M}_{\lambda K,q}|I_m M_m\rangle|$ and excitation $|\langle I_m M_m|\mathcal{M}_{\lambda K,q}|I_g M_g\rangle|$ are given directly with (4.14), and the result is a matrix of size $(2I_g+1)\times(2I_m+1)$ or $(2I_m+1)\times(2I_g+1)$ respectively, one element for each possible transition.

Using the set of single-component non-relativistic wave functions $\{|\beta\rangle\}$, the spin is introduced $|\beta, m_s\rangle$ using (4.16) , where operators have been given in the form $\langle m_s|O_{\lambda K,q}|m_s'\rangle$ in the above sections. The final form of the transition operators is thus obtained via,

$$\langle f|O_{\lambda K,q}|i\rangle = \langle \beta, m_s|O_{\lambda K,q}|\beta', m_s'\rangle = \int \psi_\beta^* \langle m_s|O_{\lambda K,q}|m_s'\rangle \psi_{\beta'} r^2 \sin\theta \,\mathrm{d}r\,\mathrm{d}\theta\,\mathrm{d}\phi. \tag{4.60}$$

For our purposes the entire matrix is usually needed. As such this generates matrices with dimension $2N\times 2N$ where there are $2N$ wave functions in the set

$$\{|\beta, m_s\rangle\} = \{|\beta_1, \tfrac{1}{2}\rangle, |\beta_1, -\tfrac{1}{2}\rangle, \ldots, |\beta_N, \tfrac{1}{2}\rangle, |\beta_N, -\tfrac{1}{2}\rangle\}. \tag{4.61}$$

For computational purposes, this is broken into real and imaginary components, considering the matrix element $\langle\psi|O|\phi\rangle$

$$\begin{aligned}\langle\psi|O|\phi\rangle = {} & \langle\Re\psi|\Re O|\Re\phi\rangle - \langle\Re\psi|\Im O|\Im\phi\rangle + \langle\Im\psi|\Re O|\Im\phi\rangle + \langle\Im\psi|\Im O|\Re\phi\rangle \\ & + i\left(\langle\Re\psi|\Re O|\Im\phi\rangle + \langle\Re\psi|\Im O|\Re\phi\rangle - \langle\Im\psi|\Re O|\Re\phi\rangle + \langle\Im\psi|\Im O|\Im\phi\rangle\right)\end{aligned} \tag{4.62}$$

where the operator and wave functions are complex. This is done for all electronic operators of interest. In our case this results in three matrices representing $D_{E1,q}$ where $q=\{1,0,-1\}$, three matrices for $T_{M1,q}$ where $q=\{1,0,-1\}$, and five matrices for $T_{E2,q}$ where $q=\{2,1,0,-1,-2\}$.

Generating these large matrices is the most computationally expensive part of the EB rate calculation. Once this is done all matrices can be saved and different EB processes can be calculated. This is done by first determining the bridge scheme one is interested in, and defining the set of initial and final states of the nucleus and electronic shell. From this information matrix elements of the effective bridge operator, (4.4) or (4.6) for the spontaneous decay or excitation process respectively, can be calculated and then the rate can be directly found via (4.3) and (4.5) respectively.

Chapter 5

EB in Thorium-doped crystals

In the last chapter, EB was discussed for a general system made up of a nucleus and surrounding electrons. In this work, we are interested in thorium-doped crystals and in the crystal environment we do not deal with electrons in atomic orbitals but rather energy bands. These are states of valence electrons in the crystals unit cell, i.e., electronic ground states and excited states such as those of the crystals conduction band. Some of these electronic states are localized tightly around thorium (resembling atomic orbitals) and others have their origin elsewhere in the crystal's unit cell or may not even have an origin. Furthermore, due to lack of rotational and reflection symmetry[33] the wave functions of electrons in the crystal environment are not necessarily eigenstates of either angular momentum or parity. They are only defined by their energy and hence the set of these wave functions is given by $\{|E_n\rangle\}$, where n denotes the level numbering. We therefore define nuclear decay via EB in the crystal as a process whereby the nucleus of interest decays by transfer of energy to a valence electron in the crystals units cell accompanied by the emission of a photon. In the present chapter we will first discuss calculation of electronic wave functions for thorium-doped crystals followed by the application of EB theory to the crystal environment.

Electronic wave functions in the crystal

The electronic wave functions used for this section were calculated by Martin Pimon, who works in the group of Peter Mohn at the Technische Universität Wien, using Density Functional Theory (DFT) within the Vienna Ab initio Simulation Package (VASP) for which they specialize [22, 90]. The specific method used to calculate the wave functions involved here is called the Projector Augmented Wave Method (PAW) described in [91] along with its implementation in VASP given in [92].

To gain a general understanding of DFT terminology without its many intricacies, we present a brief outline of the Kohn-Sham (KS) equations which lay at its core. Kohn and Sham in [93] introduced a self-consistent method to solve a system of non-interacting electrons with an effective potential which results in the correct electron density of the same system of interacting electrons. Following [94, p.142], the single electron KS equation[34] is given by

$$\left[-\frac{1}{2}\nabla^2 + v_{eff}(\boldsymbol{r})\right]\psi_n = E_n\psi_n, \tag{5.1}$$

where ψ_n and E_n are the N lowest single electron eigenstates and eigenvalues, and the wave functions are orthonormal

$$\int \psi_n^*(\boldsymbol{r})\psi_m(\boldsymbol{r})\,\mathrm{d}\boldsymbol{r} = \delta_{nm}. \tag{5.2}$$

The total electron density is given by

$$\rho(\boldsymbol{r}) = \sum_{n=1}^{N}\sum_{s}|\psi_n(\boldsymbol{r},s)|^2, \tag{5.3}$$

The KS effective potential is

$$v_{eff}(\boldsymbol{r}) = v(\boldsymbol{r}) + \frac{\delta J[\rho]}{\delta\rho(\boldsymbol{r})} + \frac{\delta E_{xc}[\rho]}{\delta\rho(\boldsymbol{r})} = v(\boldsymbol{r}) + \int\frac{\rho(\boldsymbol{r}')}{|\boldsymbol{r}-\boldsymbol{r}'|}\,\mathrm{d}\boldsymbol{r}' + v_{xc}(\boldsymbol{r}), \tag{5.4}$$

[33] Different from the case involving ions.

[34] Single electron Schrödinger equation with effective KS potential.

where $v(\boldsymbol{r})$ is the potential due to the nuclei as well as any externally applied potential, $J[\rho] = \frac{1}{2}\iint \frac{\rho(\boldsymbol{r})\rho(\boldsymbol{r}')}{|\boldsymbol{r}-\boldsymbol{r}'|}\,\mathrm{d}\boldsymbol{r}\,\mathrm{d}\boldsymbol{r}'$ is the classical electron-electron repulsion energy and $v_{xc}(\boldsymbol{r}) = \frac{\delta E_{xc}[\rho]}{\delta\rho(\boldsymbol{r})}$ the so-called exchange-correlation potential. The system is solved by giving an initial guess of $\rho(\boldsymbol{r})$ from which the effective potential can be found via (5.4). Inputting this in the KS equation (5.1) gives a new prediction of the single electron wave functions which in turn give the new density using (5.3). This iterative nature depicted in Figure 5.1 is what makes the calculation self-consistent.

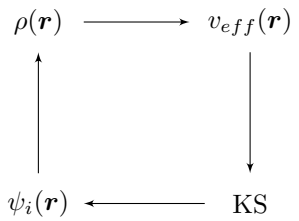

Figure 5.1: Self-consistent method via Kohn-Sham equations. Given an initial guess of $\rho(\boldsymbol{r})$ the effective potential can be found via (5.4), inputting this in the KE equation (5.1) gives a new prediction of the single electron wave functions from which the new density is found using (5.3).

Once the predicted density and therefore energy converges within the set bounds the calculation is finished. The total energy of the system is written as

$$E[\rho] = T_s[\rho] + J[\rho] + E_{xc}[\rho] + \int \rho(\boldsymbol{r})v(\boldsymbol{r})\,\mathrm{d}\boldsymbol{r} \tag{5.5}$$

where

$$T_s[\rho] = \sum_{n=1}^{N}\sum_{s}\psi_n^*(\boldsymbol{r},s)\left(\frac{1}{2}\nabla^2\right)\psi_n(\boldsymbol{r},s), \tag{5.6}$$

is the KS kinetic energy and $E_{xc}[\rho]$ is the exchange-correlation functional. It is in the definition of the exchange-correlation functional where all the details of DFT are hidden. This is because to solve the KS equations, $E_{xc}[\rho]$ is the only unknown and therefore the only approximation. The mathematical form $E_{xc}[\rho]$ remains an intense field of research since the KS method was first proposed, and the resultant research is some of the most cited work in physics today [95].

For further calculations using these wave functions, it is important that they are (1) numerically orthonormal and (2) the energies of the wave functions are properly calculated. Unfortunately, in our case these two properties are not an easy task computationally. Orthonormality of the generated wave functions is a required condition in PWA and thus will be numerically orthonormal provided there is sufficient sampling in the three-dimensional space for which the wave functions are defined, more on this in Chapter 7.

Unfortunately, it is well known [8] that DFT methods do not accurately predict the energy of the calculated states. Our crystal of interest CaF_2 has an experimentally measured band gap in the region of $11 - 12$ eV [64–66] which we approximate as 11.5 eV. As a result, the energies predicted by DFT and the PAW method are scaled to match this band gap value at 11.5 eV. In the case of the two exchange-correlation functionals PBE (Perdew-Burke-Ernzerhof) [96] and HSE (Heyd-Scuseria-Ernzerhof) [97] used here, all energies are scaled by a multiplicative factor of 1.54 and 1.18 respectively. This is the simplest method of scaling and the only one available to us without further experimental measurements.

Calculations suggest that doping thorium into CaF_2 results in localized thorium states, called color-center states, within the band gap of the crystal [8, 22]. The term color-center is given to a wide range of impurities in crystals, both natural and laser induced. For crystals these impurities can act to provide an otherwise transparent crystal with "color" by absorbing light in a given wavelength range [23]. We can view doping thorium into CaF_2 as the introduction of defects and as such will refer to it as a color-center [8, 24]. At this time, there are no experimental energy measurements of the color-center states in ^{229}Th:CaF_2. Therefore, it is unclear if the energy of thorium states sitting within the band-gap scale linearly with all other states. This is however the simplest option and its consequences will be discussed further in Section 6.4.

The unit cell chosen has 66 fluorine, 31 calcium and a single thorium nucleus, where periodic boundary conditions are applied to the unit cell. The unit cell has approximate dimensions of $(10\,\text{Å})^3$ which corresponds to a dopant density of $N = 10^{-3}\ \text{Å}^{-3} = 10^{21}\ \text{cm}^{-3}$. This concentration

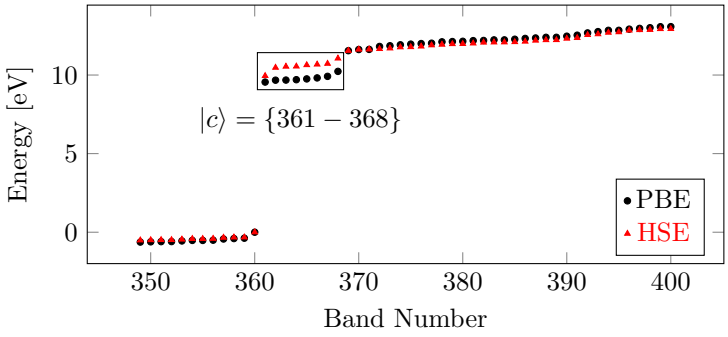

Figure 5.2: Energy of single electron states calculated using PBE and HSE functionals respectively. PBE and HSE energies are scaled by a multiplicative factor of 1.54 and 1.18 respectively, to match the experimentally determined CaF_2 band gap of 11.5 eV. color-center states $|c\rangle$ corresponding to band numbers $\{361 - 368\}$ are circled.

is larger than the expected experimental densities in the range of $10^{16} - 10^{18}\,\mathrm{cm}^{-3}$. This size was chosen to decrease computation times. The current calculation uses 98 nuclei. To get to a dopant density to $10^{16}\,\mathrm{cm}^{-3}$ we would require $\approx 9.8 \times 10^6$ nuclei which is not computationally feasible. Even still, calculations using several hundred nuclei can be an aim for future work.

We can divide the states of interest into three groups, depicted in Figure 5.3. The first being electronic ground states of the valence electrons in the unit cell of which there are 360, denoted $|o\rangle = \{1, \ldots, 360\}$. State 360 is the highest occupied level in the ground state also called the Fermi edge which is taken as 0 eV. Each energy state is spin-degenerate, thus state 360 is made up of two levels $|360\rangle \rightarrow |360\rangle|m_s\rangle \rightarrow |360^{\uparrow,\downarrow}\rangle$. Then there are the localized excited thorium color-center states of which there are eight, denoted $|c\rangle = \{361, \ldots, 368\}$, and finally there are conduction band states which begin at band 369 and increase in energy and decrease in energy spacing until the continuum, denoted $|b\rangle = \{369, \ldots\}$. Each of these states are spin-degenerate.

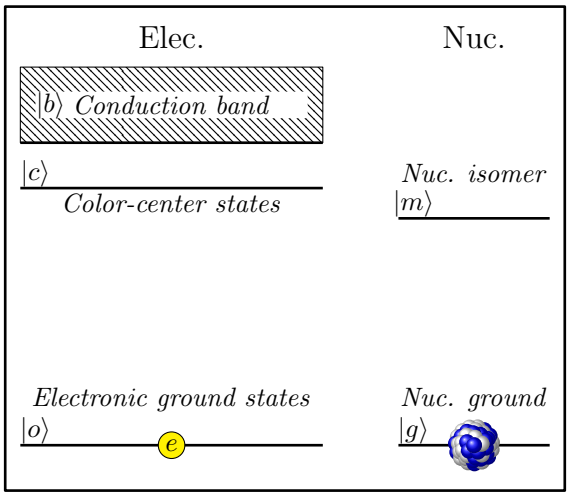

Figure 5.3: Fixed notation for the nuclear and electronic levels. The ground and isomeric states of the nucleus are $|g\rangle$ and $|m\rangle$ respectively. The electronic ground states are given by $|o\rangle$, electronic color-center states within the band-gap of the crystal by $|c\rangle$ and the conduction band shown by the slashed box by $|b\rangle$.

The predicted energies of each level depend on the functional used, however as stated above are scaled to match the experimental band gap of CaF_2. Once scaled, each functional should agree for us to be confident in the calculated energies. The scaled energies of the two methods are shown in Figure 5.2 where the eight color-center states denoted $|c\rangle$ are circled and correspond to bands $361 - 368$. The ground and conduction band states differ on the order of 0.1 eV for the bands plotted, where as the color-center states differ on the order of 1 eV. PBE color-center is at an average energy of 9.9 eV, or 1.6 eV above the isomer, and the HSE color-center is at an average energy of 10.5 eV, or 2.2 eV above the isomer. The energy width of the PBE and HSE color-centers are 0.6 eV and 1.1 eV respectively. As such we cannot be confident in the location of

the color-center states until further theoretical and experimental work is carried out.

The electron densities of the color-center states which are localized around the thorium nucleus are seen in Figure 5.4. Electron density of color-center wave functions are labeled 361 → 368 corresponding to increasing energy and the band numbering seen in Figure 5.2. Each image is shown at the same magnification, and corresponding PBE and HSE wave functions, denoted by "↔", are shown from the same viewpoint. Moving down the column the viewpoint changes. All functions were individually scaled to unity and so do not share the same max and min values. These images are intended to give an qualitative idea of the spatial structure. In the case of PBE functions 364 and 367, two different scalings where used to demonstrate the less obvious shape. The right most image is scaled to unity and displays the highest density sections. In the left most image a cutoff value was chosen such that the high density sections did not dominate the image and the lower density structure could be seen. PBE functions are matched with the closest corresponding HSE function and the pair are shown from the same viewpoint. There are some visual similarities to f-type atomic orbitals, however skewed by the crystal environment. Visually comparing the color-center electron density calculated using the two functionals shows some clear similarities, although there are no exact matches and the ordering in energy is not the same. Further investigation of these and other functionals must carried out to gain a better understanding of the color-center states. All calculations of bridge processes will strongly depend on the energy of the states involved and the form of the wave functions as seen in equations (4.3)-(4.6) . Based on the above it should be clear that the values of rates given here serve to demonstrate the feasibility of the EB schemes discussed in the following sections. More accurate rates can be calculated pending further experimental and theoretical investigation.

Application to the Electronic Bridge

Now that we have an understanding of the form of the wave functions we will be using we can adjust our mathematical view of EB to the crystal environment. Recall that our electronic wave functions are not eigenstates of either angular momentum or parity. Furthermore, in the crystal environment we will not be targeting a specific transition but rather an averaged transition between sets of non-degenerate electronic levels[35]. With this in mind we can rewrite equations (4.3) and (4.5) as follows[36]

$$\Gamma^{sp}_{EB}(g,f;m,i) = \frac{4}{3}\frac{1}{N_m N_i}\sum_{\substack{m,g,\\ i,f,q}}\left(\frac{\omega_N-\omega_{fi}}{c}\right)^3 |\langle g,f|\widetilde{D}_{E1,q}|m,i\rangle|^2, \tag{5.9}$$

where N_m and N_i are the number of initial nuclear and electronic states in the sets $\{|m\rangle\}$ and $\{|i\rangle\}$ respectively that take part in the process. Each set of electronic states in the crystal is not degenerate, therefore the emitted photon energy is not a constant. This is why the emitted photon energy ω_p has been moved within the summation. Similarly, for spontaneous excitation of the nucleus via EB

$$\Gamma^{sp}_{EB}(m,f;g,i) = \frac{4}{3}\frac{1}{N_g N_i}\sum_{\substack{m,g,\\ i,f,q}}\left(\frac{\omega_{if}-\omega_N}{c}\right)^3 |\langle m,f|\widetilde{D}_{E1,q}|g,i\rangle|^2. \tag{5.10}$$

The effective electric dipole operators are still given by (4.4) and (4.6) respectively, where all operators outlined in the last chapter apply to the crystal as well with no modification. In the context of the thorium-doped crystals, the intermediate summations seen in (4.4) and (4.6) are once again over all unoccupied states. This includes the ground, color-center, conduction band

[35]Note that although these wave function sets are non-degenerate, the energy spacing between levels in a set is smaller than the total energy width of the set which will be $\lesssim 0.5$ eV.

[36]The bridge rates studied here are that of the effective E1 bridge operator. One could also construct an effective M1 bridge written here for nuclear decay in the crystal [81, p.225],

$$\Gamma^{sp}_{EB}(g,f;m,i) = \frac{1}{3c^5}\frac{1}{N_m N_i}\sum_{\substack{m,g,\\ i,f,q}}(\omega_N-\omega_{fi})^3|\langle g,f|\widetilde{M}_{M1,q}|m,i\rangle|^2, \tag{5.7}$$

$$\langle g,f|\widetilde{\boldsymbol{M}}_{M1}|m,i\rangle = \sum_{\lambda K,q}(-1)^q\left[\sum_n\frac{\langle f|\boldsymbol{M}_{M1}|n\rangle\langle n|\mathcal{T}_{\lambda K,q}|i\rangle}{\omega_{in}+\omega_N}+\sum_k\frac{\langle f|\mathcal{T}_{\lambda K,q}|k\rangle\langle k|\boldsymbol{M}_{M1}|i\rangle}{\omega_{fk}-\omega_N}\right]\langle g|\mathcal{M}_{\lambda K,-q}|m\rangle, \tag{5.8}$$

where $\boldsymbol{M}_{M1}=\boldsymbol{l}+2\boldsymbol{s}$ is the the is the magnetic dipole operator with $\boldsymbol{l}=-\boldsymbol{r}\times\boldsymbol{\nabla}$ the orbital angular momentum operator and $\boldsymbol{s}$ the spin operator. This rate is hampered by the extra factor $1/c^2$ and is thus assumed negligible when compared to the E1 rate.

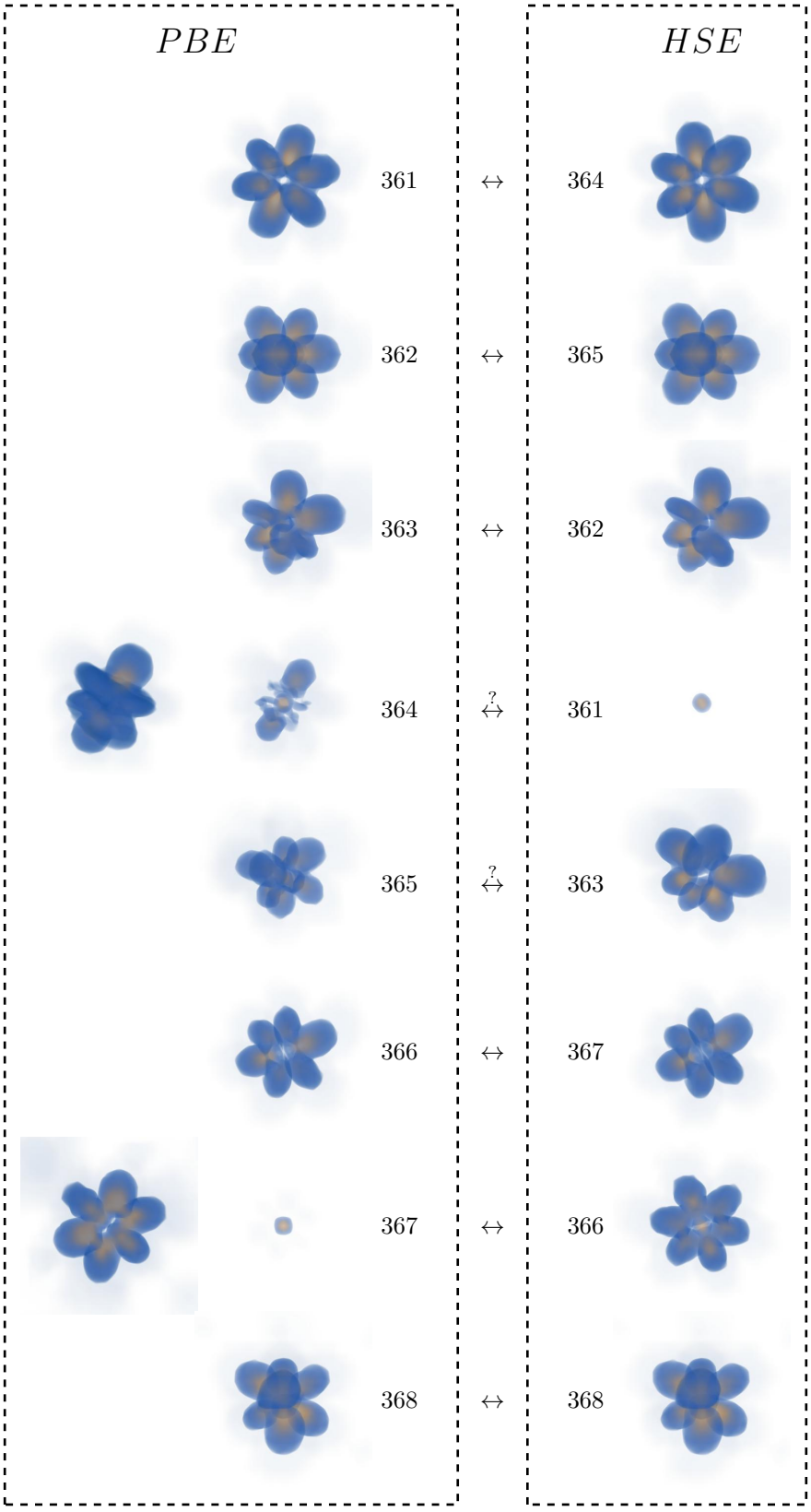

Figure 5.4: Electron density of color-center wave functions labeled 361 → 368 corresponding to increasing energy. Each image is shown at the same magnification but differing viewpoints to show the structure more clearly. PBE functions are matched with the closest corresponding HSE function and viewed from the same location. The "?" stands for cases where identification is not clear.

and unbound free states. The number states included in these intermediate summations must be increased until the rate converges.

Lastly, because the emitted photon energy is not a constant, the laser photons required for stimulated emission and absorption processes do not have an individual energy but rather the laser used must have a linewidth that overlaps the required energy range. The linewidth required will depend on the total energy width of the levels in the initial and final sets of electronic states $\{|i\rangle\}$ and $\{|f\rangle\}$ respectively. Of course if a narrower linewidth is used only a fraction of the electronic levels will take part in the stimulated or driven processes. There is thus an interplay between broadband excitation addressing more levels with less power per level, and narrowband excitation exciting a specific level with large power. This will be discussed further in the following sections.

Chapter 6

Excitation of the nuclear isomer

There are a variety of excitation schemes that one can investigate depending on the lasers/radiation sources available as well as the electronic and nuclear level structure in question. Before discussing these options, recall the notation for the nuclear and electronic levels is shown in Figure 5.3. The set of ground and isomeric states of the nucleus are given by $\{|g\rangle\}$ and $\{|m\rangle\}$ respectively. The electronic ground states of valence electrons are given by $\{|o\rangle\}$ the electronic color-center states within the band-gap of the crystal $\{|c\rangle\}$ and the conduction band levels $\{|b\rangle\}$. Notation introduced earlier will also be used such as $|i\rangle$ for initial $|f\rangle$ for final and $|v\rangle$ for virtual electronic states, however the corresponding states change depending on the scheme of interest. Note that each of these states is actually made up of a cluster of states as shown in the Chapter 5. In the case of the nuclear states we assume that all $(2I+1)$ magnetic sub-states are degenerate as the quadrupole splitting, of the order 10^{-6} eV, is far less than the energy difference of the electronic levels considered. The spin sub-states, i.e., spin up and spin down, of the electronic states that make up the color-center $|c\rangle$, ground state $|o\rangle$ and conduction band $|b\rangle$ are degenerate.

In the following sections we will discuss first the direct excitation rate of the nuclear isomeric state and color-center states independently. These values will then be used to compare with rates achieved using a variety of EB schemes. In addition to calculation of excitation rates, we also discuss the steady state occupation probability of the isomeric state as a rough measure of how successful the excitation scheme is.

6.1 Direct photoexcitation

Before considering transition rates due to EB processes, it is helpful to consider the direct excitation rates of (1) the nucleus and (2) electron shell independently. These will be considered here first, to be compared with the EB process in the following pages.

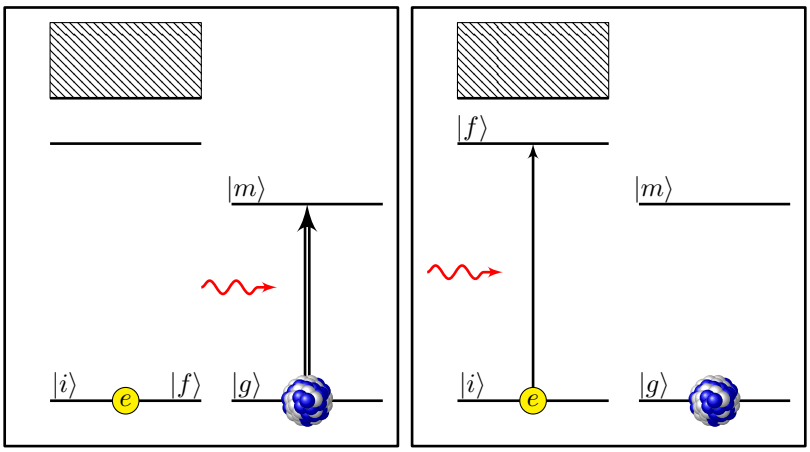

Figure 6.1: Direct photoexcitation of the nuclear isomer (Left) and electronic color-center (Right) states respectively. Here $|i\rangle$ is the initial state of the electron on the Fermi edge, $|f\rangle$ the final electronic state which is equal to $|i\rangle$ in the first case and the color-center state in the second case. Higher slashed states are that of the conduction band. $|g\rangle$ is the ground state of the thorium nucleus, and $|m\rangle$ the nuclear isomeric state.

(1) **The direct photoexcitation rate of the isomer** can be found by considering its spontaneous radiative decay rate, $\Gamma^{sp}_\gamma(g;m) \approx 10^{-4}$ s^{-1}. This rate considers no interaction with electrons in the shell. To consider the driven inverse process, i.e., excitation, we make use of the equation (4.8)

$$\Gamma^{a}_\gamma(m;g) = \Gamma^{sp}_\gamma(g;m) F_\omega P_\omega \delta(g;m), \tag{6.1}$$

where $\delta(g;m) = (2I_m+1)/(2I_g+1) = 2/3$ is the ratio of degeneracy of the initial and final states for the $\Gamma^{sp}_\gamma(g;m)$ decay process. The required photon energy $E_\omega = 8.3$ eV is that of the isomeric state. Thus, all elements of this equation are given except that of the power of the excitation source.

From here we can write the steady state occupation probability. This is the same as the density matrix treatment used for NFS where ρ_a corresponds to ρ_{aa}, i.e. the diagonal elements of the density matrix in the notation used in Part I. of the isomeric state if driven directly with photons of matching energy. Excitation, spontaneous emission and stimulated emission are considered,

$$\dot{\rho}_m = \rho_g \Gamma^{a}_\gamma(m;g) - \rho_m(\Gamma^{sp}_\gamma(g;m) + \Gamma^{st}_\gamma(g;m)) \tag{6.2}$$

where $\rho_g = 1 - \rho_m$. Taking the steady state solution $\dot{\rho}_m = 0$,

$$\rho_m = \frac{\Gamma^{a}_\gamma(m;g)}{\Gamma^{sp}_\gamma(g;m) + \Gamma^{st}_\gamma(g;m) + \Gamma^{a}_\gamma(m;g)} = \frac{F_\omega P_\omega \delta(g;m)}{1 + F_\omega P_\omega [\delta(g;m)+1]}. \tag{6.3}$$

Thus for large power P_ω the occupation probability of the isomeric state can be as high as $\rho_m \approx 2/5$.

The experimental group working on ^{229}Th:CaF$_2$ is lead by Thorsten Schumm at the Technische Universitt Wien. For excitation in the crystal environment Schumm's group currently uses a broad band VUV lamp described in [10] with $N \approx 3$ photons/s/Hz, a focus of $f = 0.5$ mm^2 which gives $P_\omega = NE_\omega/f \approx 10^{-11}$ W/(m^2 Hz) and a FWHM linewidth of ≈ 0.5 eV. This gives a direct excitation rate of

$$\Gamma^{a}_\gamma(m;g) \approx 4 \times 10^{-11}\,\mathrm{s}^{-1}, \tag{6.4}$$

and a steady state isomeric occupation probability of

$$\rho_m \approx 4 \times 10^{-7}, \tag{6.5}$$

which could be reached in $\tau \approx \rho_m/\Gamma^{a}_\gamma(m;g) = 10^4$ s^{-1}.

(2) **The direct photoexcitation rate of the color-center** states can be calculated in a two step process. First, the spontaneous decay rate of the color-center states to ground states is calculated using the equation [98, p.300] [84, p.171],

$$\Gamma^{sp}_{E1}(o;c) = \frac{4}{3}\frac{1}{N_c}\sum_{i,f,q}\left(\frac{\omega_{if}}{c}\right)^3 |\langle o_f|D_{E1,q}|c_i\rangle|^2, \tag{6.6}$$

where the spontaneous decay is approximated by transition via the E1 channel. Here $\omega_{if} = \omega_{c_i} - \omega_{o_f}$ is the emitted photon energy given by the difference in energy of the initial $|c_i\rangle$ and final $|o_f\rangle$ states, N_c is the number of initial states $|c_i\rangle$ in the decay process, and $D_{E1,q}$ is the electric dipole operator, not to be confused with the effective electric dipole operator as used for the bridge calculation. Note that ω_{if} is not fixed here due to the color-center and electronic ground states not being degenerate in energy. For the reverse process, i.e. excitation, ω_{if} will be the photon energy required. We assume here that the laser/excitation source used to populate the color-center overlaps the entire color-center, i.e. the 0.5 eV lamp outlined above. In this case, we do not know which level the electron is excited to. As such in the decay process we average over all possible color-center states, seen by the $1/N_c$ in (6.6).

A plot of the decay rate from the complete set of color-center states $\{|c\rangle\}$ to a individual electronic ground state $|o_f\rangle$ is shown in Figure 6.2 for both HSE and PBE wave functions. The energy of the states differ between PBE and HSE calculations. An equal number of ground states were chosen in both cases to investigate. The energy of the ground states ranged from $\{0 \to -0.63\}$ eV in the case of PBE and $\{0 \to -0.51\}$ eV for HSE. Ground

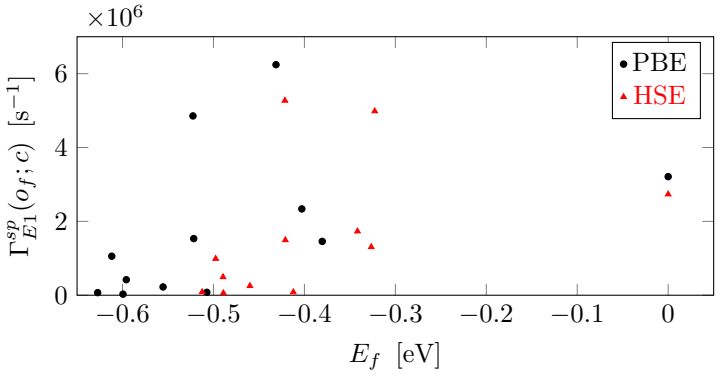

Figure 6.2: Spontaneous decay rate of the color-center states $|c\rangle$ to individual ground states $|o_f\rangle$ at energies E_f.

states up to ≈ 0.5 eV below the Fermi edge were first considered due to the linewidth of the lamp currently used in the group of Schumm. Spontaneous decay rates to these states ranged from $\Gamma^{sp}_{E1}(o_f;c) = \{0.2 \to 6.2 \times 10^6\}$ s^{-1}.

The rate of the inverse process i.e., the excitation $\Gamma^{a}_{E1}(c;o)$ depicted in Figure 6.1, is calculated using (4.8) where the power of the laser is required and $\delta(o;c) = N_c/N_o$. As we are only considering a single electron transition, at any given moment only one of the electronic ground states is excited to the color-center, and all other ground states are occupied. The rate of excitation from a given state is proportional to the decay rate to that state, as seen in (4.8). Therefore, the dominant contribution to the excitation rate from the set of ground states to the set of color-center states $\{|o\rangle\} \to \{|c\rangle\}$ will come from the ground state with largest rate shown in Figure 6.2, provided the laser/excitation source overlaps the transition. The largest decay rates presented in Figure 6.2 are all of the same order, thus the average excitation rate from an individual ground state will be of the same order as well. Hence, we approximate the EB rates in the following by considering only one of these energy levels. For this, we will consider the highest occupied the spin-degenerate ground state level at the Fermi edge, 0 eV[37].

With the average energy of the color-center states as $E_\omega = \bar{E}_{co} \approx 10$ eV, we can estimate the excitation rate for Schumm's above outlined VUV lamp,

$$\Gamma^{a}_{E1}(c;o) = \Gamma^{sp}_{E1}(o;c) F_\omega P_\omega \delta(o;c) \approx 7\,\mathrm{s}^{-1}, \tag{6.7}$$

where $\delta(o;c) = 8$ as there are eight spin-degenerate color-center states and only a single spin-degenerate ground state.

6.2 A: EB starting in the electronic ground state

In the following we consider our first EB scheme labeled A and depicted in Figure 6.3. The color-center states are assumed to be higher in energy than the isomer. With both the nucleus and the electronic shell in their respective ground states, a laser of energy $\omega_p = \omega_N - \omega_{fi}$ is used to drive the EB process. The EB process can be thought of as the electron undergoing a transition from the ground state to a virtual state $|v\rangle$, with the input of an laser photon at the energy of the nuclear transition, and upon its decay back to the electronic ground state passes the energy to the nucleus, causing its excitation to the isomeric state. In this scheme, both the initial and final electronic states belong to the set of electronic ground state levels $\{|o\rangle\}$. This set is approximated by the spin-degenerate state at 0 eV, as discussed earlier. In this approximation, $\omega_{fi} = 0$, however if other ground states are used this is not necessarily true.

To calculate the excitation rate of the isomer we first determine the rate of the inverse process, which is found by reversing process seen in Figure 6.3. This is achieved by swapping the initial and final state of both the electron and nucleus, and reversing the direction of all arrows including that of the photon (i.e. the photon is emitted not absorbed). The inverse is then a spontaneous

[37] If lower ground state levels were excited instead, a more rigorous treatment of the dynamics of decay between levels within the ground state would be required. This complication is unnecessary in the first approximation as spontaneous decay from the color-center to the largest contributing individual ground states all yield rates of the order 10^6 s^{-1}.

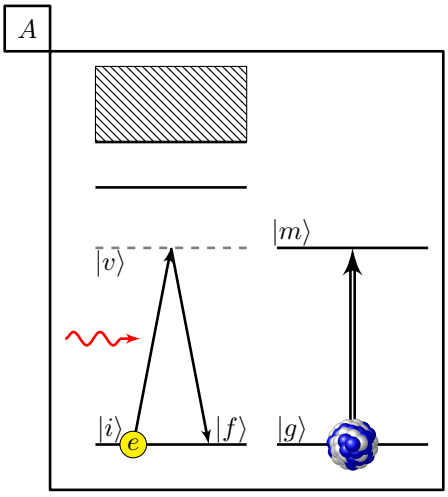

Figure 6.3: EB scheme A: excitation of the nuclear isomer via EB where the electronic shell, initially in the ground state, first absorbs the incoming laser photon of energy $\omega_p = \omega_N - \omega_{fi}$, and then passes the energy to the nucleus with transition back to the ground state.

decay process which is calculated using (5.9) where $N_m N_i = (2I_m + 1)N_o$ written here as,

$$\Gamma_A^{sp}(g, o; m, o) = \frac{4}{3}\frac{1}{(2I_m+1)N_o} \sum_{\substack{M_m, M_g, \\ i,f,q}} \left(\frac{\omega_N - \omega_{fi}}{c}\right)^3 |\langle I_g, M_g, o_f | \widetilde{D}_{E1,q} | I_m, M_m, o_i \rangle|^2, \tag{6.8}$$

where all notation is presented in the theory section with the exception of $N_o = 2$ which is the number of initial electronic ground states $|o_i\rangle$ used[38].

The effective electric dipole operator is calculated using (4.4), where the two summations correspond to the two Feynman diagrams shown in Figure 4.1. The dominant contribution in this case is due to the first summation corresponding the the nuclear isomer decaying first to its ground state and then transferring a photon to the electronic shell which is subsequently excited to an intermediate state (virtual) which decays emitting a photon out of the system. This first summation is pictorially represented by the reverse of Figure 6.3. The second summation does not contribute as it requires that first the electron undergoes a decay emitting a photon from the system and then the nucleus decays bring the electron back up to the Fermi edge. This process is blocked as all levels below the Fermi edge are assumed to be filled, thus the initial decay of the electron is not allowed.

The EB rate considering electronic ground states $|o\rangle \in \{360^{\uparrow,\downarrow}\}$ and summing over intermediate states $|n\rangle \in \{360^{\uparrow,\downarrow}, \ldots, 407^{\uparrow,\downarrow}\}$ results in $\Gamma_A^{sp}(g, o; m, o) = \mathcal{O}(10^{-8})$ s^{-1}. This rate does not exceed the radiative decay $\Gamma_\gamma^{sp}(g; m)$, and thus is only a correction to the direct radiative decay or excitation process,

$$\frac{\Gamma_A^a(m, o; g, o)}{\Gamma_\gamma^a(m; g)} = \frac{\Gamma_A^{sp}(g, o; m, o)}{\Gamma_\gamma^{sp}(g; m)} \approx \frac{10^{-8}}{10^{-4}} = 10^{-4}. \tag{6.9}$$

The decay rate of the spontaneous process and laser excitation rate are related by (4.8).

6.3 B: EB starting from the color-center with energy greater than the isomer

The second EB scheme B is depicted in Figure 6.4 and is equivalent to moving from left to right in the Feynman diagrams in Figure 4.1 where m and g are swapped. The initial state of the electron is in the color-center which is assumed higher in energy than the isomeric state. Upon its decay it excites the isomer and emits a photon with energy equal to the difference in energy between the color-center and the isomer. The electron can decay emitting the photon either before or after exciting the nucleus, see once again Figure 4.1.

[38] Single energy, spin-degenerate ground state.

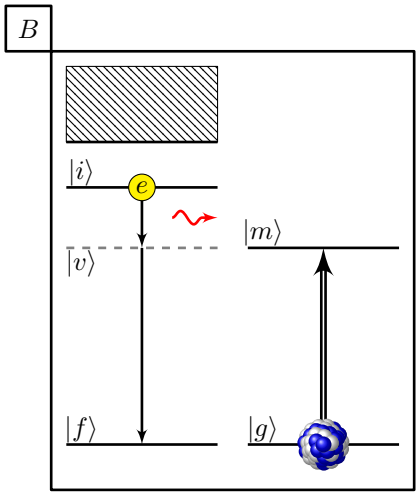

Figure 6.4: EB scheme B: excitation of the nuclear isomer via EB where the electronic shell, initially in the excited color-center, decays passing the energy to the nucleus as well as emitting a real photon of energy $\omega_p = \omega_{if} - \omega_N$. Note the electronic state can decay in two ways, first emitting the photon and then exciting the nucleus, or vice versa. Both options contribute to the rate. Here only the first is depicted.

This is not a laser driven process[39] and therefore the rate of excitation of the isomer assuming the color-center is populated is given by (5.10) where the averaging factor $N_g N_i = (2I_g + 1)N_c$ giving,

$$\Gamma_B^{sp}(m, o; g, c) = \frac{4}{3}\frac{1}{(2I_g+1)N_c} \sum_{\substack{M_m, M_g, \\ c_i, o_f, q}} \left(\frac{\omega_{if} - \omega_N}{c}\right)^3 |\langle I_m, M_m, o_f | \widetilde{D}_{E1,q} | I_g, M_g, c_i \rangle|^2, \tag{6.10}$$

with the effective electric dipole matrix elements given by (4.6).

The EB rate considering electronic ground states $|o\rangle \in \{360^{\uparrow,\downarrow}\}$, color-center states $|c\rangle \in \{361^{\uparrow,\downarrow}, \ldots, 368^{\uparrow,\downarrow}\}$ and summing over intermediate states $|n\rangle \in \{360^{\uparrow,\downarrow}, \ldots, 407^{\uparrow,\downarrow}\}$ results in $\Gamma_B^{sp}(m, o; g, c) = \mathcal{O}(10^{-8})$ s^{-1}. This assumes that the color-center is populated. As such to obtain the true reaction rate we must multiply by the occupation probability of the color-center states. This can be see easily when writing the rate of change of the occupation probability of the nuclear isomeric state $\dot{\rho}_m$ as a master equation

$$\dot{\rho}_m = \rho_g \rho_c \Gamma_B^{sp}(m, o; g, c) + \ldots - \rho_m \Gamma_\gamma^{sp}(g; m) - \ldots \tag{6.11}$$

The ellipsis $(\ldots)$ in the master equation are meant to include all other processes that change the occupation probability of the isomeric state. It can also be assumed that the occupation probability of the nuclear ground state $\rho_g = 1 - \rho_m \approx 1$ as the nuclei are for the most part naturally in the ground state when the crystal is created. Here we can see that the rate of change of isomer population depends on the $\rho_c \Gamma_B^{sp}(m, o; g, c)$, i.e., the population of the color-center states multiplied by the rate of the process B starting in the color-center states.

A similar master equation can be written for the color-center states occupation probability. The color-center is populated by excitation from the ground state via photon absorption. Assuming continuous pumping of the color-center states we can write,

$$\dot{\rho}_c = \rho_o \Gamma_{E1}^a(c; o) - \rho_c \left[\Gamma_{E1}^{sp}(o; c) + \Gamma_{E1}^{st}(o; c)\right] \tag{6.12}$$

where E1 absorption, spontaneous E1 decay and stimulated E1 decay are taken into account. Taking the steady state solution $\dot{\rho}_c = 0$ gives the approximate occupation probability of the color-center,

$$\rho_c = \frac{\Gamma_{E1}^a(c; o)}{\Gamma_{E1}^{sp}(o; c) + \Gamma_{E1}^{st}(o; c) + \Gamma_{E1}^a(c; o)} = \frac{F_{co} P_{co} \delta(o; c)}{1 + F_{co} P_{co}[1 + \delta(o; c)]}, \tag{6.13}$$

where $\rho_o = 1 - \rho_c$, E_{co} is the difference in energy between the color-center $|c\rangle$ and the electronic ground $|o\rangle$, P_{co} the power of the photon source at energy E_{co}, and $\delta(o; c) = N_c/N_o$ is the ratio of

[39] Besides the initial excitation of the electron to the color-center.

number of states in each set. Considering again only one ground state $\delta(o;c) = 8$, we can see that for the low powered VUV lamp, where $1 + F_{co}P_{co}[1 + \delta(o;c)] \approx 1$ or $P_{co} \ll 1/(F_{co}[\delta(o;c)+1])$ that,

$$\rho_c \approx F_{co}P_{co}\delta(o;c) \approx 2 \times 10^5 P_{co} = 2 \times 10^{-6}. \tag{6.14}$$

For a higher power excitation source in the region of optical lasers $P_{co} = 1$ W/(m^2 Hz), then $\rho_c = 8/9$.

Now that we know what the occupation probability of the color-center is we can write the true reaction rate as

$$\Gamma^{\uparrow m} = \rho_c \Gamma_B^{sp}(m, o; g, c) \approx 2 \times 10^{-14}\ \text{s}^{-1}, \tag{6.15}$$

when using the VUV lamp for exciting the color-center states. Calculating the steady state occupation probability of the isomeric state via process B we have,

$$\rho_m = \frac{\rho_c \Gamma_B^{sp}(m, o; g, c)}{\Gamma_\gamma^{sp}(g; m) + \rho_c \Gamma_B^{sp}(m, o; g, c)}. \tag{6.16}$$

Inputting values shows the occupation probability of the isomeric state can climb to $\rho_m \approx 2 \times 10^{-10}$ using the VUV lamp in a time $\tau \approx \rho_m/\Gamma^{\uparrow m} = 10^4$ s^{-1}. With a high powered laser for the $|o\rangle \to |c\rangle$ transition with $P_{co} = 1$ W/(m^2 Hz) one could reach $\rho_m \approx 9 \times 10^{-5}$ for via this process. This is less than the value shown earlier for direct nuclear excitation. Furthermore, comparing the rate of isomer excitation due to process B with that of direct nuclear excitation,

$$\frac{\rho_c \Gamma_B^{sp}(m, o; g, c)}{\Gamma_\gamma^a(m; g)} = 5 \times 10^{-4} \frac{P_{co}}{P_{mg}} \approx 5 \times 10^{-4}. \tag{6.17}$$

The difference in energy between the color-center and isomer is not known exactly. However, based on the current DFT calculations this difference is ≈ 2 eV. Because the transitions are close in energy, here it was assumed that the available power of the excitation sources at the isomeric energy $\omega_{mg} = \omega_m - \omega_g$ and the color-center $\omega_{co} = \omega_c - \omega_o$ where equal $P_{mg} = P_{co}$. This is to say, if we have two lasers with equal power, one with wavelength ω_{co} and the other with ω_{mg} then direct nuclear excitation is three orders faster than process B.

If one does not have access to equal power sources in the required energy ranges then this ratio of course changes, and the bridge process B may be a promising candidate for excitation. Although the color-center is still not well understood experimentally, based on the DFT calculation the group of color-center states takes up an energy region around $0.5 - 1$ eV thick, possibly making their excitation experimentally easier than that of the isomer with its narrow linewidth.

6.3.1 Stimulated Electronic Bridge

It is the interaction with the decaying electron that leads to EB excitation of the nucleus. The total energy of electronic decay from $|i\rangle \to |f\rangle$ is broken up into two pieces, one of these pieces is given to the nucleus and the other is emitted as a photon. To our knowledge, here we study for the first time the idea of stimulated EB. This is achieved with the use of external photons with frequency matched to the emitted photon in the spontaneous EB process. These external photons cause stimulated emission via a desired path in the electronic shell and thus increase the rate of a specific decay channel.

In the following, we will study this idea applied to the process B, as shown in Figure 6.5, in an effort to increase the EB excitation rates. This is done by providing photons with energy equal to the difference between the isomer and the color-center. Referring to the notation in Figure 6.5 we can write the required laser photon energy as $\omega_p = \omega_{if} - \omega_N = \omega_{cm}$. With this energy in the region of ≈ 2 eV we assume a typical optical laser power of $P_{cm} \approx 1$ W/(m^2 Hz) to be available. The rate of a stimulate process in terms of its spontaneous version is given by (4.7). Thus the rate of the isomer excitation for both the spontaneous and stimulated processes B and B_{st} is then

$$\begin{aligned}\Gamma^{\uparrow m} &= \rho_g \rho_c \left[\Gamma_B^{sp}(m, o; g, c) + \Gamma_B^{st}(m, o; g, c)\right] \\ &= \rho_g \rho_c \Gamma_B^{sp}(m, o; g, c)\left[1 + F_{cm}P_{cm}\right] \\ &\approx 8 \times 10^{-8}\ \text{s}^{-1},\end{aligned} \tag{6.18}$$

where the VUV lamp was used for initial excitation of the electron to the color-center. Comparing to direct nuclear excitation using the VUV lamp,

$$\frac{\Gamma^{\uparrow m}}{\Gamma_\gamma^a(m; g)} = \frac{\rho_g \rho_c \Gamma_B^{sp}(m, o; g, c)\left[1 + F_{cm}P_{cm}\right]}{\rho_g \Gamma_\gamma^{sp} F_{mg} P_{mg} \delta(g, m)} \approx 2 \times 10^3, \tag{6.19}$$

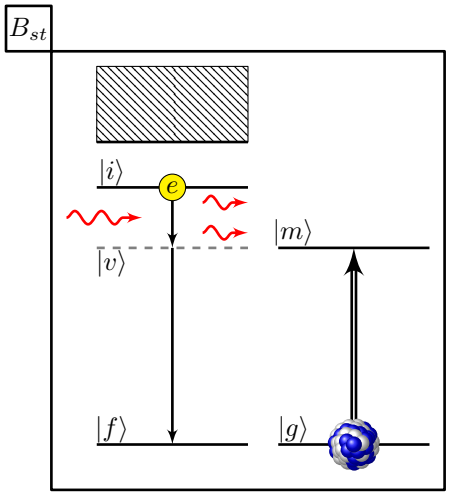

Figure 6.5: Stimulated EB scheme B_{st}: stimulation of scheme B with the use of laser photons of energy $\omega_p = \omega_{if} - \omega_N$. Note the electronic state can decay in two ways, first emitting the photon and then exciting the nucleus, or vice versa. Both options contribute to the rate. Here only the first is depicted.

where $P_{mg} = P_{co} = 10^{-11}$ W/(m^2 Hz) is the power of the VUV lamp in the energy range of ω_N. This stimulated scheme is three orders faster than directly driving the isomeric transition with the VUV lamp. Thus, the stimulated process is our most promising scheme as it can speed up the excitation of the isomer proportional to the power P_{cm} of the $c \to m$ of the optical laser used. Of course this scheme is more complicated as we require two excitation sources, the VUV lamp for initial population of the color-center and then an optical laser for the stimulation.

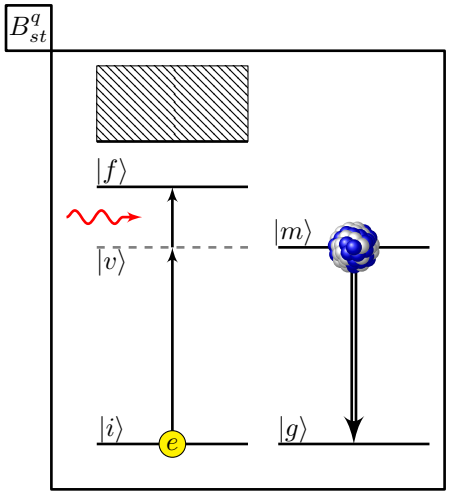

Figure 6.6: Quenching of isomeric state via EB scheme B^q_{st}: the use of laser photons of energy $\omega_p = \omega_{fi} - \omega_N$ can cause an increased decay rate of the isomeric state if the electronic shell is in its ground state. Note the electronic state can be excited in two ways, first by getting energy from the nucleus and then the laser photon, or vice versa. Both options contribute to the rate. Here only the first is depicted.

There are two important points to consider with this stimulated process:

1. The first is depicted in Figure 6.6. With the nuclei in the excited state and the electron shell in the ground state, the laser driving with energy $\omega_p = \omega_{fi} - \omega_N = \omega_{cm}$ ($= \omega_{if} - \omega_N = \omega_{cm}$ in Figure 6.5) can cause quenching, i.e., decay, of the isomeric state. This happens when the nucleus decaying to the ground state passes the energy to the electronic shell and the driving photon makes up the difference to bump the electron into the color-center. This is exactly the inverse of scheme B making the rate,

$$\Gamma^a_B(g,c;m,o) = \Gamma^{sp}_B(m,o;g,c) F_{cm} P_{cm} \delta(m,o;g,c) \approx 0.5 \text{ s}^{-1}. \tag{6.20}$$

The total decay rate of the isomeric state including spontaneous decay is then,

$$\Gamma^{\downarrow m} = \rho_m \left[\Gamma^{sp}_{\gamma}(g;m) + \rho_o \Gamma^{a}_{B}(g,c;m,o)\right], \tag{6.21}$$

hence the decay rate of the isomer increases with the use of the stimulating laser P_{cm} as well. Looking at the master equation for the isomeric level,

$$\dot{\rho}_m = \rho_g \rho_c \left[\Gamma^{sp}_{B}(m,o;g,c) + \Gamma^{st}_{B}(m,o;g,c)\right] - \rho_m \left[\Gamma^{sp}_{\gamma}(g;m) + \rho_o \Gamma^{a}_{B}(g,c;m,o)\right]. \tag{6.22}$$

The steady state occupation probability of the isomeric state is,

$$\rho_m = \frac{\rho_c \left[\Gamma^{sp}_{B}(m,o;g,c) + \Gamma^{st}_{B}(m,o;g,c)\right]}{\rho_c \left[\Gamma^{sp}_{B}(m,o;g,c) + \Gamma^{st}_{B}(m,o;g,c)\right] + \Gamma^{sp}_{\gamma}(g;m) + \rho_o \Gamma^{a}_{B}(g,c;m,o)}, \tag{6.23}$$

$$= \frac{\rho_c \Gamma^{sp}_{B}(m,o;g,c)[1 + F_{cm}P_{cm}]}{\Gamma^{sp}_{\gamma}(g;m) + \Gamma^{sp}_{B}(m,o;g,c)\left[F_{cm}P_{cm}\delta(m,o;g,c) + \rho_c\left[1 + F_{cm}P_{cm} - F_{cm}P_{cm}\delta(m,o;g,c)\right]\right]}. \tag{6.24}$$

Recall that $\Gamma^{sp}_{\gamma}(g;m) \approx 10^{-4}$ s^{-1}, $\Gamma^{sp}_{B}(m,o,g,c) \approx 10^{-8}$ s^{-1} and $\delta(m,o;g,c) = 8(2I_g + 1)/(2I_m + 1) = 12$. For the low powered VUV lamp $\rho_c \approx 2 \times 10^{-6}$, and using $P_{cm} \approx 1$ W/(m^2 Hz) in the range of optical lasers we get

$$\rho_m \approx 2 \times 10^{-7}. \tag{6.25}$$

Therefore, even with quenching this scheme provides a steady state occupation probability larger than that seen without stimulation. Revisiting the quench rate (6.21) we can input values where $\rho_o = 1 - \rho_c$ giving

$$\Gamma^{\downarrow m} \approx 8 \times 10^{-8} \text{ s}^{-1}. \tag{6.26}$$

For high power P_{co}, $\rho_c = 8/9$ and the isomeric occupation probability would be $\rho_m \approx 1$. We can understand this by noting that the P_{co} laser empties the electronic ground state preventing the stimulated quenching process B^q_{st}. Turning off the P_{co} laser which is used for initial population of the color-center will then leave the electronic shell predominantly in the ground state. Then the P_{cm} laser could be used intentionally to cause rapid quenching of the isomeric level which could aid in its measurement.

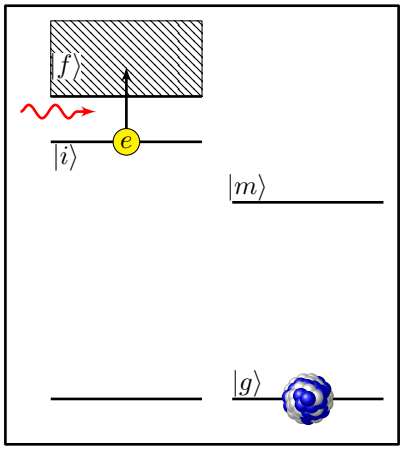

Figure 6.7: Laser photon intended to stimulate EB scheme B could act to further excite the electron initially in the color-center to the conduction band.

2. The second is that even if the nucleus is in the ground state, such that the above quenching process B^q_{st} doesn't occur, the electron in the color-center could be further excited into the conduction band by the input photon. This happens instead of the electron being stimulated to decay via process B_{st}, and is depicted in Figure 6.7. Excitation of the conduction band states from color-center states via E1 with photons ω_{cm} is the familiar

$$\Gamma^{a}_{E1}(b;c) = \left[\frac{4}{3}\frac{1}{N_b}\sum_{b_i,c_f,q}\left(\frac{\omega_{if}}{c}\right)^3 |\langle c_f|D_{E1,q}|b_i\rangle|^2\right] F_{cm}P_{cm}\delta(c;b), \tag{6.27}$$

where the laser providing photons of central frequency ω_{cm} will have a linewidth which determines the bounds of the summation according to overlap.

This two stage electron excitation $o \to c \to b$ decreases the occupation probability of the color-center, ρ_c, by promoting electrons to the conduction band. The master equation of the color-center with two excitation sources (one for the initial pumping of the color-center $o \to c$ with energy ω_{co}; and a second intended to stimulate the EB process with energy ω_{cm} but eventually causing excitation of the conduction band instead) is given by

$$\dot{\rho}_c = \rho_o \Gamma^a_{E1}(c;o) + \rho_b \left[\Gamma^{sp}_{E1}(c;b) + \Gamma^{st}_{E1}(c;b)\right] - \rho_c \left[\Gamma^a_{E1}(b;c) + \Gamma^{sp}_{E1}(o;c) + \Gamma^{st}_{E1}(o;c)\right]. \quad (6.28)$$

From here we can approximate the steady state occupation probability provided we make some assumptions on the lasers being used. Assuming the color-center is initially populated $\rho_c \approx 1$, we know from earlier,

$$\rho_b = \frac{F_{bc}P_{bc}\delta(c;b)}{1 + F_{bc}P_{bc} + F_{bc}P_{bc}\delta(c;b)} = 1 - \rho_c \quad (6.29)$$

here the $c \to b$ laser's intended use is to stimulate the bridge process requiring energy ω_{cm}. Hence, for excitation of the conduction band, there must be conduction band states such that $\omega_{bc} = \omega_{cm}$, i.e., $\delta(c;b) > 0$. Writing in terms of the color-center

$$\rho_c = \frac{1 + F_{cm}P_{bc}}{1 + F_{cm}P_{bc} + F_{cm}P_{bc}\delta(c;b)}. \quad (6.30)$$

With the color-center less than ω_{cm} away from the conduction band then for large power P_{cm} the occupation probability of the color-center drops to $\rho_c = 1/[1+\delta(c;b)]$. If the color-center is farther that E_{cm} away from the conduction band than there will be no conduction band excitation, and the population of the color-center will remain unchanged.

Therefore, one must be aware of (1) the possibility of quenching which can reduce the isomeric population and (2) additional excitation channels that, with the use of the stimulating laser, may deplete the population of the color-center states leading to reduced EB excitation rates.

6.4 C: EB starting from the color-center with energy less than the isomer

As discussed in Chapter 5, the energy of the color-center states in ^{229}Th:CaF_2 are not known experimentally. Furthermore, DFT calculations do not provide a reliable value. As such we cannot be sure that the color-center has energy larger than that of the isomer. With the color-center lower in energy than the isomer, other EB schemes become available.

The last EB scheme C is depicted in Figure 6.8. In this case the color-center is initially populated and assumed to be at lower energy than the nuclear isomeric state. The process is driven with a laser of energy $\omega_p = \omega_N - \omega_{if} = \omega_{mc}$ and the electron is excited to a virtual state at the energy of the isomer which decays to the electronic ground state passing the energy to the nucleus and exciting it to the isomeric state. This is analogous to the stimulated scheme B_{st} where the color-center energy is less than the one of the isomer.

Once again we can calculate the rate by first determining the rate of the spontaneous process, i.e., the inverse of Figure 6.8 using (4.4) written here as,

$$\Gamma^{sp}_C(g,c;m,o) = \frac{4}{3}\frac{1}{(2I_m+1)N_o}\sum_{\substack{M_m,M_g,\\ o_i,c_f,q}}\left(\frac{\omega_N - \omega_{fi}}{c}\right)^3 |\langle I_g, M_g, c_f|\widetilde{D}_{E1,q}|I_m, M_m, o_i\rangle|^2, \quad (6.31)$$

with the effective electric dipole matrix elements given by (4.4).

To approximate this, we use the same matrix elements of electronic operators $\boldsymbol{D}_{E1}$, $\boldsymbol{\mathcal{T}}_{M1}$ and $\boldsymbol{\mathcal{T}}_{E2}$ as calculated using the HSE wave functions. When computing the EB rates we scale the energy of only the color-center states down to below the isomer. Presented in Figure 6.9 is the spontaneous decay rate of the isomer via inverse of scheme presented in Figure 6.8 where the average energy of the isomer was varied. The electronic ground states used were $|o\rangle \in \{360^{\uparrow,\downarrow}\}$, color-center states $|c\rangle \in \{361^{\uparrow,\downarrow}, \ldots, 368^{\uparrow,\downarrow}\}$ and summing over intermediate states $|n\rangle \in \{360^{\uparrow,\downarrow}, \ldots, 407^{\uparrow,\downarrow}\}$.

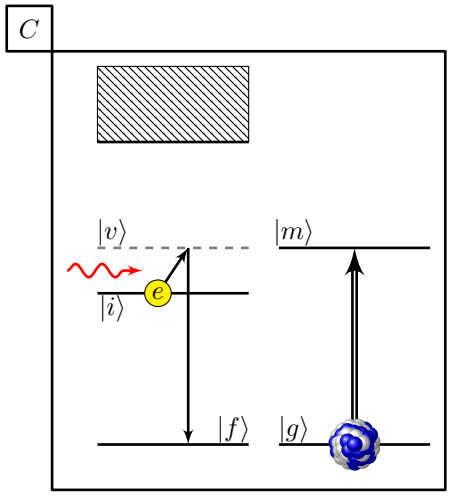

Figure 6.8: EB scheme C: excitation of the nuclear isomer via EB where the color-center states, which are initially populated, are lower in energy than the isomer. The electron in the color-center absorbs an externally supplied photon of energy $\omega_p = \omega_N - \omega_{if}$, and then passes the energy to the nucleus. Note the electronic state can first absorb the laser photon and then decay or vice versa. Both options contribute to the rate. Here only the first is depicted.

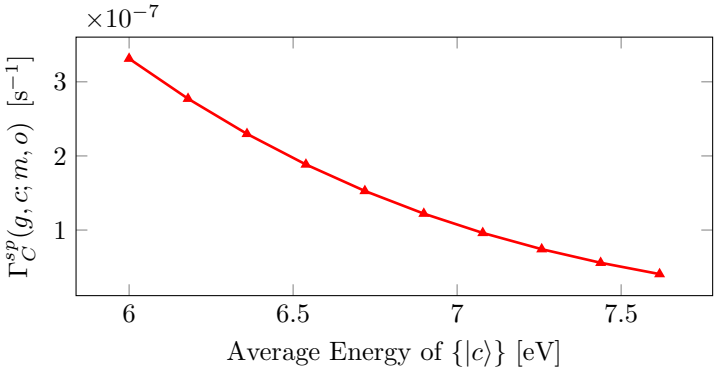

Figure 6.9: Spontaneous EB rate due to (6.31), i.e., inverse of process depicted in Figure 6.8, as a function of the average energy of the set of color-center states $\{|c\rangle\}$. Wave functions generated using HSE functional were used here.

The excitation rate via process C with the use of a laser of energy $\omega_p = \omega_N - \omega_{if} = \omega_{cm}$ is given by,

$$\Gamma^{\uparrow m} = \rho_c \Gamma^a_C(m, o; g, c) = \rho_c \Gamma^{sp}_C(g, c; m, o) F_{cm} P_{cm} \delta(g, c; m, o) \tag{6.32}$$

where $\delta(g, c; m, o) = 1/\delta(m, o; g, c) = 1/12$. This is similar to the stimulated EB rate via the B_{st} process. Figure 6.10 compares EB excitation rates via process C and B_{st} respectively where the average energy of the color-center is varied. When calculating (6.32), recall that $F_{cm} = 4\pi^3 c^2 \hbar^2 / E^3_{cm}$, hence the factor $\hbar^3 / E^3_{cm} = 1/(\omega_N - \omega_{fi})^3$ cancels the $(\omega_N - \omega_{fi})^3$ seen in $\Gamma^{sp}_C(g, c; m, o)$. Looking closer, we see that the dependence on energy is the result of only the denominators of the intermediate state summations in (4.4) which we will call $\Delta\omega$. Therefore, the energy dependence is

$$\Gamma^{\uparrow m} \propto |\langle I_g, M_g; c_f | \widetilde{D}_{E1,q} | I_m, M_m; o_i \rangle|^2 \propto \frac{1}{(\Delta\omega)^2}. \tag{6.33}$$

Thus as the color-center moves closer to the isomeric energy there is a resonance. This is because the dominant terms in the intermediate state summations of (4.4) are those where $\Delta\omega = \omega_{in} + \omega_N \to 0$ or $\Delta\omega = \omega_{fk} - \omega_N \to 0$, i.e., $\omega_{ni} \to \omega_N$ or $\omega_{fk} \to \omega_N$ respectively. Resonance thus happens when there is a real intermediate state close to the virtual state $|v\rangle$ sitting at the isomeric energy, $\omega_{vo} = \omega_N$. This resonance is also seen in similar laser induced electronic bridge (LIEB) processes for ions [35, 37]. As a result, by varying the color-center energy we see a resonance of the form

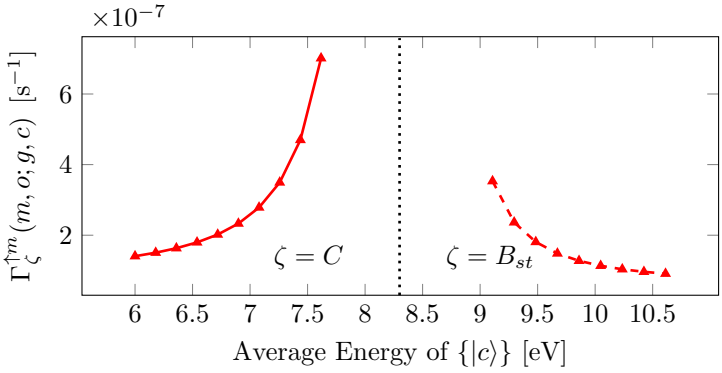

Figure 6.10: EB excitation rates via process C (red solid) and B_{st} (red dashed) respectively where the average energy of the color-center is varied. The isomeric energy is shown as a vertical dotted line at 8.3 eV. Wave functions generated using HSE functional were used here.

$\Gamma^{\uparrow m} \propto 1/(\omega_N - \omega_{co})^2$, where the process B_{st} and C define the excitation of the isomer when the color-center is higher and lower in energy than ω_N respectively.

If the electron's initial state were a level within the color-center with energy equal to the isomer, $\omega_{if} \equiv \omega(c_i, o_f) = \omega_N$, than there would be no emitted photon during its decay to the electronic ground state and subsequent nuclear excitation. Nuclear excitation in this case would be described as Nuclear Excitation by Electron Transfer (NEET). Here we are interested in EB processes only, and as such, the electronic transition must always move from initial to final over an intermediate state where by a real photon is emitted. This photon energy will vary depending on the scheme in question. To stimulate or drive the EB process one requires the input of external photons with this energy. We can then note that to stimulate or drive the EB process (B^{st} and C respectively) as $\omega_{if} \to \omega_N$ one requires a laser with photon energy where $\omega_p \to 0$. Clearly if this energy difference is too small than laser sources with sufficient power may not be available. We must also take care as we move towards resonance to include the level widths Γ_n in (4.1) previously neglected.

As with the stimulated process B_{st}, our EB rate is increased with the use of a second laser $P_{cm} = 1$ W/(m^{2}Hz) to bridge the gap between the color-center and the isomeric energy. Both processes yield similar excitation rates and require a similar laser setup, VUV lamp for initial excitation of an electron to the color-center and then a second laser in the optical or infrared range depending on the color-center energy.

When comparing to direct nuclear excitation with the VUV lamp alone we have similar enhancement for both B^{st} and C schemes. With average color-center energy at $\approx \pm 2$ eV,

$$\frac{\Gamma^{\uparrow m}_{\zeta}(m, o; g, c)}{\Gamma^{a}_{\gamma}(m; g)} \approx 10^3. \tag{6.34}$$

If the color-center states are found to be closer to the isomeric energy this rate will move towards the resonance, $1/(\Delta\omega)^2$, as shown in Figure 6.10. To this end we look forward to the prospect of first experimental measurements and characterization of the color-center states.

6.4.1 Internal conversion from excited states

The last rate that is of interest is that of Internal Conversion (IC) from the excited electronic color-center. With the nucleus in the isomeric state and the electron in the excited color-center, the decaying isomeric state could provide enough energy to promote the electron to a free electronic state and expel the electron from the crystals unit cell. IC is outlined in [37] for single atoms and can be calculated, however requires better knowledge of the conduction band levels and beyond which we currently lack in the crystal environment. To this end it will be an interesting topic for future investigation.

If IC is possible within the crystal, then it will act as a channel to quench the nuclear population that is in the isomeric state, similar to the quenching shown in B^q_{st}. The quench rate via IC will of course depend on the occupation probability of the isomeric state. In the thorium-doped crystal, before excitation the occupation probability of the isomer is negligible. Therefore, in the initial stages of excitation these quenching channels will not contribute. Only once a significant excitation is achieved, will the quenching channels play a role.

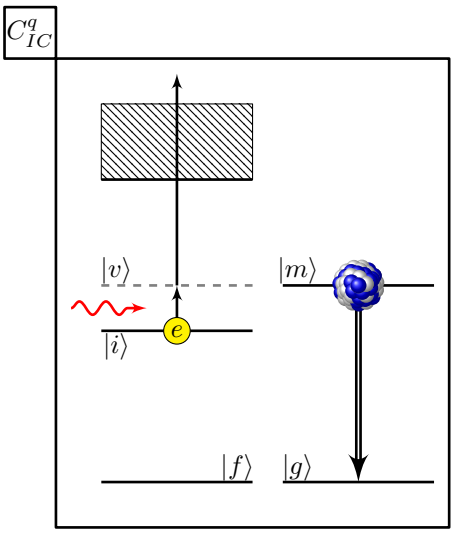

Figure 6.11: Illustration of IC channel, where the decaying nuclear isomer passes its energy to an already excited valence electron. The valence electron can then be removed from the system. This may happen with or without the addition of an external laser photon.

Chapter 7

Discussion of errors and approximations

Calculation of EB rates within the thorium-doped crystal provided many difficulties which are different to those seen in the calculation with ions. These were not all obvious at the outset of the project. Here we outline the various checks and approximations made during the generation of the calculation method for Th:CF_2.

7.1 Benchmark with quasi-relativistic wave functions

Before using wave functions for the thorium-doped crystal, the theory presented in Chapter 4 was benchmarked with previously published values for EB rates in ions. This was done using relativistic wave functions calculated with GRASP2K [37, 99, 100]. The relativistic wave functions $|nlj\rangle = \{5f_{5/2}, 6d_{5/2}, 7s_{1/2}, 7p_{1/2}, 8s_{1/2}, 7d_{3/2}\}$ were calculated for electronic states in Th^{3+}. Using these wave functions, matrix values for the operators involved in the EB process were calculated and compared for accuracy.

Previous calculations done by Bilous [37], involved thorium ions. The ions have electronic wave functions which are eigenstates of angular momentum and parity. As such, angular integration can be carried out analytically leaving only the radial integration to be performed numerically. Because of this only the radial component without spin was calculated. Files were organized in columns $(r, P_{nlj}(r), Q_{nlj}(r))$ where P and Q are the large and small components of the Dirac wave functions respectively, n is the principal quantum number l the orbital angular momentum and j the total angular momentum.

From these relativistic wave functions, we create a set of single-component non-relativistic wave functions[40] by using the large component $P_{nlj}(r) = P_{nl}(r)$ only. The resulting wave functions can then be generated in all space via,

$$\psi_{nlm_l}(r, \theta, \phi) = \frac{1}{r} P_{nl}(r) Y_{lm_l}(\theta, \phi). \tag{7.1}$$

where m_l is the projection of l. The spin component then is added once again by hand. For electrons, spin $s = 1/2$ and its projection can be $m_s = \pm 1/2$. To account for this we can write

$$|n, l, m_l\rangle|s, m_s\rangle = |n, l, m_l\rangle|m_s\rangle = \psi_{nlm} \begin{pmatrix} \psi(\frac{1}{2}) \\ \psi(-\frac{1}{2}) \end{pmatrix} \tag{7.2}$$

where the electron spin can be left out of the notation as it is always $s = \frac{1}{2}$, and where $|\psi(\pm\frac{1}{2})|^2$ is the probability to be spin up, $m_s = 1/2$, or down, $m_s = -1/2$. For this there are two options

$$|n, l, m_l\rangle|\tfrac{1}{2}\rangle = \psi_{nlm} \begin{pmatrix} 1 \\ 0 \end{pmatrix}, \quad |n, l, m_l\rangle|-\tfrac{1}{2}\rangle = \psi_{nlm} \begin{pmatrix} 0 \\ 1 \end{pmatrix}. \tag{7.3}$$

The relativistic wave functions have a defined total angular momentum j. Hence, given our set of approximate wave functions $|n, l, m_l\rangle|s, m_s\rangle$ we can then generate a new and final set of wave functions with defined j and its projection m_j, where for electrons $j = l \pm \frac{1}{2}$ and $m_j = m_l + m_s$.

[40] Quasi-relativistic as they are generated using the relativistic functions.

For this we construct,

$$|n,l,j,m_j\rangle = \sum_{m_s,m_l} C^{\ s\ \ l\ \ j}_{m_s m_l m_j} |m_s\rangle |n,l,m_l\rangle \tag{7.4}$$

where the value of j is given by the relativistic wave function from which we approximated, and $C^{\ s\ \ l\ \ j}_{m_s m_l m_j}$ is the Clebsch-Gordan coefficient. We call these quasi-relativistic wave functions. Quantum numbers n,l,j are given by the wave functions from Bilous and projection m_j can take $(2j+1)$ values, $\{-j,-j+1,\ldots,j\}$.

In practice matrix elements are calculated via,

$$\langle n,l,j,m_j|O|n',l',j',m'_j\rangle = \sum_{m_s,m_l,m'_s,m'_l} C^{\ s\ \ l\ \ j}_{m_s m_l m_j} C^{\ s'\ \ l'\ \ j'}_{m'_s m'_l m'_j} \langle n,l,m_l|\langle m_s|O|m'_s\rangle|n',l',m'_l\rangle \tag{7.5}$$

where the spin component is solved using,

$$\langle n,l,m_l|\langle m_s|O|m'_s\rangle|n',l',m'_l\rangle = \int \psi^*_{nlm_l}\langle m_s|O|m'_s\rangle\psi_{n'l'm'_l} r^2 \sin\theta \,\mathrm{d}r\,\mathrm{d}\theta\,\mathrm{d}\phi, \tag{7.6}$$

and $\langle m_s|O|m'_s\rangle$ has been given in Section 4.1. Using this procedure matrix elements of all operators can be calculated, as well as EB rates using the usual

$$\Gamma_{EB} = \frac{4}{3}\left(\frac{\omega_p}{c}\right)^3 \frac{1}{(2I_m+1)(2j_i+1)} \sum_{\substack{M_m,M_g,\\ m_i,m_f,q}} |\langle I_g,M_g,n_f,l_f,j_f,m_f|\widetilde{D}_{E1,q}|I_m,M_m,n_i,l_i,j_i,m_i\rangle|^2, \tag{7.7}$$

where the states are denoted by

$$|I,M,n,l,j,m_j\rangle = |I,M\rangle|n,l,j,m_j\rangle, \tag{7.8}$$

with I and M the total nuclear angular momentum and its projection quantum number respectively[41].

Here we are dealing with eigenstates of angular momentum and parity. Because of this we know the selection rules for each matrix operator, which determine the overall symmetry of the matrix. All matrix elements of each operator are calculated numerically and then checked to ensure they posses this known symmetry due to selection rules. The check involves comparing matrix elements known to be zero analytically with their numerically calculated values. This check is only possible because we know the symmetry ahead of time, something that is not the case for DFT wave functions in the crystal environment. Further discussion of this covered in the Section 7.2.1.

Several interesting points were found to be noteworthy. Firstly, following the above procedure only considers the large component, $P(r)$, of the relativistic wave functions. This was assumed to be sufficient as the small component, $Q(r)$, was at least an order of magnitude smaller and did not contribute significantly to the normalization of the wave functions, $\int \psi^*\psi \,\mathrm{d}\boldsymbol{r} = 1$. It was found however, that despite the size of the small component it was the dominant contribution for some matrix elements and thus the final transition rate. Secondly, the importance of the so called Fermi Contact (FC) term became apparent. The FC term referring to the delta function in the magnetic dipole coupling operator, $T_{M1,q}$ shown in equation (4.28), is dominant when considering transition between s-states. More specifically, it is the value of the wave function at the nucleus that is of critical importance. This is a know issue in the literature [101–105] as it is difficult to accurately calculate the value of the wave function at the origin. In this case a fitting procedure was used to determine an approximate value of the wave function at zero, as discussed in Appendix A.12. In the case of thorium-doped crystals, there is little s-like character to the wave functions used for the bridge process considered here and thus the FC term does not cause a significant effect. Moving forward, it is clear that a fully relativistic treatment would be beneficial to check the results presented here. Such a calculation would avoid both of these issues as (1) the small component would be addressed, and (2) the FC delta function does not appear in the fully relativistic operator seen in [37, 38, 84], and thus error due to the calculation of the origin point would be removed.

[41] In general other quantum numbers for the nucleus and electronic shell can be added to define the states.

7.2 DFT wave functions of undefined (j, m_j)

7.2.1 Checks based on selection rules

The wave functions of Th in the crystal environment are neither eigenstates of angular momentum nor of parity. They are only defined by their energy, $|E_i\rangle$. Because of this we cannot predict via selection rules the symmetry of the transition operators. This can be understood by considering the following example of a symmetry check of the E1 operator:

Let $\{|\phi_n\rangle\}$ be the full set of wave functions which are eigenstates of angular momentum and thus possess a defined parity, since the inversion operator commutes with the angular momentum operator [48, p.97] [42]. Then any other wave function can be expressed as a linear combination of wave functions from this set,

$$|E_i\rangle = \sum_n c_{in}|\phi_n\rangle. \tag{7.9}$$

Consider as an example the electric dipole operator $\boldsymbol{D}_{E1}$, acting on these new wave functions,

$$\langle E_f|D_{E1,q}|E_i\rangle = \sum_{n,m} c^*_{fm}c_{in}\langle\phi_m|D_{E1,q}|\phi_n\rangle. \tag{7.10}$$

Due to selection rules for the E1 operator $\langle\phi_n|D_{E1,q}|\phi_n\rangle = 0$ as $\{|\phi_n\rangle\}$ have defined parity and E1 transitions require a change in parity to be nonzero. If we then consider the set $\{|E_i\rangle\}$, we see that diagonal elements are not necessarily zero[43]

$$\langle E_i|D_{E1,q}|E_i\rangle = \sum_{\substack{n,m,\\ m\neq n}} c^*_{im}c_{in}\langle\phi_m|D_{E1,q}|\phi_n\rangle. \tag{7.11}$$

Based on the above we can see that the symmetry of $\boldsymbol{D}_{E1}$ related to parity is only obvious when acting on states $|\phi_n\rangle$ but not $|E_n\rangle$. Checking the symmetry of the numerically calculated operators is a powerful tool to rule out bugs during computation. Continuing with the above example, one can compare matrix elements known to be zero analytically with their numerically calculated values. Similar checks are available when considering angular momentum selection rules via the Wigner-Eckhart theorem[44], however in both cases are not useful when working with wave functions that are not eigenstates of angular momentum and parity.

This is why the check with quasi-relativistic wave functions was so important, as these properties could be used to ensure there were no errors by checking matrix operators had the proper symmetry before moving blindly into the calculation using crystal wave functions.

7.2.2 Brute force checks: grid choice

In the crystal environment, there is only one method to test for integration error in the calculation, the brute force method. Here this is described using the ortho-normalization condition.

Numerical integration requires dealing with discretely sampled functions. The choice of sampling frequency will be called the grid. This grid is simply the three dimensional array of points in space for which we generate values of our wave functions. Improper choice of grid will result in loss of information as the functions are not well represented by the chosen discretization. This is an overall error in this calculation. The error due to choice of grid can be most easily seen in the evaluation of the ortho-normalization matrix of the form

$$\langle E_f|E_i\rangle = \int \psi^*_f\psi_i \,\mathrm{d}\boldsymbol{r}. \tag{7.12}$$

Analytically we know the answer to this,

$$\langle E_f|E_i\rangle = \int \psi^*_f\psi_i \,\mathrm{d}\boldsymbol{r} = \delta_{fi}, \tag{7.13}$$

all diagonal elements should equal unity, and all off diagonal elements zero. However, in practice this relies heavily on the choice of grid. If the wave functions are sampled sufficiently this will hold

[42] Hence these wave functions can be relabeled as $\{|n, j, m_j\rangle\}$ where, n is the principal quantum number for energy, j that of angular momentum and m_j its projection.

[43] This should be especially clear in the crystal environment, as there can be permanent dipoles formed due to the interaction of neighbouring atoms.

[44] A matrix element $\langle jm_j|O_{k,q}|j'm'_j\rangle$ is only non-zero provided $\boldsymbol{j} = \boldsymbol{j'} + \boldsymbol{k}$ and $m_j = m'_j + q$.

true and if they are under sampled it will not. The closer the diagonal elements are to unity the better the grid is at representing that particular wave function.

The problem is that there is not one choice of grid that can sample all wave functions in the crystal sufficiently. For example, states that are localized around the thorium nucleus are well represented by a spherical grid centered on Th where there is a fixed number of points in the angular dimensions θ and ϕ, and grid points are spaced at a distance $r_n = e^{n/\kappa} \cdot r_0$ in the radial direction, r_0 is the smallest r value and κ a scaling factor chosen to sample the region, and $n = \{0, 1, 2, \ldots\}$. Such a grid has a high sampling rate near Th and it becomes less and less as you move farther away. Integration of the norm squared of wave functions localized on Th with this grid yield results close to unity. For de-localized wave functions with respect to this choice of grid, carrying out the same integral can yield results below 0.5. By changing the grid one can favor one region of the unit cell over another to better represent wave functions localized in a given area, however it must be noted that not all wave functions are localized around an origin such as those representing the crystals conduction band. These de-localized wave functions cannot be well represented by any spherical grid regardless of the choice of origin.

One could choose, instead of a spherical grid, a linear Cartesian grid. This grid will equally sample all wave functions in the unit cell which looks appealing at first glance. Upon further inspection, it becomes a game of numbers and computational power. With linear sampling on the Cartesian grid there is a fixed spacing between grid points, i.e $\Delta V = \Delta x \Delta y \Delta z$. For the same total number of points in the grid, the Cartesian grid poorly samples all wave functions, where as the spherical grid well represents those localized around the origin and poorly those at the edges. As such if we denote $\varepsilon(x, S/C)$ as the error on calculation of x using the Spherical S grid centered on Th or Cartesian C grid with equal total number of points to the spherical option, then

$$\varepsilon(\langle c|O|c\rangle, S) < \{\varepsilon(\langle c|O|o\rangle, S), \varepsilon(\langle b|O|c\rangle, S)\} < \{\varepsilon(\langle b|O|b\rangle, S), \varepsilon(\langle b|O|o\rangle, S), \varepsilon(\langle o|O|o\rangle, S)\},$$
$$\varepsilon(\langle c|O|c\rangle, C) \approx \{\varepsilon(\langle c|O|o\rangle, C), \varepsilon(\langle b|O|c\rangle, C)\} \approx \{\varepsilon(\langle b|O|b\rangle, C), \varepsilon(\langle b|O|o\rangle, C), \varepsilon(\langle o|O|o\rangle, C)\}.$$

Comparing the two grids,

$$\begin{aligned}
\varepsilon(\langle c|O|c\rangle, S) &< \varepsilon(\langle c|O|c\rangle, C),\\
\varepsilon(\langle c|O|o\rangle, S) &< \varepsilon(\langle c|O|o\rangle, C),\\
\varepsilon(\langle b|O|c\rangle, S) &< \varepsilon(\langle b|O|c\rangle, C),\\
\{\varepsilon(\langle b|O|b\rangle, S), \varepsilon(\langle o|O|o\rangle, S), \varepsilon(\langle b|O|o\rangle, S)\} &\gtrapprox \{\varepsilon(\langle b|O|b\rangle, C), \varepsilon(\langle o|O|o\rangle, C), \varepsilon(\langle b|O|o\rangle, C)\}
\end{aligned}$$

where $|o\rangle$, $|c\rangle$ and $|b\rangle$ refer the electronic ground, color-center and conduction band states respectively. Note these rules apply to matrix elements $\langle i|O|j\rangle$ and $\langle j|O|i\rangle$ in the same way.

Calculations presented here use a spherical grid where the number of points $(N_r, N_\theta, N_\phi) = (353, 29, 60)$, the spacing in angular components is constant and the spacing in the radial component follows $r_n = e^{n/\kappa} \cdot r_0$ where $r_0 = 0.000135\, a_0$, a_0 is the Bohr radius, and $\kappa = 31.25$ chosen by default in VASP. Spherical grids as large as $(N_r, N_\theta, N_\phi) = (353, 44, 90)$ or $\approx 2.3\times$ as many total grid points where used, however, the order of magnitude of EB rates calculated did not change and thus the smaller grid was chosen for computation speed.

To visualize the errors discussed above, we compare the results from calculation of $\Gamma^{sp}_{E1}(o_f; c)$ using both a Cartesian and spherical grid respectively. The Cartesian grid has discretization $(N_x, N_y, N_z) = (85, 85, 85)$ and the spherical grid has $(N_r, N_\theta, N_\phi) = (353, 29, 60)$, i.e., both grids have approximately the same total number of points, however with different distributions in space. Both calculations use the same wave functions calculated using the HSE functional. The results are shown in Figure 7.1, where the rates as calculated on the spherical grid where shown earlier in Figure 6.2. As we can see, all rates calculated with the Cartesian grid are less than those seen for the spherical grid. We know from above, $\varepsilon(\langle c|O|o\rangle, S) < \varepsilon(\langle c|O|o\rangle, C)$, that the error is larger for the Cartesian grid when it comes to transitions from $|c\rangle \to |o\rangle$. More specifically, the Cartesian grid under samples all wave functions equally. This means with the chosen discretization $\int \mathrm{d}\boldsymbol{r}|\psi|^2 < 1$ for all wave functions. In contrast, the spherical grid does a good job of sampling wave functions localized around the thorium nucleus. Hence the color-center wave functions are well represented, $\int \mathrm{d}\boldsymbol{r}|\psi|^2 \approx 1$, and thus their interaction with other wave functions is also better represented. The rate plotted in Figure 7.1 depends only on transition matrix elements of the form $\langle o|O|c\rangle$ and thus the spherical grid is more accurate than the Cartesian grid in calculation of the spontaneous decay from the color-center to the ground states, $\Gamma^{sp}_{E1}(o_f; c)$.

The issues presented above show that there is not an ideal choice of grid for every case. In particular, the de-localized wave functions are not sampled well using the spherical grid, and thus a Cartesian grid should be chosen in the future to check values of matrix element between all

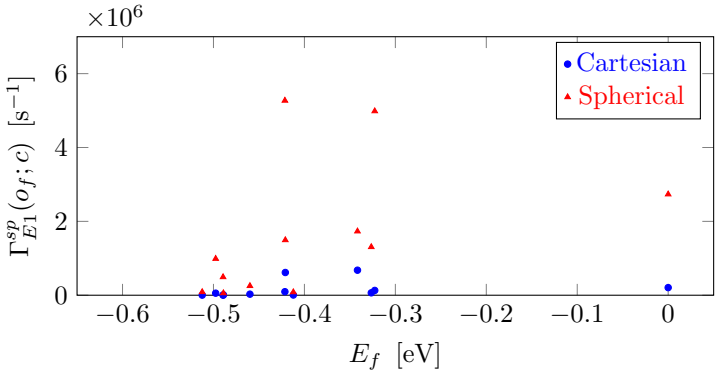

Figure 7.1: Comparison of rates $\Gamma^{sp}_{E1}(o_f; c)$ calculated using both a Cartesian and spherical grid respectively. The Cartesian grid has discretization $(N_x, N_y, N_z) = (85, 85, 85)$ and the spherical grid has $(N_r, N_\theta, N_\phi) = (353, 29, 60)$. Both calculations use the same wave functions calculated using the HSE functional.

de-localized wave functions. Then one must increase the number of total points in the three-dimensional grid until the calculation of rates Γ and normalization $|\psi|^2$ converge.

7.2.3 Brute force checks: intermediate states

When calculating EB processes there is an additional convergence test that must be carried out. All EB processes require calculation of matrix elements similar to equation (4.4), re-written here for reference,

$$\langle g, f|\widetilde{\boldsymbol{D}}_{E1}|m, i\rangle = \sum_{\lambda K, q}(-1)^q \left[\sum_n \frac{\langle f|\boldsymbol{D}_{E1}|n\rangle\langle n|\mathcal{T}_{\lambda K,q}|i\rangle}{\omega_{in}+\omega_N} + \sum_k \frac{\langle f|\mathcal{T}_{\lambda K,q}|k\rangle\langle k|\boldsymbol{D}_{E1}|i\rangle}{\omega_{fk}-\omega_N}\right]\langle g|\mathcal{M}_{\lambda K,-q}|m\rangle,$$

where there is a summation over intermediate states represented by sets $\{|n\rangle\} = \{|k\rangle\}$. In principle this summation is over all open states, that includes ground, color-center, conduction band and continuum. Looking at the denominator of the two summations we see there is the energy difference between initial and intermediate or final and intermediate states. As this energy difference becomes large the terms contribute less and less to the calculated rate. Here both the ground states and color-center states are used in all calculations. We must then include an increasing number of conduction band states in the set of intermediate states $\{|n\rangle\}$ until the EB rate converges below a predefined tolerance.

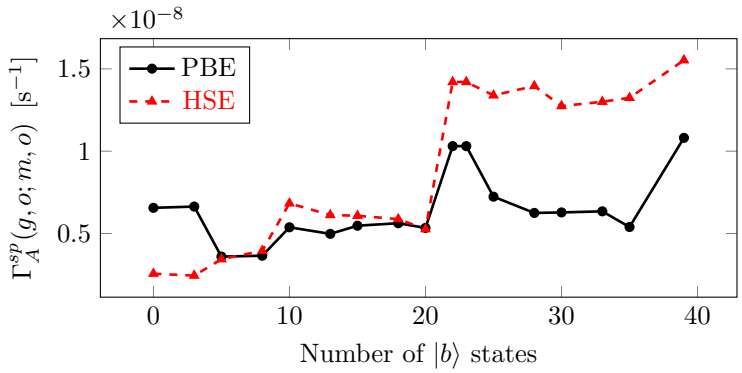

Figure 7.2: Convergence test of $\Gamma^{sp}_A(g, o; m, o)$ carried out by increasing the number of conduction band states considered in the sum over intermediate states. Note that each conduction band states $|b\rangle$ is spin degenerate so the total number of states accounting for degeneracy is twice as much as that shown on the x-axis.

The rates of process A and B covered in Chapter 6 as a function of conduction band states are shown in Figure 7.2 and Figure 7.3, respectively. In both graphs, the result of using two different sets of wave functions generated using the PBE and HSE functionals respectively are shown.

We expect that with increasing number of conduction band states, the final rate should be monotonically increasing as it approaches an asymptotic limit. This is because the EB rate is proportional to $\sum_{i,f,q} |\langle f|\widetilde{D}_{E1,q}|i\rangle|^2$ and each additional conduction band state will add a smaller and smaller positive value to this summation. This brings us to our first point. Figure 7.2 shows that the rate increases with increasing number of conduction band states, however, the data points are not monotonically increasing. This suggests there is a problem with the matrix elements involved and most likely is due to sampling on the grid as discussed in Section 7.2.2. This makes sense as the rate in question, $\Gamma_A^{sp}(g,o;m,o)$, has both initial and final states as part of the delocalized ground state set $\{|o\rangle\}$ which are poorly sampled on the spherical grid. Therefore, more of the matrix elements involved in the calculation will be in the largest error category[45] as compared to rates where either the initial, final or both states are the well sampled color-center states.

Looking now at Figure 7.3 we see that we have a monotonically increasing rate as a function of number of conduction band states. Based on the same argument as before we expect this rate to be more accurate as the initial electronic state is always part of the well sampled color-center $\{|c\rangle\}$. There exists a step like behavior that shows there are some states contributing more to the EB rates that others. This behavior may also be an artifact of poor sampling of wave functions by the grid, and if so should become less and less apparent with increased sampling.

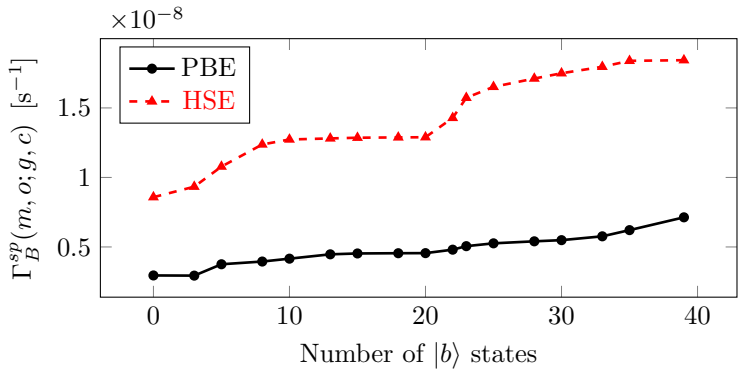

Figure 7.3: Convergence test of $\Gamma_B^{sp}(m,o;g,c)$ carried out by increasing the number of conduction band states considered in the sum over intermediate states. Note that each conduction band states $|b\rangle$ is spin degenerate so the total number of states accounting for degeneracy is twice as much as that shown on the x-axis.

As discussed earlier, the larger the difference in energy between the intermediate state and the initial or final state, ω_{in} and ω_{fk} respectively, the smaller the contribution to the rate. This is because of the denominators of the intermediate summations seen in $\widetilde{\boldsymbol{D}}_{E1}$. However, we note that a summation proportional to $\sum_x 1/x$ does not converge, and therefore the numerator, i.e., terms like $\langle f|\boldsymbol{D}_{E1}|n\rangle\langle n|\mathcal{T}_{\lambda K,q}|i\rangle$ must also decrease with increasing energy for convergence to take place. In the case of ions, it is clear that with increasing energy the wave functions become more and more delocalized. Thus their overlaps with localized wave functions as well as their matrix elements decrease to the point where they can be neglected. In the case of EB in the crystal environment, we deal with only few localized wave functions. The majority are delocalized, even in the most crude approximation of few total states. Therefore delocalized states play a significant role for all EB processes in the crystal. This makes computation more difficult that in the case of ions.

The rate at which the numerator $\langle f|\boldsymbol{D}_{E1}|n\rangle\langle n|\mathcal{T}_{\lambda K,q}|i\rangle$ decreases with increasing intermediate state energy is unclear at this point. If further investigation revealed this rate, one could attempt to find the contribution of higher energy states by considering the intermediate summation as an integration involving the density of states $g(\omega)$ of the conduction band which could be calculated using DFT,

$$\sum_n \frac{\langle f|\boldsymbol{D}_{E1}|n\rangle\langle n|\mathcal{T}_{\lambda K,q}|i\rangle}{\omega_{in}+\omega_N} \longrightarrow \int_\omega^\infty f(\omega)g(\omega)\,\mathrm{d}\omega.$$

Currently our only option to improve the estimate of EB rates in the crystal environment is via brute force, both higher sampling and more intermediate states. To this end, we expect EB rates will only be larger than the values quoted here.

[45] Defined in Section 7.2.2 for the spherical grid as, $\{\varepsilon(\langle b|O|b\rangle, S), \varepsilon(\langle b|O|o\rangle, S), \varepsilon(\langle o|O|o\rangle, S)\}$.

Conclusions & Outlook

This dissertation was dedicated to the theoretical investigation of ^{229}Th's isomeric excitation in the crystal environment. This was broken down into two main parts, the first covering direct excitation of the nuclear isomer via NFS style schemes and the second covering excitation with EB.

Part I of this dissertation covered nuclear forward scattering with the use of narrowband polarized lasers. Excitation schemes for both two- and three-level systems in ^{229}Th:CaF_2 crystals were investigated theoretically. We showed that the complex crystal system with 10 levels and three q-axes can be understood when looking at simplified two- and three-level systems with a single quantization axis. We defined a resonance condition $E_{\Delta_i} < E_p < E_Q$, where E_{Δ_i} is the detuning in energy of the driving laser to the i^{th} transition, E_p is the energy spread of the laser pulse and E_Q the quadrupole level splitting. The level simplifications are valid provided we satisfy this condition of resonance for only the levels of interest. If so, all other transitions can be safely neglected. Within these approximations, the result of selectively driving (with polarized fields) two- and three-level systems where explored.

It was shown that both the time delay and phase shift between excitation pulses can cause a change in intensity of the measured signal in NFS experiments. To reliably increase the signal intensity using multiple excitation pulses, the detuning of the driving laser to the transition of interest must be known. Once initial excitation is found in the two-level system ($|\frac{5}{2}, \frac{5}{2}\rangle \rightarrow |\frac{3}{2}, \frac{3}{2}\rangle$), multipulsed excitation can be used to increase the intensity of the signal and determine the laser detuning in the system. Additionally, a signature of excitation in the form of quantum beating can be created by (i) a second laser to couple the $|\frac{5}{2}, \frac{3}{2}\rangle$ and $|\frac{3}{2}, \frac{3}{2}\rangle$ levels or (ii) a second crystal in a static magnetic field. Where both the intensity of the couple laser and strength of the applied static magnetic field serve to change the period of the quantum beating.

These findings are anticipating first coherent driving of the thorium nucleus with VUV sources, which have so far failed mainly due to our poor knowledge of the transition frequency. A more exact value for the latter remains a prerequisite for any attempt to directly excite with lasers the nuclear isomer in the simplified NFS schemes outlined here. Once this is known to the level of the quadrupole splitting in the crystal environment, one can discuss further these schemes presented here as well as other possibilities using NFS.

Due to the strict energy requirements of the NFS schemes presented, their realization experimentally is not within reach at the current time. Therefore in Part II we investigated for the first time EB processes in thorium-doped crystals. EB relies on interaction of the nucleus with the electronic shell. In a variety of schemes we studied how energy could be exchanged between electronic color-center states and the nucleus with the goal of isomeric excitation. To drive the EB processes in question our lasers/radiation sources need to excite sets of electronic levels which can be far broader in energy than the nuclear isomer. Hence, these EB schemes would allow for excitation of thorium's isomeric state without the strict energy requirements of the NFS schemes presented earlier.

Two of the EB schemes studied here show the most promise. They are schemes B_{st} and C respectively and are actually closely related. The main difference is the assumption on the energy of the color-center. As discussed in Chapter 5 we do not know at the moment what the energy of these electronic color-center states are. As such scheme B_{st} and scheme C assume the color-center to be above and below the energy of the isomer respectively. Both schemes make use of a VUV lamp for initial excitation of the color-center states as well as an optical laser to stimulate (in the case of B_{st}) or drive (in the case of C) the respective bridge excitation schemes. These two schemes resulted in excitation rates on the order of 10^{-7} s^{-1} when the average color-center state energy was assumed to be $\approx \pm 2$ eV from the nuclear isomeric state. These EB rates are linearly dependent on the occupation probability of the electronic color-center states and the inverse square of the energy difference between the color-center energy and the nuclear isomeric state, $\Gamma^{\uparrow m} \propto \rho_c/(\omega_N - \omega_{co})^2$. Hence, the true occupation probability as well as color-center energy will determine this rate in future experimental efforts. In the context of the energy values and laser powers discussed, these

rates are three orders of magnitude larger than the direct excitation with the VUV lamp alone.

Beyond excitation, we have also shown how the optical laser can cause rapid quenching of the excited isomeric state when the VUV lamp is turned off. This process initially thought to be a detriment for excitation could in fact be used to aid in the experimental measurement process. As discussed in Section 6.3.1 initial excitation of the isomeric state could be achieved using EB, followed by deliberate quenching of that population at later time.

The two EB systems B_{st} and C have the potential to make an impact on current efforts to study excitation in the crystal environment. It should be noted that the results shown have several limitations such as grid sampling and limited summation over intermediate states as discussed in Chapter 7. This being said we expect that more accurate rates will only be larger than the ones quoted and hope to show this with future computational efforts. The limiting factor on immediate experimental implementation of these EB schemes is only in better experimental classification of the energy of the color-center states which is currently under way in the group of T. Schumm at the Technische Universität Wien.

There are many topics for future theoretical study surrounding the EB process in the crystal environment. The first would be to solidify our current results by increasing both the discrete sampling of wave functions and the number if intermediate states used in the computation. Our hope is to reach convergence in both of these areas thus bringing us closer to the true rate of the EB processes discussed. Beyond this the question of IC within the crystal can be explored to understand its impacts on EB excitation rates. If possible, IC could hinder the EB process by depleting the excited electronic states before nuclear excitation can occur. Similarly, we would like to further investigate other possible processes that deplete color-center population leading to reduced EB rates. Finally, we are also interested in looking at the relativistic corrections to EB processes in the crystal environment as discussed in Section 7.1. A non-relativistic first treatment was given here, however, as discussed is Section 7.1 the small component of the relativistic wave functions can play an important role in increasing EB rates in some cases.

Appendix: Details in development

A.1 Dynamical beat: ^{57}Fe

To demonstrate the dynamical beat seen in NFS spectrum we will consider a solid state ^{57}Fe target. The internal magnetic field B_0 can be several 100 kG [106] in iron. This internal magnetic field causes Zeeman splitting of the nuclear energy levels. The splitting depends on the magnetic dipole moments of the ground and excited states which are $\mu_g \approx 0.09\mu_N$ and $\mu_e \approx -0.15\mu_N$ [107, 108].

Due to iron's ferromagnetic nature, we can align the magnetic domains in the sample and therefore the magnetic dipole moments of all nuclei by applying a small[46] static external magnetic field [109, 110]. The strength of the field depends on the size of the sample but is usually on the order of a few 100's to a few 1000 G for these type experiments [106, 111] with foils on the order of μm thickness. The direction of the static external magnetic field defines the quantization axis of the entire sample taken here as $B = B_z$.

The levels $I_g = \frac{1}{2}$ and $I_e = \frac{3}{2}$ are thus split into $(2I + 1)$ magnetic sub-levels where the energy shift due to the Zeeman splitting is given by $\Delta E_I = \mu m_I B_0/\hbar$ where m_I is the projection of total angular momentum along the static magnetic field axis, B_z. This is shown, not to scale, in Figure A.1.

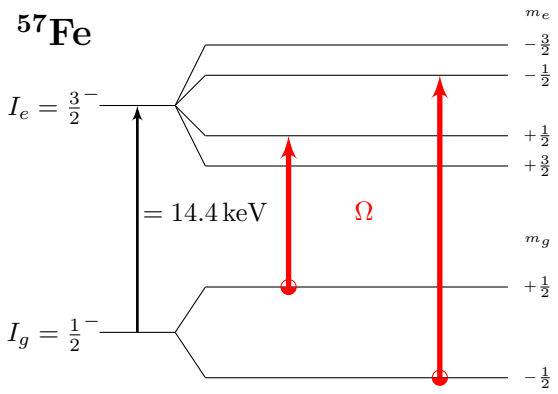

Figure A.1: Zeeman level-scheme of ^{57}Fe as a result of applied static magnetic field. Ω is the driving rabi frequency, $I_{g/e}$ are nuclear spins of the ground and excited state, respectively and $m_{g/e}$ the projection on the z-axis.

We can excite the two $\Delta m = 0$ transitions in this level structure with a single mode laser of frequency ν impinging along the y direction with polarization of the magnetic component matching the quantization axis along z. Being an M1 transition the interaction Hamiltonian is given by

$$\hat{V} = -\hat{\boldsymbol{m}} \cdot \boldsymbol{B}, \tag{A.14}$$

and the full Hamiltonian can be written as,

$$\hat{H} = \begin{pmatrix} 0 & 0 & 0 & V_{14} \\ 0 & \hbar\omega_2 & V_{23} & 0 \\ 0 & V_{32} & \hbar\omega_3 & 0 \\ V_{41} & 0 & 0 & \hbar\omega_4 \end{pmatrix}, \tag{A.15}$$

where ω_n is the frequency of level n and V_{ij} is the field component acting on the two $\Delta m = 0$, $j \to i$ transitions.

[46] In comparison the internal magnetic field at the Fe nucleus. When calculating the splitting this value can usually be neglected in comparison to the internal field.

The Zeeman splitting of the ground and excited state is given by Δ_g and Δ_e respectively, and ω is the frequency difference between the unsplit excited and ground state. Hence,

$$\begin{aligned}\omega_2 &= 2\Delta_g, &(A.16)\\ \omega_3 &= \omega + \Delta_g - \Delta_e, &(A.17)\\ \omega_4 &= \omega + \Delta_g + \Delta_e. &(A.18)\end{aligned}$$

The relaxation contribution is given by (1.13), where only internal decay from the excited state to ground state, i.e not between the split levels, is allowed

$$\hat{\rho}_r = \begin{pmatrix} \gamma_{13}\rho_{33}+\gamma_{14}\rho_{44} & 0 & -\frac{1}{2}(\gamma_{13}+\gamma_{23})\rho_{13} & -\frac{1}{2}(\gamma_{14}+\gamma_{24})\rho_{14} \\ 0 & \gamma_{23}\rho_{33}+\gamma_{24}\rho_{44} & -\frac{1}{2}(\gamma_{13}+\gamma_{23})\rho_{23} & -\frac{1}{2}(\gamma_{14}+\gamma_{24})\rho_{24} \\ -\frac{1}{2}(\gamma_{13}+\gamma_{23})\rho_{31} & -\frac{1}{2}(\gamma_{13}+\gamma_{23})\rho_{32} & -(\gamma_{13}+\gamma_{23})\rho_{33} & -\frac{1}{2}(\gamma_{13}+\gamma_{23}+\gamma_{14}+\gamma_{24})\rho_{34} \\ -\frac{1}{2}(\gamma_{14}+\gamma_{24})\rho_{41} & -\frac{1}{2}(\gamma_{14}+\gamma_{24})\rho_{42} & -\frac{1}{2}(\gamma_{13}+\gamma_{23}+\gamma_{14}+\gamma_{24})\rho_{43} & -(\gamma_{14}+\gamma_{24})\rho_{44} \end{pmatrix}.$$

Making the unitary transformation

$$\hat{U} = \begin{pmatrix} 1 & 0 & 0 & 0 \\ 0 & 1 & 0 & 0 \\ 0 & 0 & e^{-i\nu t} & 0 \\ 0 & 0 & 0 & e^{-i\nu t} \end{pmatrix}, \qquad (A.19)$$

gives the transformed density matrix $\hat{\tilde{\rho}} = \hat{U}^\dagger \hat{\rho} \hat{U}$

$$\hat{\tilde{\rho}} = (\tilde{\rho}_{ij}) = \begin{pmatrix} \rho_{11} & \rho_{12} & e^{-i\nu t}\rho_{13} & e^{-i\nu t}\rho_{14} \\ \rho_{21} & \rho_{22} & e^{-i\nu t}\rho_{23} & e^{-i\nu t}\rho_{24} \\ e^{i\nu t}\rho_{31} & e^{i\nu t}\rho_{32} & \rho_{33} & \rho_{34} \\ e^{i\nu t}\rho_{41} & e^{i\nu t}\rho_{42} & \rho_{43} & \rho_{44} \end{pmatrix}, \qquad (A.20)$$

and the transformed Hamiltonian $\hat{\tilde{H}} = i\hbar\partial_t \hat{U}^\dagger \hat{U} + \hat{U}^\dagger \hat{H} \hat{U}$,

$$\hat{\tilde{H}} = \begin{pmatrix} 0 & 0 & 0 & e^{-i\nu t}V_{14} \\ 0 & 2\hbar\Delta_g & e^{-i\nu t}V_{23} & 0 \\ 0 & e^{i\nu t}V_{32} & \hbar(\Delta + \Delta_g - \Delta_e) & 0 \\ e^{i\nu t}V_{41} & 0 & 0 & \hbar(\Delta + \Delta_g + \Delta_e) \end{pmatrix}, \qquad (A.21)$$

where $\Delta = \omega - \nu$.

The RWA is then made by expanding the form of the applied potential $\hat{V}$, and dropping the fast oscillating terms,

$$\begin{aligned}\tilde{H}_{eg} &= e^{i\nu t}V_{eg} &(A.22)\\ &= -\frac{\hbar}{2}\Omega_{eg}\left(e^{2i\nu t}+1\right) &(A.23)\\ &\overset{RWA}{\approx} -\frac{\hbar}{2}\Omega_{eg}. &(A.24)\end{aligned}$$

The Bloch equations $\partial_t \hat{\tilde{\rho}} = \frac{1}{i\hbar}[\hat{\tilde{H}}, \hat{\tilde{\rho}}] + \hat{\tilde{\rho}}_r$ in the RWA where Clebsch-Gordan coefficients have been factored out as usual, $\Omega_{ij} = |C_{ij}|\Omega$ and $\gamma_{ij} = C_{ij}^2\Gamma$ gives

$$\begin{aligned}\dot{\rho}_{11} &= -\frac{i}{2}|C_{41}|(\Omega\tilde{\rho}_{41}^* - \Omega^*\tilde{\rho}_{41}) + \Gamma(C_{31}^2\rho_{33} + C_{41}^2\rho_{44}), &(A.25)\\ \dot{\rho}_{22} &= -\frac{i}{2}|C_{32}|(\Omega\tilde{\rho}_{32}^* - \Omega^*\tilde{\rho}_{32}) + \Gamma(C_{32}^2\rho_{33} + C_{42}^2\rho_{44}), &(A.26)\\ \dot{\tilde{\rho}}_{32} &= \frac{i}{2}|C_{32}|\Omega(\rho_{22}-\rho_{33}) - \frac{1}{2}\left(2i\Delta_{32} + \Gamma(C_{31}^2 + C_{32}^2)\right)\tilde{\rho}_{32}, &(A.27)\\ \dot{\rho}_{33} &= \frac{i}{2}|C_{32}|(\Omega\tilde{\rho}_{32}^* - \Omega^*\tilde{\rho}_{32}) - \Gamma(C_{31}^2 + C_{32}^2)\rho_{33}, &(A.28)\\ \dot{\tilde{\rho}}_{41} &= \frac{i}{2}|C_{41}|\Omega(\rho_{11}-\rho_{44}) - \frac{1}{2}\left(2i\Delta_{41} + \Gamma(C_{41}^2 + C_{42}^2)\right)\tilde{\rho}_{41}, &(A.29)\\ \dot{\rho}_{44} &= \frac{i}{2}|C_{41}|(\Omega\tilde{\rho}_{41}^* - \Omega^*\tilde{\rho}_{41}) - \Gamma(C_{41}^2 + C_{42}^2)\rho_{44}, &(A.30)\end{aligned}$$

where $\Delta_{32} = \omega_3 - \omega_2 - \nu = \Delta - \Delta_g - \Delta_e$, $\Delta_{41} = \omega_4 - \nu = \Delta + \Delta_g + \Delta_e$ are the detunings to the $3 \leftrightarrow 2$ and $4 \leftrightarrow 1$ transitions respectively. The field equation is given by

$$\frac{1}{c}\partial_t\Omega + \partial_z\Omega = i\eta(|C_{32}|\rho_{32} + |C_{41}|\rho_{41}) \qquad (A.31)$$

where $\eta = \frac{N\sigma\Gamma}{2}$ and $\sigma = \frac{\lambda^2}{\pi(1+\alpha)}(2K+1)$. In the case of pure iron sample we can find the number density $N = 7.89$ g cm$^{-3} \div 55.8$ g mol$^{-1} \times 6.022 \cdot 10^{23}$ atoms mol$^{-1} = 8.5 \cdot 10^{22}$ atoms cm^{-3}. The decay rate of the upper state is $\Gamma = 1/\tau \approx 10^7$ s^{-1} ($\tau \approx 141$ ns [112]). The transition wavelength is $\lambda = 2\pi\hbar c/E \approx 8.6 \cdot 10^{-11}$ m where the transition energy is $E = 14.4$ keV, and for M1 transition K=1. Lastly, in the case of iron we must consider the internal conversion coefficient which is $\alpha \approx 9$ [113] making the cross section $\sigma \approx 10^{-19}$.

We then use as initial conditions for the MBE,

$$\rho_{11}(z,0) = \rho_{22}(z,0) = \frac{1}{2}, \tag{A.32}$$

$$\Omega(z,0) = \Omega_0, \tag{A.33}$$

$$\Omega(0,t) = \Omega_0 e^{-(t/T)^2}. \tag{A.34}$$

The pulse strength and width are chosen such that $\Omega_0 T < 1$ to prevent Rabi oscillations during the time the pulse is acting on the nuclei in the sample. For computational purposes, we choose $\Omega_0 \ll 1/T$ and a pulse width of $T = 1$ ns[47].

Solving for Ω as a function of time and plotting $I/I_0 \propto |\Omega/\Omega_0|^2$ gives the NFS intensity spectrum, Figure A.2. We pick an internal magnetic field of $B_0 = 25$ T, sample thickness $L = 1$ μm and laser detuning $\Delta = 0$. The red curve shows the quantum beating as a result of the Zeeman splitting (caused by B_0) of the ground and excited states Δ_g and Δ_e respectively. The dynamical beat due to multiple scattering is seen as the envelope to the quantum beats, and is given by the black curve. The dynamical beat curve is found by artificially setting $B_0 = 0$ and $\eta \to \eta/2$ which reduces the system to a two-level system with total population 1/2 of the 4-state system. Increasing the thickness of the sample will increase the chance of multiple scattering and thus the period of the dynamical beat decreases.

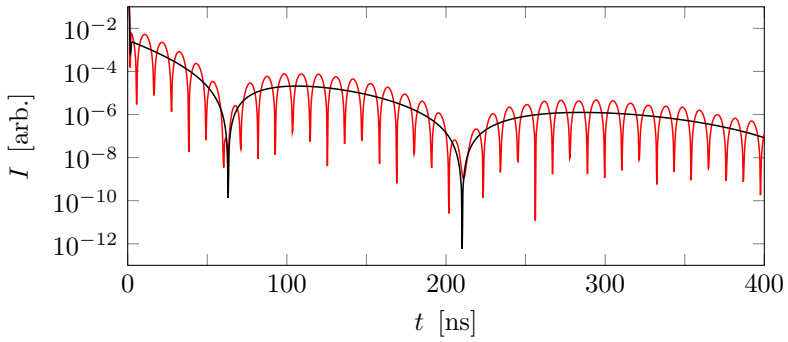

Figure A.2: NFS intensity spectrum for ^{57}Fe sample discussed in text with internal magnetic field $B_0 = 25$ T, sample thickness $L = 1$ μm and laser detuning $\Delta = 0$. The red curve shows the quantum beating as a result of B_0. The black curve shows the dynamical beat where $B_0 = 0$ and $\eta \to \eta/2$.

This system is the poster child of Mössbauer spectroscopy and thus can be seen in many publications including [54, 112, 114, 115].

A.2 Clebsch-Gordan coefficients, Wigner-Eckhart theorem

Clebsch-Gordan coefficients arise in the coupling of two eigenstates of angular momentum,

$$|j,m\rangle = \sum_{m_1,m_2} C^{j_1\ j_2\ j}_{m_2 m_2 m} |j_1,m_1\rangle |j_2,m_2\rangle. \tag{A.35}$$

Although Clebsch-Gordan coefficients and 3j-symbols are well defined, reduced matrix elements differ in the literature along with the statement of the Wigner-Eckhart theorem. In many cases different constants are absorbed into the reduced matrix element.

Starting with the definition of the Clebsch-Gordan coefficient shown in different notations [48,

[47] As long as the condition $\Omega_0 T < 1$ is satisfied the NFS spectrum will be the same.

p.436] [45, p.1177] [116, p.65] [117, p.224] [118, p.1056] [62, p.583] [89, p.475]

$$C^{j_1\ j_2\ j}_{m_1 m_2 m} = \langle j_1 m_1 j_2 m_2 | j m\rangle = \langle j_1 j_2 m_1 m_2 | j m\rangle = \langle m_1 m_2 | j m\rangle \tag{A.36}$$

$$= (-1)^{j_1 - j_2 + m}\sqrt{2j+1}\begin{pmatrix} j_1 & j_2 & j \\ m_1 & m_2 & -m\end{pmatrix} \tag{A.37}$$

The Clebsch-Gordan coefficients as well as the 3j-symbols are real [48, p.435-7] . As such, we can rewrite the phase factor, $(-1)^n = e^{i\pi n}$, and thus n must be an integer for $(-1)^n$ to be real. For n and integer, we also have $(-1)^n = (-1)^{-n}$. Therefore we can also write,

$$C^{j_1\ j_2\ j}_{m_1 m_2 m} = (-1)^{-j_1 + j_2 - m}\sqrt{2j+1}\begin{pmatrix} j_1 & j_2 & j \\ m_1 & m_2 & -m\end{pmatrix} \tag{A.38}$$

where $j_1 - j_2 + m$ is an integer. Rules for 3j-symbols can be seen for example in [45, p.1325]. The 3j-symbol

$$\begin{pmatrix} j_1 & j_2 & j \\ m_1 & m_2 & -m\end{pmatrix},$$

is only non-zero provided $m_1 + m_2 - m = 0$ and j_1, j_2, j must form sides of a triangle having integer perimeter i.e $|j_1 - j_2| \leq j$. Furthermore, we know from the properties of angular momentum that:

1. j_1, j_2, j are all positive, and $2j_1$, $2j_2$, $2j$ are all positive integers.
2. The projection of total angular momentum $m = (j, j-1, \ldots, -j)$, and thus $2m_1$, $2m_2$, $2m$, are all integers.

3j-symbols are invariant under cyclic permutations, and are multiplied by $(-1)^{j_1+j_2+j}$ for non-cyclic permutations. Replacing all magnetic quantum numbers by there negative $(m_1, m_2, -m) \rightarrow (-m_1, -m_2, m)$ gives the same factor $(-1)^{j_1+j_2+j}$.

Several equivalent statements of Wigner-Eckhart theorem are [63],

$$\langle \beta j m | T_{kq} | \beta' j' m'\rangle = (-1)^{j-m}\begin{pmatrix} j & k & j' \\ -m & q & m'\end{pmatrix}\langle \beta j || T_k || \beta' j'\rangle \tag{A.39}$$

$$= \frac{(-1)^{k-j'+j}}{\sqrt{2j+1}}\langle kqj'm'|jm\rangle\langle \beta j||T_k||\beta' j'\rangle \tag{A.40}$$

$$= \frac{(-1)^{j'-m'+2k}}{\sqrt{2k+1}}\langle jmj'-m'|kq\rangle\langle \beta j||T_k||\beta' j'\rangle \tag{A.41}$$

$$= \frac{(-1)^{2k}}{\sqrt{2j+1}}\langle j'm'kq|jm\rangle\langle \beta j||T_k||\beta' j'\rangle. \tag{A.42}$$

Note that we are concerned with tensor operators T_{kq}, where k is an integer, i.e., electric (Ek, q) of magnetic (Mk, q) transition operators. As such, $2k$ is an even integer and factors $(-1)^{2k} = 1$, thus can be dropped. $q = k, k-1, \ldots, -k$.

A useful relation between Clebsch-Gordan coefficients is also given by [63, p.38] [89, p.259],

$$\sum_{m_1, m_2} C^{j_1\ j_2\ j}_{m_1 m_2 m} C^{j_1\ j_2\ j'}_{m_1 m_2 m'} = \delta_{m,m'}\delta_{j,j'}\delta(j_1, j_2, j). \tag{A.43}$$

A.3 Decay rate, linewidth and lifetime

According to the Heisenberg's uncertainty principle

$$\Delta E \Delta t \gtrsim \hbar, \tag{A.44}$$

hence the width of a state in units of energy is

$$\Delta E \approx \hbar\Gamma, \tag{A.45}$$

where $\Gamma = \sum_i \Gamma_i$ is the total decay rate of the state, a sum of rates from all possible decay paths to all other possible states. The branching ratio, $B_i = \Gamma_i/\Gamma$ determines the fraction of particles decaying to the i^{th} state.

The population of the decaying state can be written

$$\rho(t) = e^{-\Gamma t}, \tag{A.46}$$

where the lifetime is given by $\tau = 1/\Gamma$. Therefore, the probability of being in that state is

$$|\psi(t)|^2 \propto e^{-\Gamma t} \tag{A.47}$$
$$\psi(t) \propto e^{-iEt/\hbar}e^{-\Gamma t/2} \tag{A.48}$$

where the time dependence of the wave function was introduced with central energy of the state E. Taking the Fourier transform in terms of angular frequency ω gives the wave function of the state in terms of ω where $\omega_0 = E/\hbar$

$$\phi(\omega) = \int_{-\infty}^{\infty} \psi(t)e^{i\omega t}dt \tag{A.49}$$
$$\propto \int_{0}^{\infty} e^{-iEt/\hbar}e^{-\Gamma t/2}e^{i\omega t}dt \tag{A.50}$$
$$= \int_{0}^{\infty} e^{i(\omega-\omega_0+i\Gamma/2)t}dt \tag{A.51}$$
$$= \left[\frac{1}{i(\omega-\omega_0+i\Gamma/2)}e^{i(\omega-\omega_0+i\Gamma/2)t}\right]_0^{\infty} \tag{A.52}$$
$$= \frac{i}{\omega-\omega_0+i\Gamma/2}. \tag{A.53}$$

The probability as a function of ω is then given by

$$|\phi(\omega)|^2 \propto \frac{1}{(\omega-\omega_0)^2+(\Gamma/2)^2} \tag{A.54}$$

which has a width at half max of Γ. Hence, Γ is both the decay rate and the linewidth when the spectrum is plotted as a function of ω, i.e Γ has units of ω. This is an important point as both angular ω and linear f frequency are quoted in the literature and proper conversion must be applied. The above argument carried out using the Fourier transform in terms of the linear frequency f

$$\phi(f) = \int_{-\infty}^{\infty} \psi(t)e^{2\pi i f t}dt \tag{A.55}$$

gives the intensity as

$$|\phi(f)|^2 \propto \frac{1}{4\pi^2(f-f_0)^2+(\Gamma/2)^2}. \tag{A.56}$$

Measuring the width at half max for this spectrum plotted as a function of linear frequency would then give $\Gamma/2\pi$. Both values are in units of per second however in literature the decay rate quoted in terms of ω is usually given in units of $[\mathrm{s}^{-1}]$ where as linear frequency f units are given by [Hz].

A.4 Weisskopf units

The reduced transition probability for the nuclear electric (EL) or magnetic (ML) transition is given by

$$\mathbb{B}(EK, i\to f) = \mathbb{B}_W(EK, i\to f)\frac{1}{4\pi}\left(\frac{3}{K+3}\right)^2 (1.2A)^{2K}e^2(\mathrm{fm})^{2K} \tag{A.57}$$
$$\mathbb{B}(ML, i\to f) = \mathbb{B}_W(MK, i\to f)\frac{10}{\pi}\left(\frac{3}{K+3}\right)^2 1.2^{(2K-2)/2}\mu_N^2(\mathrm{fm})^{2K-2} \tag{A.58}$$

$\mathbb{B}_W$ is the value in Weisskopf units, K the multipolarity of the transition, $R = 1.2A^{1/3}$ is the radius of the nucleus in units of femtometers ($\mathrm{fm} = 10^{-15}\mathrm{m}$) with A the number of nucleons. $\mu_N = \frac{e\hbar}{2m_pc}$ is the nuclear magneton.

A.5 Early time decay rate in NFS spectrum

Following [119, p.16] the emitted electric field from a two state system excited by a delta pulse, $\Omega(t,0) = \delta(t-\tau)$, with detuning $\Delta = 0$ is given by,

$$E(t) \propto \xi\exp(-\Gamma t/2)J_1(\sqrt{4\xi\Gamma t})/\sqrt{\xi\Gamma t}$$

where $\xi = N\sigma L/4$, $\eta = 2\xi\Gamma/L$, and J_1 is the first Bessel function of the first kind. In the case of early time after excitation $\Gamma t \ll 1/(1+\xi)$

$$E(t) \propto \xi \exp(-(1+\xi)\Gamma t/2)$$

making the intensity

$$I(t) \propto \xi^2 \exp(-(1+\xi)\Gamma t)$$

and thus there is an enhancement of the decay rate for early time of $(1+\xi)$. The factor ξ comes from the decay rate of the population and the additional factor of 1 comes from the decay of the coherence. Hence, if there are additional decoherence terms, as there are for the thorium doped crystal, than the coherence terms can take the form seen in equation (2.13). For example the decay rate of the coherence term ρ_{31} is given by

$$\gamma_{13}^c + \Gamma/2$$

therefore the early time NFS spectrum looking at the $3 \rightarrow 1$ transition will have a decay rate of $2\gamma_{13}^c + \Gamma + \xi\Gamma$ as discussed in Chapter 2.

A.6 Introducing pulse phase shift in initial conditions

In Section 2.2 we discussed the use of multi pulsed excitation with laser pulses of differing phase. To achieve pulses with differing phases we first consider E1 excitation with a single mode field $\boldsymbol{E}(\boldsymbol{r}_i, t) = \mathscr{E}\cos(\nu t + \phi)\hat{\boldsymbol{x}}$. The interaction potential is,

$$\begin{aligned} \hat{V} &= -\boldsymbol{d}_i \cdot \boldsymbol{E}(\boldsymbol{r}_i, t), && \text{(A.59)} \\ &= -(d_{21}|2\rangle\langle 1| + d_{21}^*|1\rangle\langle 2|)\mathscr{E}\cos(\nu t + \phi), && \text{(A.60)} \end{aligned}$$

applying unitary transformation

$$\hat{U} = \begin{pmatrix} 1 & 0 \\ 0 & e^{-i\nu t} \end{pmatrix} \quad \text{(A.61)}$$

we arrive at,

$$\begin{aligned} \hat{\tilde{V}} &= -(d_{21}e^{i\nu t}|2\rangle\langle 1| + d_{21}^* e^{-i\nu t}|1\rangle\langle 2|)\mathscr{E}\cos(\nu t + \phi) && \text{(A.62)} \\ &= -\frac{\hbar}{2}\left(d_{21}\left(e^{i(2\nu t+\phi)} + e^{-i\phi}\right)|2\rangle\langle 1| + d_{21}^*\left(e^{i\phi} + e^{-i(2\nu t+\phi)}\right)|1\rangle\langle 2|\right) && \text{(A.63)} \\ &\overset{RWA}{\approx} -\frac{\hbar}{2}\left(d_{21}e^{-i\phi}|2\rangle\langle 1| + d_{21}^* e^{i\phi}|1\rangle\langle 2|\right) && \text{(A.64)} \\ &= -\frac{\hbar}{2}\left(\Omega|2\rangle\langle 1| + \Omega^*|1\rangle\langle 2|\right), && \text{(A.65)} \end{aligned}$$

where now we define the Rabi frequency as $\Omega = d_{21}\mathscr{E}e^{-i\phi}/\hbar$. The only difference here to the usual case of excitation with $\boldsymbol{E}(\boldsymbol{r}_i, t) = \mathscr{E}\cos(\nu t)\hat{\boldsymbol{x}}$ is phase factor $e^{i\phi}$. The initial conditions of the NFS calculation then defines the phase of the pulse,

$$\Omega(0, t) = \Omega_0 e^{-(t/T)^2} e^{i\phi}. \quad \text{(A.66)}$$

The phase only has an impact on the excitation when there is more than one excitation pulse. In the case of multiple pulses it is then the relative phase that affects the intensity seen in the NFS spectrum. Both relative phase and time delay can have a significant effect as shown for example with equation (2.29) for two pulses with time delay and phase difference.

A.7 Multipulsed excitation: superposition

Testing the solution for multiple pulses exciting the two-state system against the MBE: Consider 2 pulses arriving at the sample at t_1, t_2, with phases ϕ_1, ϕ_2,

$$I_n(t) \propto \left|\sum_n N e^{-\Gamma(t-t_n)/2} e^{i(\Delta(t-t_n)+\phi_n)}\right|^2, \quad \text{(A.67)}$$

$$I_2(t) \propto N^2\left(e^{-\Gamma(t-t_1)} + e^{-\Gamma(t-t_2)} + 2e^{-\Gamma(2t-t_1-t_2)/2}\cos(\Delta(t_2-t_1) - (\phi_2-\phi_1))\right). \quad \text{(A.68)}$$

The intensity of the exciting pulse cannot be separated from the signal therefore we must compare two intensity points after the excitations have happened, i.e we cannot compare intensities directly at $t = t_1, t_2$. The intensity at time δ, where $t_2 > \delta > t_1$, after the first pulse is then,

$$I_1(\delta) = N^2 e^{-\Gamma(\delta - t_1)}, \tag{A.69}$$

$$N^2 = \frac{I_1(\delta)}{e^{-\Gamma(\delta - t_1)}}. \tag{A.70}$$

Plugging into the above equation for the intensity after the second pulse we find

$$I_2(t) = I_1(\delta)e^{-\Gamma(t-\delta)} + I_1(\delta)e^{-\Gamma(t-\delta-t_2+t_1)} + 2I_1(\delta)e^{-\Gamma\left(t-\delta-\frac{t_2-t_1}{2}\right)}\cos(\Delta(t_2-t_1) - (\phi_2 - \phi_1)). \tag{A.71}$$

Hence we can compare the intensity after the second pulse $I_2(t)$ using first the above equation and secondly using the MBE. In both cases $I_1(\delta)$ is given as a starting intensity from the MBE calculation. This simple model does not yield an exact match in intensities, however, predicts the correct trends in the output intensity which is valuable for a basic understanding of the system.

A.8 Electric field gradient

The quantization axis is aligned with the dominant component of the electric field gradient experienced by the thorium nucleus inside the crystal environment. Following [76, p124], the electric field gradient (EFG) tensor is given by

$$\boldsymbol{\nabla E} = -\begin{bmatrix} V_{xx} & V_{xy} & V_{xz} \\ V_{yx} & V_{yy} & V_{yz} \\ V_{zx} & V_{zy} & V_{zz} \end{bmatrix}, \qquad V_{nm} = \frac{\partial^2 V}{\partial n \partial m}, \tag{A.72}$$

$$\boldsymbol{E} = -\boldsymbol{\nabla} V = -(\hat{\boldsymbol{x}} V_x + \hat{\boldsymbol{y}} V_y + \hat{\boldsymbol{z}} V_z). \tag{A.73}$$

The eigenvectors of the diagonalized EFG tensor define the principal axes. Once diagonalized, $\nabla^2 V = V_{xx} + V_{yy} + V_{zz} = 0$. By convention, we define the axes such that $|V_{zz}| \geq |V_{yy}| \geq |V_{zz}|$, and $\eta = (V_{xx} - V_{yy})/V_{zz}$ is the asymmetry factor such that $\eta = 0$ defines axial symmetry.

Here we discuss the most relevant cases of 90° and 180° dopant orientations using point charges to represent the flouride interstitials. Consider the thorium nuclei at the origin and the two fluoride interstitials placed a distance a and b in the x-y plane at 90° with the origin giving,

$$V^{(90)} = -ke\left[((x-a)^2 + y^2 + z^2)^{-1/2} + (x^2 + (y-b)^2 + z^2)^{-1/2}\right], \tag{A.74}$$

$$V_{xx}^{(90)}|_0 = ke\left(\frac{1}{|b|^3} - \frac{2}{|a|^3}\right), \tag{A.75}$$

$$V_{yy}^{(90)}|_0 = ke\left(\frac{1}{|a|^3} - \frac{2}{|b|^3}\right), \tag{A.76}$$

$$V_{zz}^{(90)}|_0 = ke\left(\frac{1}{|a|^3} + \frac{1}{|b|^3}\right), \tag{A.77}$$

$$\eta^{(90)} = \frac{3}{|b|^3} - \frac{3}{|a|^3}. \tag{A.78}$$

Placing the F^- either side thorium along the z axis for 180° gives,

$$V^{(180)} = -ke\left[(x^2 + y^2 + (z-a)^2)^{-1/2} + (x^2 + y^2 + (z+b)^2)^{-1/2}\right], \tag{A.79}$$

$$V_{xx}^{(180)}|_0 = V_{yy}^{(180)}|_0 = ke\left(\frac{1}{|a|^3} + \frac{1}{|b|^3}\right), \tag{A.80}$$

$$V_{zz}^{(180)}|_0 = -ke\left(\frac{2}{|a|^3} + \frac{2}{|b|^3}\right), \tag{A.81}$$

$$\eta^{(180)} = 0. \tag{A.82}$$

A.9 Multipole radiation selection rules

In the case of electric (magnetic) dipole transitions, the transition moment operator $\boldsymbol{\mathcal{M}}_{E1(M1)}$ is a rank-1 tensor i.e., vector. Hence we can write it in its spherical basis components $\boldsymbol{\chi}_{-q}$ see Appendix A.11,

$$\boldsymbol{\mathcal{M}}_{E1(M1)} = \sum_{q=-1}^{q=1} (-1)^q \mathcal{M}_{E1(M1),q} \boldsymbol{\chi}_{-q}. \tag{A.83}$$

The electric and magnetic dipole interaction Hamiltonians are

$$\hat{V}^{E1} = -\boldsymbol{d} \cdot \boldsymbol{E}, \tag{A.84}$$

$$\hat{V}^{M1} = -\boldsymbol{m} \cdot \boldsymbol{B}, \tag{A.85}$$

where $\boldsymbol{d}$ and $\boldsymbol{m}$ are more standard notation for the electric (magnetic) transition moment operators and $\boldsymbol{E}$ and $\boldsymbol{B}$ the exciting electric and magnetic fields respectively [45, p.202]. The electric and magnetic fields can be expanded in the spherical basis, and the inner product carried out to give

$$\hat{V}^{E1} = -\sum_{q=-1}^{q=1} (-1)^q \mathcal{D}_{E1,q} E_{-q}, \tag{A.86}$$

$$\hat{V}^{M1} = -\sum_{q=-1}^{q=1} (-1)^q \mathcal{M}_{M1,q} B_{-q}. \tag{A.87}$$

As a result we can deduce the required polarization of the field to drive each transition. Magnetic dipole transitions are more relevant to this work so as an example, for a $\mathcal{M}_{M1,-1}$ ($\Delta m = -1$) transition, we require a left-handed circularly polarized magnetic field $\boldsymbol{B} = B\hat{\boldsymbol{b}} = B_1 \boldsymbol{\chi}_{-1}$ where $\hat{\boldsymbol{b}} = \boldsymbol{\chi}_{-1} = \frac{1}{\sqrt{2}}(\hat{\boldsymbol{x}} - i\hat{\boldsymbol{y}})$. In the context of transitions, the polarization $(\boldsymbol{\chi}_0, \boldsymbol{\chi}_1, \boldsymbol{\chi}_{-1})$ is also referred to as $(\pi, \sigma^+, \sigma^-)$.

In addition to the type and polarization of the exciting field, we know from the Wigner-Eckhart theorem and the properties of the Clebsch-Gordan coefficients, that a matrix element $\langle j m_j | O_{k,q} | j' m_j' \rangle$ is only non-zero provided $\boldsymbol{j} = \boldsymbol{j}' + \boldsymbol{k}$ and $m_j = m_j' + q$. Furthermore, the multipolarity of a transition given by the change in angular momentum $l = \Delta I$ defines the parity P of a multipole transition is $P = (-1)^l$ for electric 2^l-pole El and $P = (-1)^{l-1}$ for magnetic 2^l-pole Ml transitions. Thus, for both E1 and M1 transitions we require $\Delta j = 0, \pm 1$ and $\Delta m = 0, \pm 1$, and for E1 $P_f = -P_i$, and M1 $P_f = P_i$.

A.10 Multi-quantization axis calculations

Calculations involving samples with multiple quantization axes rely on the ability to project the exciting laser field's polarization vector onto the different q-axis frames. By doing so one can determine the transitions that will be driven in each frame and then the resulting polarization of the emitted radiation. Fields resulting from the decay of the excited states with like polarization in the lab frame then add in superposition resulting in the final recorded spectrum.

To keep track of the polarization vectors throughout the calculation we define the lab frame by $(\hat{\boldsymbol{x}}, \hat{\boldsymbol{y}}, \hat{\boldsymbol{z}})$, and the quantization axis frame by $(\hat{\boldsymbol{\alpha}}, \hat{\boldsymbol{\beta}}, \hat{\boldsymbol{q}})$, where the quantization axis has vector components $\hat{\boldsymbol{q}} = (q_x, q_y, q_z)$ in the lab frame and,

$$\hat{\boldsymbol{\alpha}} = \frac{\hat{\boldsymbol{z}} - (\hat{\boldsymbol{z}} \cdot \hat{\boldsymbol{q}})\hat{\boldsymbol{q}}}{|\hat{\boldsymbol{z}} - (\hat{\boldsymbol{z}} \cdot \hat{\boldsymbol{q}})\hat{\boldsymbol{q}}|}, \tag{A.88}$$

$$\hat{\boldsymbol{\beta}} = \hat{\boldsymbol{q}} \times \hat{\boldsymbol{\alpha}}. \tag{A.89}$$

The polarization vectors for a given transition can then be defined in the q-axis frame,

$$\hat{\boldsymbol{\pi}}_q = \hat{\boldsymbol{q}}, \tag{A.90}$$

$$\hat{\boldsymbol{\sigma}}_q^+ = -\frac{1}{\sqrt{2}}(\hat{\boldsymbol{\alpha}} + i\hat{\boldsymbol{\beta}}), \tag{A.91}$$

$$\hat{\boldsymbol{\sigma}}_q^- = \frac{1}{\sqrt{2}}(\hat{\boldsymbol{\alpha}} - i\hat{\boldsymbol{\beta}}). \tag{A.92}$$

Given a field with unit amplitude polarized along $\hat{\boldsymbol{p}}$ in the lab frame, one then projects onto vectors $\hat{\boldsymbol{\chi}}_q = (\hat{\boldsymbol{\pi}}_q, \hat{\boldsymbol{\sigma}}_q^+, \hat{\boldsymbol{\sigma}}_q^-)$ to give the amplitude A of the field driving each transition in the q frame,

$$A_q^0 = \hat{\boldsymbol{p}} \cdot \hat{\boldsymbol{\pi}}_q = p_x \pi_{q,x}^* + p_y \pi_{q,y}^* + p_z \pi_{q,z}^*, \tag{A.93}$$

$$A_q^+ = \hat{\boldsymbol{p}} \cdot \hat{\boldsymbol{\sigma}}_q^+, \tag{A.94}$$

$$A_q^- = \hat{\boldsymbol{p}} \cdot \hat{\boldsymbol{\sigma}}_q^-. \tag{A.95}$$

The amplitude projections are used as initial conditions to define the peak Rabi frequency for each transition type, and in each q-axis frame. For each q-axis frame there are three field equations,

$$\left(\frac{\partial}{\partial z} + \frac{1}{c}\frac{\partial}{\partial t}\right) \Omega_q^{(0,+,-)} = i\eta \sum_{i,f} C_{fi} \rho_{fi}^{(0,+,-)}, \tag{A.96}$$

one for each polarization direction $(\hat{\boldsymbol{\pi}}_q, \hat{\boldsymbol{\sigma}}_q^+, \hat{\boldsymbol{\sigma}}_q^-)$. Here $\rho_{fi}^{(0,+,-)}$, denotes the density matrix elements for transitions of type $(0,+,-)$ from initial state i to final state f.

Upon completion of the calculation all resultant fields $\Omega_q^{(0,+,-)}$ are projected onto the lab frame axes giving components in (x, y, z),

$$\boldsymbol{\Omega}_q^{(0,+,-)} = \Omega_q^{(0,+,-)} \hat{\boldsymbol{\chi}}_{q,(0,+,-)} = (\Omega_{q,x}^{(0,+,-)}, \Omega_{q,y}^{(0,+,-)}, \Omega_{q,z}^{(0,+,-)}). \tag{A.97}$$

(x, y, z) components of each field can then be added in superposition to find the resultant intensity.

This method was used to consider crystals with multiple quantization axes as well as multiple crystals excited sequentially, where the output field from one crystal forms the input to the next.

A.11 The spherical basis

The spherical basis is used extensively when talking about polarized excitations, as such a brief overview is presented here following [116, p.23] [89].

A vector in Cartesian basis is given by,

$$\boldsymbol{f} = f_x \hat{\boldsymbol{x}} + f_y \hat{\boldsymbol{y}} + f_z \hat{\boldsymbol{z}}. \tag{A.98}$$

Vectors in the spherical basis are given by,

$$\boldsymbol{f} = \sum_{\mu=-1}^{1} f^\mu \boldsymbol{\chi}_\mu = \sum_{\mu=-1}^{1} f_\mu \boldsymbol{\chi}_\mu^* = \sum_{\mu=-1}^{1} (-1)^\mu f_\mu \boldsymbol{\chi}_{-\mu}, \tag{A.99}$$

where the unit vectors are that of linear and circular polarization,

$$\boldsymbol{\chi}_0 = \hat{\boldsymbol{z}}, \tag{A.100}$$

$$\boldsymbol{\chi}_{\pm 1} = \mp \frac{1}{\sqrt{2}} (\hat{\boldsymbol{x}} \pm i\hat{\boldsymbol{y}}). \tag{A.101}$$

The spherical basis vectors obey $\boldsymbol{\chi}_\mu \boldsymbol{\chi}_{\mu'}^* = \delta_{\mu\mu'}$ and the spherical coordinates in contravariant and covariant form are given by,

$$f^0 = f_z,\ f^{\pm 1} = \mp \frac{1}{\sqrt{2}} (f_x \mp i f_y), \qquad f_0 = f_z,\ f_{\pm 1} = \mp \frac{1}{\sqrt{2}} (f_x \pm i f_y). \tag{A.102}$$

The inner product is defined by,

$$\boldsymbol{f} \cdot \boldsymbol{g} = \sum_{\mu=-1}^{1} f^\mu g_\mu = \sum_{\mu=-1}^{1} g^\mu f_\mu = \sum_{\mu=-1}^{1} (-1)^\mu f_\mu g_{-\mu}. \tag{A.103}$$

A.12 Computation of magnetic-dipole coupling operator

In an effort to simplify notation we can break down the matrix elements further and denote $\mathcal{T}_{M1,q} \to \mathcal{T}_{1q}$,

$$\langle m_s | \mathcal{T}_{1,+1} | m_s' \rangle = \frac{1}{c} \left[\frac{l_+ \delta_{m_s,m_s'}}{r^3} + \frac{\delta_{m_s,m_s'+1}}{\sqrt{2} r^3} + \frac{3 r_+}{2 r^5} \langle m_s | \boldsymbol{\sigma} \cdot \boldsymbol{r} | m_s' \rangle - \frac{8\pi}{3\sqrt{2}} \delta_{m_s,m_s'+1} \delta(\boldsymbol{r}) \right],$$

$$\langle m_s | \mathcal{T}_{1,-1} | m_s' \rangle = \frac{1}{c} \left[\frac{l_- \delta_{m_s,m_s'}}{r^3} - \frac{\delta_{m_s,m_s'-1}}{\sqrt{2} r^3} + \frac{3 r_-}{2 r^5} \langle m_s | \boldsymbol{\sigma} \cdot \boldsymbol{r} | m_s' \rangle + \frac{8\pi}{3\sqrt{2}} \delta_{m_s,m_s'-1} \delta(\boldsymbol{r}) \right],$$

$$\langle m_s | \mathcal{T}_{1,0} | m_s' \rangle = \frac{1}{c} \left[\frac{l_0 \delta_{m_s,m_s'}}{r^3} - \frac{m_s' \delta_{m_s,m_s'}}{r^3} + \frac{3 r_0}{2 r^5} \langle m_s | \boldsymbol{\sigma} \cdot \boldsymbol{r} | m_s' \rangle + \frac{8\pi m_s'}{3} \delta_{m_s,m_s'} \delta(\boldsymbol{r}) \right].$$

Solving the spin component,

$$\langle \tfrac{1}{2}|\mathcal{T}_{1+}|\tfrac{1}{2}\rangle = \frac{1}{c}\left[\frac{l_+}{r^3} + \frac{3r_+\cos\theta}{2r^4}\right], \tag{A.104}$$

$$\langle -\tfrac{1}{2}|\mathcal{T}_{1+}|-\tfrac{1}{2}\rangle = \frac{1}{c}\left[\frac{l_+}{r^3} - \frac{3r_+\cos\theta}{2r^4}\right], \tag{A.105}$$

$$\langle \tfrac{1}{2}|\mathcal{T}_{1+}|-\tfrac{1}{2}\rangle = \frac{1}{c}\left[\frac{1}{\sqrt{2}r^3} + \frac{3r_+e^{-i\phi}\sin\theta}{2r^4} - \frac{8\pi}{3\sqrt{2}}\delta(\boldsymbol{r})\right], \tag{A.106}$$

$$\langle -\tfrac{1}{2}|\mathcal{T}_{1+}|\tfrac{1}{2}\rangle = \frac{1}{c}\left[\frac{3r_+e^{i\phi}\sin\theta}{2r^4}\right], \tag{A.107}$$

$$\langle \tfrac{1}{2}|\mathcal{T}_{1-}|\tfrac{1}{2}\rangle = \frac{1}{c}\left[\frac{l_-}{r^3} + \frac{3r_-\cos\theta}{2r^4}\right], \tag{A.108}$$

$$\langle -\tfrac{1}{2}|\mathcal{T}_{1-}|-\tfrac{1}{2}\rangle = \frac{1}{c}\left[\frac{l_-}{r^3} - \frac{3r_-\cos\theta}{2r^4}\right], \tag{A.109}$$

$$\langle \tfrac{1}{2}|\mathcal{T}_{1-}|-\tfrac{1}{2}\rangle = \frac{1}{c}\left[\frac{3r_-e^{-i\phi}\sin\theta}{2r^4}\right], \tag{A.110}$$

$$\langle -\tfrac{1}{2}|\mathcal{T}_{1-}|\tfrac{1}{2}\rangle = \frac{1}{c}\left[-\frac{1}{\sqrt{2}r^3} + \frac{3r_-e^{i\phi}\sin\theta}{2r^4} + \frac{8\pi}{3\sqrt{2}}\delta(\boldsymbol{r})\right], \tag{A.111}$$

$$\langle \tfrac{1}{2}|\mathcal{T}_{10}|\tfrac{1}{2}\rangle = \frac{1}{c}\left[\frac{l_0}{r^3} - \frac{1}{2r^3} + \frac{3r_0\cos\theta}{2r^4} + \frac{8\pi}{6}\delta(\boldsymbol{r})\right], \tag{A.112}$$

$$\langle -\tfrac{1}{2}|\mathcal{T}_{10}|-\tfrac{1}{2}\rangle = \frac{1}{c}\left[\frac{l_0}{r^3} + \frac{1}{2r^3} - \frac{3r_0\cos\theta}{2r^4} - \frac{8\pi}{6}\delta(\boldsymbol{r})\right], \tag{A.113}$$

$$\langle \tfrac{1}{2}|\mathcal{T}_{10}|-\tfrac{1}{2}\rangle = \frac{1}{c}\left[\frac{3r_0e^{-i\phi}\sin\theta}{2r^4}\right], \tag{A.114}$$

$$\langle -\tfrac{1}{2}|\mathcal{T}_{10}|\tfrac{1}{2}\rangle = \frac{1}{c}\left[\frac{3r_0e^{i\phi}\sin\theta}{2r^4}\right]. \tag{A.115}$$

When comparing matrix elements, it is clear that many terms are similar. This can be useful during computation. Comparing $\mathcal{T}_{1\pm}$ for $m_s = m_s'$ we can define[48],

$$① = -\frac{1}{\sqrt{2}r^3} i l_y = \frac{1}{\sqrt{2}r^3}\left(-\cos\phi\frac{\partial}{\partial\theta} + \cot\theta\sin\phi\frac{\partial}{\partial\phi}\right), \tag{A.116}$$

$$② = -\frac{1}{\sqrt{2}r^3}\frac{l_x}{i} = -\frac{1}{\sqrt{2}r^3}\left(\sin\phi\frac{\partial}{\partial\theta} + \cot\theta\cos\phi\frac{\partial}{\partial\phi}\right), \tag{A.117}$$

$$③ = -\frac{3\cos\theta\sin\theta\cos\phi}{2\sqrt{2}r^3}, \tag{A.118}$$

$$④ = -\frac{3\cos\theta\sin\theta\sin\phi}{2\sqrt{2}r^3}, \tag{A.119}$$

making the final matrix elements,

$$\langle \tfrac{1}{2}|\mathcal{T}_{1+}|\tfrac{1}{2}\rangle = \frac{1}{c}\left[(① + ③) + i(② + ④)\right], \tag{A.120}$$

$$\langle -\tfrac{1}{2}|\mathcal{T}_{1+}|-\tfrac{1}{2}\rangle = \frac{1}{c}\left[(① - ③) + i(② - ④)\right], \tag{A.121}$$

$$\langle \tfrac{1}{2}|\mathcal{T}_{1-}|\tfrac{1}{2}\rangle = \frac{1}{c}\left[(① - ③) + i(-② + ④)\right], \tag{A.122}$$

$$\langle -\tfrac{1}{2}|\mathcal{T}_{1-}|-\tfrac{1}{2}\rangle = \frac{1}{c}\left[(① + ③) + i(-② - ④)\right]. \tag{A.123}$$

[48] $\int f(r,\theta,\phi)\,\mathrm{d}V = \int f(r,\theta,\phi)r^2\sin\theta\,\mathrm{d}r\,\mathrm{d}\theta\,\mathrm{d}\phi = \int k(r,\theta,\phi)r^2\,\mathrm{d}r\,\mathrm{d}\theta\,\mathrm{d}\phi$ when building the functions to be integrated multiply through by $\sin\theta$ from $\mathrm{d}V$ to remove the undefined values for $\cot\theta$ at 0 and π in the data set prior to the integration step.

Comparing now $\langle\frac{1}{2}|\mathcal{T}_{1+}|-\frac{1}{2}\rangle$ with $\langle-\frac{1}{2}|\mathcal{T}_{1-}|\frac{1}{2}\rangle$, and $\langle-\frac{1}{2}|\mathcal{T}_{1+}|\frac{1}{2}\rangle$ with $\langle\frac{1}{2}|\mathcal{T}_{1-}|-\frac{1}{2}\rangle$ we define,

$$⑤ = \frac{1}{\sqrt{2}r^3}, \tag{A.124}$$

$$⑥ = \frac{3r_+e^{-i\phi}\sin\theta}{2r^4} = -\frac{3r_-e^{i\phi}\sin\theta}{2r^4} = -\frac{3\sin^2\theta}{2\sqrt{2}r^3}, \tag{A.125}$$

$$⑦ = -\frac{8\pi}{3\sqrt{2}}\delta(\boldsymbol{r}), \tag{A.126}$$

$$⑧ = -\frac{3\sin^2\theta}{2\sqrt{2}r^3}\cos(2\phi), \tag{A.127}$$

$$⑨ = -\frac{3\sin^2\theta}{2\sqrt{2}r^3}\sin(2\phi), \tag{A.128}$$

giving,

$$\langle\tfrac{1}{2}|\mathcal{T}_{1+}|-\tfrac{1}{2}\rangle = \frac{1}{c}\left[⑤+⑥+⑦\right], \tag{A.129}$$

$$\langle-\tfrac{1}{2}|\mathcal{T}_{1+}|\tfrac{1}{2}\rangle = \frac{1}{c}\left[⑧+i⑨\right], \tag{A.130}$$

$$\langle\tfrac{1}{2}|\mathcal{T}_{1-}|-\tfrac{1}{2}\rangle = \frac{1}{c}\left[-⑧+i⑨\right], \tag{A.131}$$

$$\langle-\tfrac{1}{2}|\mathcal{T}_{1-}|\tfrac{1}{2}\rangle = \frac{1}{c}\left[-⑤-⑥-⑦\right]. \tag{A.132}$$

Comparing $\langle\frac{1}{2}|\mathcal{T}_{10}|\frac{1}{2}\rangle$ with $\langle-\frac{1}{2}|\mathcal{T}_{10}|-\frac{1}{2}\rangle$, and $\langle\frac{1}{2}|\mathcal{T}_{10}|-\frac{1}{2}\rangle$ with $\langle-\frac{1}{2}|\mathcal{T}_{10}|\frac{1}{2}\rangle$ we define

$$⑩ = -\frac{1}{r^3}\frac{\partial}{\partial\phi}, \tag{A.133}$$

$$⑪ = \frac{3\cos^2\theta}{2r^3}, \tag{A.134}$$

giving,

$$\langle\tfrac{1}{2}|\mathcal{T}_{10}|\tfrac{1}{2}\rangle = \frac{1}{c}\left[i⑩-\frac{1}{\sqrt{2}}⑤+⑪-\frac{1}{\sqrt{2}}⑦\right], \tag{A.135}$$

$$\langle-\tfrac{1}{2}|\mathcal{T}_{10}|-\tfrac{1}{2}\rangle = \frac{1}{c}\left[i⑩+\frac{1}{\sqrt{2}}⑤-⑪+\frac{1}{\sqrt{2}}⑦\right], \tag{A.136}$$

$$\langle\tfrac{1}{2}|\mathcal{T}_{10}|-\tfrac{1}{2}\rangle = \frac{1}{c}\left[-\sqrt{2}③+i\sqrt{2}④\right], \tag{A.137}$$

$$\langle-\tfrac{1}{2}|\mathcal{T}_{10}|\tfrac{1}{2}\rangle = \frac{1}{c}\left[-\sqrt{2}③-i\sqrt{2}④\right]. \tag{A.138}$$

The Fermi contact term

Each element of $\mathcal{T}_{M1,q}$ has a term $\propto a\delta(\boldsymbol{r})$ where a is a constant. These are the Fermi contact (FC) terms which must be considered carefully.

When benchmarking with quasi-relativistic wave functions as done in Section 7.1 the following procedure was used to determine the value of the wave functions at the origin. The delta function in spherical coordinates is defined as $\delta(\boldsymbol{r}) = \delta^3(r,\theta,\phi) = \frac{1}{r^2\sin\theta}\delta(r)\delta(\theta)\delta(\phi)$. The set of quasi-relativistic wave functions are of the form $\psi_{nlm} = \frac{1}{r}P_{nl}(r)Y_{lm}(\theta,\phi)$, where we approximate the radial component of the wave function with the large component of the relativistic wave function P. We can then solve,

$$\langle nlm|\delta(\boldsymbol{r})|n'l'm'\rangle = \int \psi_f^*\delta(\boldsymbol{r})\psi_i r^2\sin\theta\,\mathrm{d}r\,\mathrm{d}\theta\,\mathrm{d}\phi \tag{A.139}$$

$$= \int \psi_f^*\delta(r)\delta(\theta)\delta(\phi)\psi_i\,\mathrm{d}r\,\mathrm{d}\theta\,\mathrm{d}\phi \tag{A.140}$$

$$= \int \frac{P_{nl}^*}{r}\delta(r)\frac{P_{n'l'}}{r}\,\mathrm{d}r\int Y_{lm}^*\delta(\theta)\delta(\phi)Y_{l'm'}\,\mathrm{d}\theta\,\mathrm{d}\phi \tag{A.141}$$

$$= \left[\frac{P_{nl}^*(r)P_{n'l'}(r)}{r^2}\right]_{r=0}\left[Y_{lm}^*(\theta,\phi)Y_{l'm'}(\theta,\phi)\right]_{\substack{\theta=0\\\phi=0}}. \tag{A.142}$$

We know from [48, p.120] that the radial wave function which for us is $R_{nl}(r) = P_{nl}(r)/r$ is proportional to r^l at the origin. Therefore, the radial component is different from zero only for s-states ($l = 0$) at the origin $r = 0$. As a result we have

$$\langle nlm|\delta(\boldsymbol{r})|n'l'm'\rangle = \frac{\delta_{l0}\delta_{ll'}\delta_{mm'}}{4\pi}\left[\frac{P^*_{nl}(r)P_{n'l'}(r)}{r^2}\right]_{r=0}. \tag{A.143}$$

To deal with the delta function numerically, fit P_{nl} with a polynomial of order r^{l+1} giving $P_{nl} \approx \sum_{k=0}^{l} a_{nk}r^{k+1}$. Then the radial component[49], $R_{nl} = \sum_{k=0}^{l} a_{nk}r^k = a_{nl}r^l$ and at the origin $R_{nl}(0) \approx a_{nl}\delta_{l0}$ giving the final result as

$$\langle nlm|\delta(\boldsymbol{r})|n'l'm'\rangle = \frac{a^*_{nl}a_{n'l'}}{4\pi}\delta_{l0}\delta_{ll'}\delta_{mm'}. \tag{A.144}$$

The wave functions used for electrons in the crystal environment are already non-relativistic, as such we do not have to deal with the above fitting procedure. Rather we must extrapolate the wave function directly to get an approximate value at the origin. The origin in the case of EB in the crystal is the thorium nucleus. None of the wave functions used had a significant value at the origin, and thus the FC terms in the crystal had negligible effect here. This can be understood if we look at the color-center wave functions in Figure 5.4 which are the most localized around the thorium nucleus. These wave functions are predominantly f-like making the value at the origin negligible. In the case of the few wave functions with a significant s character such as PBE 364 and 367 or HSE 361 the FC term is still negligible as it only acts on $s \to s$ type transitions of which there are effectively none.

[49] As we know from earlier all $a_{nk} = 0$ except for $k = l$. Numerically, this is not strictly the case due to error, however the a_{nl} should be dominant.

Bibliography

1. Peik, E. & Tamm, C. Nuclear laser spectroscopy of the 3.5 eV transition in Th-229. *Europhys. Lett.* **61,** 181–186 (2003).
2. Seiferle, B. *et al.* Energy of the ^{229}Th nuclear clock transition. *Nature* **573,** 243–246 (2019).
3. Minkov, N. & Pálffy, A. Reduced Transition Probabilities for the Gamma Decay of the 7.8 eV Isomer in ^{229}Th. *Phys. Rev. Lett.* **118,** 212501 (2017).
4. Campbell, C. J. *et al.* Single-Ion Nuclear Clock for Metrology at the 19th Decimal Place. *Phys. Rev. Lett.* **108,** 120802 (2012).
5. Campbell, C. J., Radnaev, A. G. & Kuzmich, A. Wigner Crystals of ^{229}Th for Optical Excitation of the Nuclear Isomer. *Phys. Rev. Lett.* **106,** 223001 (2011).
6. Rellergert, W. G. *et al.* Constraining the Evolution of the Fundamental Constants with a Solid-State Optical Frequency Reference Based on the ^{229}Th Nucleus. *Phys. Rev. Lett.* **104,** 200802 (2010).
7. Kazakov, G. A. *et al.* Performance of a ^{229}Thorium solid-state nuclear clock. *New Journal of Physics* **14,** 083019 (2012).
8. Dessovic, P. *et al.* ^{229}Thorium-doped calcium fluoride for nuclear laser spectroscopy. *J. Phys.: Condens. Matter* **26,** 105402 (2014).
9. Peik, E. & Okhapkin, M. Nuclear clocks based on resonant excitation of γ-transitions. *Comptes Rendus Physique* **16.** The measurement of time / La mesure du temps, 516 – 523 (2015).
10. Stellmer, S. *et al.* Attempt to optically excite the nuclear isomer in ^{229}Th. *Phys. Rev. A* **97,** 062506 (2018).
11. Peik, E. *private communication* 2017.
12. Thompson, R. C. Ion Coulomb crystals. *Contemporary Physics* **56,** 63–79 (2015).
13. Itano, W. M. *et al.* Quantum projection noise: Population fluctuations in two-level systems. *Phys. Rev. A* **47,** 3554–3570 (1993).
14. Beck, B. R. *et al.* Energy Splitting of the Ground-State Doublet in the Nucleus ^{229}Th. *Phys. Rev. Lett.* **98,** 142501 (2007).
15. Beck, B. R. *et al.* Improved Value for the Energy Splitting of the Ground-State Doublet in the Nucleus 229Th. *CERN-Proceedings* **1** (2010).
16. Von der Wense, L. *et al.* Direct detection of the 229Th nuclear clock transition. *Nature* **533,** 47–51 (2016).
17. Seiferle, B., von der Wense, L. & Thirolf, P. Lifetime Measurement of the ^{229}Th Nuclear Isomer. *Phys. Rev. Lett.* **118,** 042501 (2017).
18. Von der Wense, L. *et al.* The concept of laser-based conversion electron Mössbauer spectroscopy for a precise energy determination of ^{229m}Th. *Hyperfine Interactions* **240,** 23 (2019).
19. Jeet, J. *et al.* Results of a Direct Search Using Synchrotron Radiation for the Low-Energy ^{229}Th Nuclear Isomeric Transition. *Phys. Rev. Lett.* **114,** 253001 (2015).
20. Yamaguchi, A. *et al.* Experimental search for the low-energy nuclear transition in ^{229}Th with undulator radiation. *New Journal of Physics* **17,** 053053 (2015).
21. Stellmer, S., Schreitl, M. & Schumm, T. Radioluminescence and photoluminescence of Th:CaF_2 crystals. *Sci. Rep.* **5,** 15580 (2015).
22. Pimon, M. & Mohn, P. *private communication* 2019.

23. Rix, S. *Radiation-induced Defects in Calcium Fluoride and Their Influence on Material Properties under 193 nm Laser Irradiation* PhD thesis (Johannes Gutenberg-Universität, Mainz, 2011).

24. Dessovic, P. *Ab-initio calculations for Thorium doped Calcium Fluoride (CaF_2)* Diplomarbeit, Technischen Universität Wien (2016).

25. Dicke, R. H. The Effect of Collisions upon the Doppler Width of Spectral Lines. *Phys. Rev.* **89,** 472 (1953).

26. Liao, W. T., Das, S., Keitel, C. H. & Pálffy, A. Coherence-Enhanced Optical Determination of the ^{229}Th Isomeric Transition. *Phys. Rev. Lett.* **109,** 262502 (2012).

27. Hannon, J. P. & Trammell, G. T. Coherent γ-ray optics. *Hyperfine Interactions* **123/124,** 127 (1999).

28. Crisp, M. D. Propagation of Small-Area Pulses of Coherent Light through a Resonant Medium. *Phys. Rev. A* **1,** 1604 (1970).

29. Hartmann, H. J. & Laubereau, A. Coherent pulse propagation in the infrared on the picosecond time scale. *Opt. Commun.* **47,** 117 (1983).

30. Rothenberg, J. E., Grischkowsky, D. & Balant, A. C. Observation of the Formation of the 0π Pulse. *Phys. Rev. Lett.* **53,** 552 (1984).

31. Das, S., Pálffy, A. & Keitel, C. H. Quantum interference effects in an ensemble of ^{229}Th nuclei interacting with coherent light. *Phys. Rev. C* **88,** 024601 (2013).

32. Liao, W. T. & Pálffy, A. Optomechanically induced transparency of x-rays via optical control. *Sci. Rep.* **7,** 321 (2017).

33. Stellmer, S., Schreitl, M., Kazakov, G. A., Sterba, J. H. & Schumm, T. Feasibility study of measuring the ^{229}Th nuclear isomer transition with ^{233}U-doped crystals. *Phys. Rev. C* **94,** 014302 (2016).

34. Barker, B. J. *et al.* Oxidation State of 229Th Recoils Implanted into MgF2 Crystals. *Science Journal of Chemistry* **6** (2018).

35. Bilous, P. V., Peik, E. & Pálffy, A. Laser-induced electronic bridge for characterization of the ^{229m}Th $\rightarrow$ ^{229g}Th nuclear transition with a tunable optical laser. *New Journal of Physics* **20,** 013016 (2018).

36. Bilous, P. V., Minkov, N. & Pálffy, A. The electric quadrupole channel of the 7.8 eV ^{229}Th transition. *Phys. Rev. C* **97,** 044320 (2018).

37. Bilous, P. V. *Towards a nuclear clock with the ^{229}Th isomeric transition* PhD thesis (University of Heidelberg, 2018).

38. Porsev, S. G. & Flambaum, V. V. Effect of atomic electrons on the 7.6-eV nuclear transition in ^{229}Th^{3+}. *Phys. Rev. A* **81,** 032504 (2010).

39. Dicke, R. H. Coherence in Spontaneous Radiation Processes. *Phys. Rev.* **93,** 99 (1954).

40. Scully, M. O. & Zubairy, M. S. *Quantum Optics* (Cambridge University Press, 1999).

41. Shvyd'ko, Y. V. Nuclear resonant forward scattering of x rays: Time and space picture. *Phys. Rev. B* **59,** 9132 (1999).

42. Gunst, J. *Mutual control of x-rays and nuclear transitions* PhD thesis (University of Heidelberg, 2015).

43. Gunst, J. & Pálffy, A. X-ray quantum-eraser setup for time-energy complementarity. *Phys. Rev. A* **94,** 063849 (2016).

44. Mandel, L. & Wolf, E. *Optical coherence and quantum optics* (Cambridge University Press, 1995).

45. Shore, B. W. *The Theory of Coherent Atomic Excitation* (Wiley, 1990).

46. Allen, L. & Eberly, J. H. *Optical resonance and two-level atoms* (Wiley, 1975).

47. De Valcarcel, G. J., Roldan, E. & Prati, F. Semiclassical Theory of Amplification and Lasing. *Revista Mexicana de Fisica E* **52,** 198–214 (2006).

48. Landau, L. D. & Lifshitz, E. M. *Quantum Mechanics Non-Relativistic Theory* 3rd ed. (Pergamon Press, 1991).

49. Boyd, R. *Nonlinear Optics* 3rd ed. (Academic Press, 2008).

50. Keeling, J. *Light-Matter Interactions and Quantum Optics* (CreateSpace Independent Publishing Platform, 2014).

51. Del Valle Reboul, E. *Quantum Electrodynamics with Quantum Dots in Microcavities* PhD thesis (Universidad Autonoma de Madrid, 2009).

52. Fujii, K., Higashida, K., Kato, R. & Wada, Y. N Level System with RWA and Analytical Solutions Revisited. *arXiv:quant-ph/0307066v2* (2003).

53. Jackson, J. *Classical Electrodynamics* 3rd ed. (John Wiley & Sons, Inc., 1999).

54. Shvyd'ko, Y. V. *et al.* Hybrid beat in nuclear forward scattering of synchrotron radiation. *Phys. Rev. B* **57,** 3552–3561 (1998).

55. Chen, Y. L. & Yang, D. P. *Mössbauer Effect in Lattice Dynamics* (Wiley, 2007).

56. Steck, D. A. *Quantum and Atom Optics* (Available online at http://steck.us/teaching (revision 0.11.4, 26 October 2016), 2016).

57. Loudon, R. *The Quantum Theory of Light* 3rd ed. (Oxford, 2000).

58. Steck, D. A. Rubidium 87 D line data. *Available online at http://steck.us/alkalidata/ (revision 1.6, 14 October 2003)* (2001).

59. Perkins, D. H. *Introduction to High Energy Physics* 4th ed. (Cambridge, 2000).

60. Blatt, J. M. & F.Weisskopf, V. *Theoretical Nuclear Physics* (Springer-Verlag, 1979).

61. Bransden, B. H. & Joachain, C. J. *Physics of atoms and molecules* 2nd ed. (Prentice Hall, 2003).

62. Ring, P. & Schuck, P. *The Nuclear Many-Body Problem* (Springer Verlag, New York, 1980).

63. Edmonds, A. R. *Angular momentum in Quantum Mechanics* (Princeton University Press, 1957).

64. Rubloff, G. Far-Ultraviolet Reflectance Spectra and the Electronic Structure of Ionic Crystals. *Phys. Rev. B* **5,** 662 (1972).

65. Barth, J., Johnson, R. L., Cardona, M., Fuchs, D. & Bradshaw, A. Dielectric function of CaF_2 between 10 and 35 eV. *Phys. Rev. B* **41,** 3291 (1990).

66. Tsujibayashi, T. & Toyoda, K. Spectral profile of the two-photon absorption coefficients in CaF_2 and BaF_2. *Appl. Phys. Lett.* **80,** 2883 (2002).

67. Tkalya, E. V. Proposal for a Nuclear Gamma-Ray Laser of Optical Range. *Phys. Rev. Lett.* **106,** 162501 (2011).

68. Bemis, C. E. *et al.* Coulomb excitation of states in 229 Th. *Physica Scripta* **38,** 657 (1988).

69. Thielking, J. *et al.* Laser spectroscopic characterization of the nuclear-clock isomer ^{229m}Th. *Nature* **556,** 321 (2018).

70. Palffy, A., Evers, J. & Keitel, C. H. Electric-dipole-forbidden nuclear transitions driven by super-intense laser fields. *Physical Review C* **77,** 044602 (2009).

71. Tkalya, E. V., Schneider, C., Jeet, J. & Hudson, E. R. Radiative lifetime and energy of the low-energy isomeric level in ^{229}Th. *Phys. Rev. C* **92,** 054324 (2015).

72. Zhao, X. *et al.* Observation of the deexcitation of the ^{229m}Th nuclear isomer. *Phys. Rev. Lett.* **109,** 160801 (2012).

73. Smirnov, G. V. General properties of nuclear resonant scattering. *Hyperfine Interactions* **123,** 31–77 (1999).

74. Liao, W. T., Pálffy, A. & Keitel, C. H. Coherent Storage and Phase Modulation of Single Hard-X-Ray Photons Using Nuclear Excitons. *Phys. Rev. Lett.* **109,** 197403 (2012).

75. Matthias, E., Schneider, W. & Steffen, R. M. Nuclear Level Splitting Caused by a Combined Electric Quadrupole and Magnetic Dipole Interaction. *Phys. Rev.* **125,** 261 (1962).

76. Collins, R. L. & Travis, J. C. in *Mössbauer Effect Methodology* (ed Gruverman, I. J.) 123 (Springer, New York, 1967).

77. Suits, B. H. in *Handbook of Applied Solid State Spectroscopy* (ed Vij, D.) 65 (Springer, Boston, MA, 2006).

78. Cho, H. Dependence of nuclear quadrupole resonance transitions on the electric field gradient asymmetry parameter for nuclides with half-integer spins. *Atomic Data and Nuclear Data Tables* **111-112,** 29–40 (2016).

79. Röhlsberger, R. *Nuclear Condensed Matter Physics with Synchrotron Radiation* (Springer-Verlag, Berlin, 2004).

80. *The Electromagnetic Interaction in Nuclear Spectroscopy* (ed Hamilton, W. D.) (North-Holland, 1975).

81. Sobelman, I. I. *Atomic Spectra And Radiative Transitions* (Springer-Verlag, Berlin, 1979).

82. Porsev, S. G., Flambaum, V. V., Peik, E. & Tamm, C. Excitation of the Isomeric ^{229m}Th Nuclear State via an Electronic Bridge Process in ^{229}Th^{+}. *Phys. Rev. Lett.* **105,** 182501 (2010).

83. Porsev, S. G. & Flambaum, V. V. Electronic bridge process in ^{229}Th^{+}. *Phys. Rev. A* **81,** 042516 (2010).

84. Johnson, W. R. *Atomic Structure Theory: Lectures on Atomic Physics* (Springer, New York, 2007).

85. Greiner, W. *Relativistic Quantum Mechanics* 3rd ed. (Springer, 2000).

86. Abragam, A. *The principles of nuclear magnitisem* (Oxford University Press, 1961).

87. Armstrong, L. *Theory of the hyperfine structure of free atoms* (Wiley-Interscience, 1971).

88. Bethe, H. A. & Salpeter, E. *Quantum mechanics of one- and two-electron atoms* (Springer, 1957).

89. Varshalovich, D. A., Moskalev, A. N. & Khersonskii, V. K. *Quantum theory of angular momentum* (World Scientific, 1988).

90. Kresse, G. & Furthmüller, J. Efficient iterative schemes for ab initio total-energy calculations using a plane-wave basis set. *Phys. Rev. B* **54,** 11169–11186 (1996).

91. Blöchl, P. E., Först, C. J. & Schimpl, J. Projector augmented wave method:ab initio molecular dynamics with full wave functions. *Bulletin of Materials Science* **26,** 33–41 (2003).

92. Kresse, G. & Joubert, D. From ultrasoft pseudopotentials to the projector augmented-wave method. *Phys. Rev. B* **59,** 1758–1775 (1999).

93. Kohn, W. & Sham, L. Self-Consistant Equations Including Exchange and Correlation Effects. *Physical Review* **140,** 1133–1138 (1965).

94. Parr, R. & Yang, W. *Density functional theory of atoms and molecules* (Oxford University Press, 1989).

95. Noorden, R. V., Maher, B. & Nuzzo, R. The top 100 papers: Nature explores the most-cited research of all time. *Nature* **514,** 550–553 (2014).

96. Perdew, J. P., Ernzerhof, M. & Burke, K. Rationale for mixing exact exchange with density functional approximations. *J. Chem. Phys.* **105,** 9982 (1996).

97. Heyd, J., Scuseria, G. E. & Ernzerhof, M. Hybrid functionals based on a screened Coulomb potential. *J. Chem. Phys.* **118,** 8207 (2003).

98. Davydov, A. S. *Quantum Mechanics* (Pergamon Press, 1965).

99. Jönsson, P., Gaigalas, G., Bieron, J., Fischer, C. F. & Grant, I. P. New version: Grasp2K relativistic atomic structure package. *Computer Physics Communications* **184,** 2197 (2013).

100. Bilous, P. V. *private communication* 2019.

101. Kennedy, W. L. Partial equivalence of the correct and incorrect versions of the Darwin term. *J. Phys. A: Math. Gen.* **21,** 3021 (1988).

102. Hiller, J., Sucher, J. & Feinberg, G. New techniques fro evaluating parity-conserving and parity-violating contact interactions. *Phys. Rev. A* **18** (1978).

103. Geertsen, J. Calculation of the indirect nuclear spin-spin coupling constant in HD using a golbal operator representation of the Fermi contact operator. *Chem. Phys. Lett.* **116** (1985).

104. Ozmen, A., Cakr, B. & Yakar, Y. Electronic structure and relativistic terms of one-electron spherical quantum dot. *Journal of Luminescence* **137,** 259–268 (2013).

105. Foldy, L. L. & Wouthuysen, S. A. On the Dirac Theory of Spin 1/2 Particles and its Non-Relativistic Limit. *Phys. Rev.* **78** (1950).

106. Childs, W. J. & Goodman, L. S. Hyperfine Interactions and the Magnetic Fields Due to Core Polarization in Fe^{57}. *Phys. Rev.* **148,** 74–78 (1966).

107. Eibschütz, M., Shtrikman, S. & Treves, D. Mössbauer Studies of Fe^{57} in Orthoferrites. *Phys. Rev.* **156,** 562–577 (1967).

108. Zemcik, T. Mössbauer six-line spectra position analysis for Fe^{57} in metallic iron. *Czech J. Phys.* **18,** 551 (1968).

109. Perlow, G. J. *et al.* Polarization of Nuclear Resonance Radiation in Ferromagnetic Fe^{57}. *Phys. Rev. Lett.* **4,** 74–75 (1960).

110. Van Bürck, U., Siddons, D. P., Hastings, J. B., Bergmann, U. & Hollatz, R. Nuclear forward scattering of synchrotron radiation. *Phys. Rev. B* **46,** 6207–6211 (1992).

111. Keune, W., Date, S. K., Dézsi, I. & Gonser, U. Mössbauereffect study of Co^{57} and $Fe5^{57}$ impurities in ferroelectric $LiNbO_3$. *Journal of Applied Physics* **46,** 3914–3924 (1975).

112. Sepiol, B. *et al.* Time Domain Study of ^{57}Fe Diffusion using Nuclear Forward Scattering of Synchrotron Radiation. *Phys. Rev. Lett.* **76,** 3220–3223 (1996).

113. Nussbaum, R. H. & Housley, R. M. Internal conversion in Fe57 from the Mössbauer effect in iron. *Nuclear Physics* **68,** 145 –152 (1965).

114. Smirnov, G. V. Nuclear resonant scattering of synchrotron radiation. *Hyperfine Interactions* **97/98,** 551–588 (1996).

115. Lübbers, R. *Magnetism and Lattice Dynamics under High Pressure Studied by Nuclear Resonant Scattering of Synchrotron Radiation* PhD thesis (Universität Paderborn, 2000).

116. Akhiezer, A. I. & Berestetski, V. B. *Quantum Electrodynamics* (Interscience Publishers, 1965).

117. Sakurai, J. J. & Napolitano, J. *Modern Quantum Mechanics* 2nd ed. (Addison-Wesley, 2011).

118. Messiah, A. *Quantum Mechanics* (North-Holland, 1967).

119. Liao, W. T. *Coherent Control of Nuclei and X-Rays* PhD thesis (University of Heidelberg, 2013).

Acknowledgements

I would first and foremost like to thank my supervisor PD Dr. Adriana Pálffy-Buß who gave me the opportunity not only to complete my doctoral studies in her group, but also for providing the opportunity to experience a new culture by living here in Germany while doing so. Her discussion on the scientific topics presented here as well as general scientific writing style and presentation has proved invaluable.

I would like to thank Assoc. Prof. Dr. Wen-Te Liao. His discussion during the early stages of this doctoral work was important to bring me up to speed on the work previously done by himself and A. Pálffy-Buß regarding NFS in thorium doped crystals, as well as the use of the MBE to model such systems.

I would like to thank Dr. Pavlo Bilous. He was instrumental in helping me make the transition from the study of NFS to that of EB. His discussion helped not only in my understanding of EB processes in ions, which he is a expert in, but also application to the crystal environment which is the new work presented here.

I would like to acknowledge Prof. Dr. Thorsten Schumm for his initial idea to use defects within the thorium-doped crystals as a means to excite the thorium nucleus. I would also like to thank him for the discussion of this topic as well as initiating the collaboration between our group at the MPIK in Heidelberg, Germany with the group of Prof. Dr. Peter Mohn as well as his own group at the Technische Universität Wien, Austria.

I would like to thank Martin Pimon who is currently working on his Doctorate in the group of P. Mohn. The work on EB could not be completed without his careful calculation of electronic wave functions in the crystal environment.

I would like to thank Kjeld Beeks who is currently working on his Doctorate in the group of T. Schumm. His discussion regarding crystal damage and their experimental efforts to measure the isomeric state of thorium as well as the electronic color-center states in ^{229}Th:CaF_2 has been helpful.

I would like to thank the nuClock consortium headed by T. Schumm which was funded by the European Unions Horizon 2020 research and innovation programme under grant agreement No. 664732. The nuClock consortium brought together research partners and provided funding for the development of a nuclear clock based on the isomeric state of ^{229}Th. I benefited greatly from this funding which allowed me to conduct my research along with travel to a variety of conferences across Germany as well as in Belgium and Austria to discuss my results and learn from others in the field.

Thank you to, Assoc. Prof. Dr. Wen-Te Liao, Dr. Pavlo Bilous and Dr. Sergey Bragin for reading parts of this dissertation and providing helpful suggestions and corrections.

Finally, I would like to thank Honorarprofessor Dr. Christoph H. Keitel for providing me with the opportunity to work in his division and the MPIK, as well as to all of my colleagues and administration who created an encouraging working environment.